

**An efficient cosmic muon veto detector
for experiments at shallow depth and
feasibility of internal magnetic field
measurements using cosmic muons**

By

Neha

PHYS01201404004

Bhabha Atomic Research Centre, Mumbai - 400 085

*A thesis submitted
to the Board of Studies in
Physical Sciences*

*In partial fulfillment of requirements
For the Degree of*

DOCTOR OF PHILOSOPHY
of
HOMI BHABHA NATIONAL INSTITUTE



July, 2019

Homi Bhabha National Institute

Recommendations of the Viva Voce Committee

As members of the Viva Voce Committee, we certify that we have read the dissertation prepared by **Neha** entitled “**An efficient cosmic muon veto detector for experiments at shallow depth and feasibility of internal magnetic field measurements using cosmic muons**” and recommend that it may be accepted as fulfilling the thesis requirement for the award of Degree of Doctor of Philosophy.

Chairman - B. K. Nayak

Date:

Guide / Convener - V. M. Datar

Date:

Co-Guide - G. Majumder

Date:

Examiner -

Date:

Member 1 - L. M. Pant

Date:

Member 2 - S. K. Agarwalla

Date:

Final approval and acceptance of this thesis is contingent upon the candidate's submission of the final copies of the thesis to HBNI.

I hereby certify that I have read this thesis prepared under my direction and recommend that it may be accepted as fulfilling the thesis requirement.

Date:

Place:

Prof. V.M. Datar

STATEMENT BY THE AUTHOR

This dissertation has been submitted in partial fulfillment of requirements for an advanced degree at Homi Bhabha National Institute (HBNI) and is deposited in the library to be made available to borrowers under rules of the HBNI.

Brief quotations from this dissertation are allowable without special permission, provided that accurate acknowledgement of source is made. Requests for permission for extended quotation from or reproduction of this manuscript in whole or in part may be granted by the Competent Authority of HBNI when in his or her judgment the proposed use of the material is in the interests of scholarship. In all other instances, however, permission must be obtained from the author.

July 2019, Mumbai

Neha

DECLARATION

I hereby declare that the investigation presented in the thesis has been carried out by me. The work is original and has not been submitted earlier as a whole or in part for a degree/diploma at this or any other Institution/University.

July 2019, Mumbai

Neha

List of Publications arising from the thesis

Publications in Refereed Journal

Published

1. **N. Panchal**, S. Mohanraj, A. Kumar, T. Dey, G. Majumder, R. Shinde, P. Verma, B. Satyanarayana and V.M. Datar, "A compact cosmic muon veto detector and possible use with the Iron Calorimeter detector for neutrinos.", *Journal of Instrumentation*, **12** (2017) T11002.
2. **N. Panchal**, G. Majumder and V.M. Datar, "Simulation of muon-induced neutral particle background for a shallow depth Iron Calorimeter detector." *Journal of Instrumentation*, **14** (2019) P02032.

Communicated

1. "Design, construction and performance of magnetised mini-ICAL detector module.", INO mini-ICAL group, Proceedings of XXXIX International Conference on High Energy Physics.

Symposium and conference proceedings

Published

1. **Neha**, et al., "A compact cosmic muon veto detector and possible use with the Iron Calorimeter detector for neutrinos.", Proceedings of the DAE Symp. on Nucl. Phys., **62** (2017) 1076.
2. **Neha**, et al., "Can Stopped Cosmic Muons Be Used to Estimate the Magnetic Field in the Prototype ICAL Detector?," XXII DAE High Energy Physics Symposium-Proceedings, Springer Science and Business Media, LLC, **203** (2018) 93.
3. **Neha**, et al., "Simulation Study of a Possible Indium-Based Cryogenic Detector for Electron Neutrinos.," XXII DAE High Energy Physics Symposium-Proceedings, Springer Science and Business Media, LLC, **203** (2018) 841.
4. **N. Panchal**, et al., "Simulation studies for false positive event rate due to muon-induced neutral particles for a shallow depth ICAL detector." , Proceedings of the DAE Symp. on Nucl. Phys., **63** (2019) 1128.

Communicated

1. **Neha**, et al., "Simulation studies for a shallow depth ICAL." XXIII DAE High Energy Physics Symposium-Proceedings, Springer Science and Business Media, LLC.
2. **Neha**, et al., " μ SR with mini-ICAL." XXIII DAE High Energy Physics Symposium-Proceedings, Springer Science and Business Media, LLC.

July 2019, Mumbai

Neha

DEDICATED TO

To my family and friends

ACKNOWLEDGEMENTS

Firstly, I would like to express my sincere gratitude to my thesis advisor Prof. V.M. Datar for his continuous support and guidance towards the completion of my PhD. His immense knowledge and passion for research is highly motivating for me. I could not have imagined having a better advisor and mentor than him. Besides my advisor, I would like to thank my co-supervisor Prof. Gobinda Majumder for his insightful comments and encouragement. I am thankful to him for all those long sessions that we had for discussions and problem solving together. I admire him for his hard work and outlook towards research.

I also want to thank my other committee members, B.K. Nayak, L.M. Pant, S.K. Agarwalla for examining my work every year and providing valuable feedback. My sincere gratitude is reserved for N.K. Mondal, B.S. Acharya, Amol Dighe, Umasankar, D. Indumathi, V. Nanal, A.K. Mohanty, S. Saha and D. Samuel for being wonderful teachers. My sincere thanks also goes to B. Satyanarayana, S.S. Upadhyaya and Mandar Saraf who provided me an opportunity to learn electronics.

Special thanks to Pathaleshwar and R.R. Shinde who have patiently supported various analysis and instrumentation related issues in my experiments. I am grateful to Varchaswi Kashyap, Vivek Singh, Neha Dokania, S. Mathimalar, Amina Khatun, Nitali Dash, Ali Azmi and Saurabh Shandilya for being really nice and encouraging seniors during the initial days of PhD. It was delightful to work with Dipankar Sil, an amazing colleague and friend. I thank my batch mates Apoorva and Nizam who provided great company, starting from course work to till thesis writing. I thank my juniors Jim John, Honey, Pethuraj, S.

Mondal, J. Datta, Harishree, C. Ghosh, and Roni Dey for being there whenever required.

I am very thankful to BARC colleagues Sourabh Pathak, Sandip Patel, S. Ajith, N.S. Dalal, S.P. Prabhakar, T.S. Srinivasan, D.N. Badodkar from DRHR (for mini-ICAL design, fabrication and assembly), S.P. Srivastava, K.N. Karn, P.I. Hadagali, P.K. Biswas, Alok Tripathi, Sachin Dolas, Prabhat Singh, Vinay Sharma, Sanjay Patil, Suresh Jaiswar (CDM) , R. Rengan, K. Srinivas from CED (for mini-ICAL related civil work), S. Achrekar, N. Ayyagiri, A. Behere, V.B. Chandratre, D. Das, A. Jain, N. Kamble, T. Kasbekar, H. Kolla, A. Manna, S. Mohanan, S. Moitra, P.M. Nair, S. Padmini, M. Punna, S.M. Raut, S. Prafulla, S. Sikder, M. Sukhwani from ED (for mini-ICAL electronics and instrumentation), P.S. Shetty, B. Sivaramakrishna, Mathew Dominic and Shashank Padwal from TSD (for LCWCS and Electrical work for mini-ICAL) for their dedicated support in building mini- ICAL at Madurai. I am very thankful to S.K. Thakur, A. Bera, A. Ghosh, and N. Mohamed (VECC magnet team) for the design of the magnet coil, lending the power supply and developing the necessary control software. I am also thankful to other members of the INO project who were stationed at Madurai IICHEP transit campus viz. K.C. Ravindran, N. Sivaramakrishnan, Umesh and Rajkumar Bharathi for their support in detector building and data taking. I also wish to thank Vijaykumar who took care of our transport but also went beyond his call of duty to help in any way that he could. Many thanks to all the project students and INO graduate students, who have taken part in assembling of mini-ICAL detector.

My thanks to the TIFR members, V. Asgolkar, S. Chavan, G. Ghodke, D. Gonji (for assistance during setting up experiments), S. Dasgupta, Upendra

Gokhale, S.R. Joshi, Puneet Kaur, A. Lokapure, T.T.S. Singh (for the electronics design and fabrication), S.D. Kalmani (for setting up gas system), P. Verma (for mechanical design and drawings), P. Kumar and P. Nagaraj (for computer cluster related issues and problem solving in general).

I appreciate continuous motivation and support from Abhijit Garai and Yuvaraj. Your company made my stay at TIFR much easier and happier. I thank all of those with whom I spent sleepless nights working together meeting deadlines, and for all the fun we have had in the last five years. Last, but not the least, I would like to thank my family, my parents and brothers, for supporting me throughout my Ph.D. student days and my life in general.

Contents

Synopsis	xxiii
List of Figures	xxxiii
List of Tables	xxxix
List of Abbreviations	xli
1 Introduction	1
1.1 Neutrinos	1
1.2 ICAL	4
1.2.1 Resistive Plate Chamber (RPC)	5
1.2.2 ICAL Magnet	9
1.3 SICAL	11
1.4 mini-ICAL	12
1.5 Muon spin rotation	14
1.5.1 Basic principle	14

1.5.2	Polarization of cosmic ray muon	15
1.5.3	μ SR with cosmic muons	17
2	A Compact Cosmic Muon Veto Detector	19
2.1	CMV assembly	21
2.2	Data Acquisition	27
2.3	Results and discussion	31
2.3.1	Cosmic Muon Rejection Efficiency	31
2.3.2	γ -ray induced mis-identification rate	34
2.3.3	Other sources of inefficiencies in CMV	36
2.4	Proof of principle demonstration in mini-ICAL	40
2.5	Summary	41
3	Muon induced neutral background for SICAL	43
3.1	Simulation Framework	44
3.2	Case I : Simplistic Geometry and Vertical muons	47
3.2.1	False positive event rate in ICAL due to muon-induced neutrals	52
3.2.2	Neutrino event rate for ICAL detector	55
3.3	Case II : Cavern Hugging Configuration of CMVD	56
3.4	Results and discussions	61
3.5	Estimation of false positive event rate in the SICAL due to muon- induced neutrals.	65
3.6	Summary	66
4	Commissioning of mini-ICAL detector	69

4.1	m-ICAL magnet	69
4.1.1	Magnetic field measurement system	75
4.2	Detector	79
4.2.1	RPC assembly	79
4.2.2	Gas system	80
4.2.3	Electronics and Data Acquisition	81
4.3	Basic test of the RPCs	85
4.4	Muon trajectories and efficiency of RPC	88
4.5	Summary	90
5	An attempt to measure the magnetic field in iron using Muon Spin Rotation in mini-ICAL	91
5.1	Studies with 12 layer stack of RPC	92
5.1.1	GEANT4 based simulation	93
5.1.2	Experimental Set up	95
5.1.3	Electronics readout and DAQ	97
5.1.4	Data Analysis	99
5.2	Studies with 5 layer stack of plastic scintillators	101
5.2.1	Ion Feedback in PMT	103
5.3	Search for μ SR signal in mini-ICAL	105
5.4	Summary	113
6	Summary	115
	Bibliography	119

Synopsis

The neutrino, a neutral fermion, participates only in weak interaction, is a fundamental constituent in the standard model (SM) of particle physics. The neutrino has been elusive ever since it was first proposed in the year 1930 by Pauli [1], in order to explain the observed continuous energy spectrum of the electron emitted in the beta decay. According to the SM, there exist three types of neutrinos namely, electron neutrino, muon neutrino, and tau neutrino associated with the corresponding charged leptons. Recent experiments have conclusively shown that the neutrinos oscillate from one flavour to another as they propagate. This phenomenon of neutrino oscillation [2] can be explained by representing the neutrino flavour state as a super-position of mass eigenstate ν_1 , ν_2 and ν_3 with mass m_1 , m_2 and m_3 respectively. The oscillation probability is related to the differences in the mass squared ($\Delta m_{ij}^2 = m_i^2 - m_j^2$). Various experiments have been conducted using atmospheric, solar, reactor and accelerator neutrinos to measure Δm_{12}^2 and Δm_{13}^2 . However, the sign of Δm_{13}^2 is not yet known. This allows two different hierarchies, namely, normal hierarchy (NH), and inverted

hierarchy (IH). The knowledge of this mass hierarchy can help us to understand some of the outstanding questions such as CP violation, Dirac or Majorana nature of neutrinos and their absolute masses through a measurement of $0\nu\beta\beta$ decay. The independent analysis of the T2K [3] and NO ν A [4] data shows a preference towards normal hierarchy. Additional knowledge can also be gained by studying the atmospheric neutrinos as they offer wide range of energies and baselines. An Indian effort has been initiated to build a magnetized Iron CALorimeter (ICAL) detector at India-based Neutrino Observatory (INO) [5], to study atmospheric neutrinos with the primary aim of addressing the mass hierarchy problem. ICAL is going to be a magnetized detector and can therefore distinguish μ^+ and μ^- , produced in charged current neutrino interaction with iron nuclei, by the bending of their trajectories in two different directions. ICAL will be having 151 layers of 5.6 cm thick iron plates interspersed with 150 layer of Resistive Plate Chambers (RPC). RPC is a gas detector used to detect charged particles. It works on the principle of ionization and electron multiplication. The neutrino energy measurement in ICAL is indirect through a measurement of the energy of muon in view of earlier comment on CC interaction. Therefore, it becomes very important to reduce any other background in the ICAL detector involving a muon. At sea level, the cosmic ray muons are the most dominant background for detector like ICAL. To reduce this background by a factor of 10^6 , the proposed ICAL will be located under a mountain cover of 1 km. There is a reduction of 10^2 in muon flux at a depth of 100 m in rock. Hence, if we build a cosmic muon veto detector (CMVD) with an veto efficiency of 99.99% then we can think of a shallow depth ICAL (SICAL) which will have same background as at the proposed INO site. In this direction, to explore the possibility of SICAL, a small cosmic muon veto

(CMV) detector of dimensions $\sim 1 \text{ m} \times 1 \text{ m} \times 0.3 \text{ m}$ was made and tested.

Another vital background for SICAL is the neutrals, produced due to interaction of cosmic muons with rock. The muon-nuclear interaction results in the production of many charged and uncharged particles. The charged particles produced in such interaction can be vetoed in CMVD whereas the neutrals can go undetected. These neutrals can produce false positive signals in ICAL which mimics neutrino events. Such background needs to be carefully investigated before building the SICAL detector. The proposition of SICAL can be advantageous as the availability of an enhanced cosmic muon flux at lower depths can be used as a probe to monitor detector performance. Also it may be helpful to estimate the magnetic field inside iron by using muon spin rotation (μSR) technique [6].

In this thesis work, a small experimental set-up of CMVD is made to study its veto efficiency and the results are presented. This is followed by results from a GEANT4-based [7] simulation study of cosmic muon induced neutral background for the SICAL detector. The feasibility of using a novel technique, μSR for estimating the internal magnetic field inside iron in ICAL is also discussed.

Compact cosmic muon veto detector at TIFR

The cosmic muon veto hut was made using 14 plastic scintillators (PSs) of dimensions 320 mm (width) \times 960 mm (length) \times 10 mm (thickness). Two layers of PSs were employed making inner and outer hut. At the top, two layers of PSs were placed perpendicular to each other. In the first (I) configuration, a set of 4 PSs of dimensions 440 mm \times 440 mm \times 10 mm thick positioned one top of another were used to generate cosmic muon trigger. This trigger set-up is referred as MuL in this text. A 4-fold coincidence in MuL ensures a muon signal

whereas an OR of all 14 PS was ANDed with the 4-fold to produce 5-fold signal. The muon veto efficiency is defined as the ratio of 5-fold to 4-fold. Also care has been taken to reduce γ -induced coincidences in MuL by placing a layer of lead sandwiched between two sets of PSs. The analysis of the event-by-event TDC data gives an overall veto efficiency of $(99.880 \pm 0.007)\%$ for the configuration (I). To place trigger paddles more centrally, a second (II) configuration with smaller PSs of dimensions $150 \text{ mm} \times 200 \text{ mm} \times 10 \text{ mm}$ thick was used. This trigger set-up is referred as MuS in this text. The configuration (II) data gives an overall veto efficiency of $(99.847 \pm 0.005)\%$. To further investigate the sources of inefficiency of the CMV, we also did the 2D efficiency scan of all the 14 PSs used in hut. For this study we had used the 12 layers RPC stack at TIFR. In a set, 3 PSs were placed on top of layer 5 in the stack and the muon trigger was generated by an AND of layers 4,5,6 and 7. The trigger ensures that the muon has gone through the PS. The hit information was stored along with the rest of RPC hit signals in Data Acquisition System whereas for PS's timing data a separate multi-hit TDC was used. The efficiency in zones of $30 \text{ cm} \times 30 \text{ cm}$ was estimated. It was found that one of the inner top side PS was less efficient. But it didn't contribute significantly to the overall veto efficiency because it was at side of the trigger set-up. This PMT was replaced for subsequent experiments. In the third (III) configuration, three PSs from the outer side hut were taken and kept on the top. The 3rd layer was placed with an offset of 20 mm with the 2nd layer at the top. This was done to cover the gaps of the below layer. For configuration (III), a set of measurements was performed by varying the thresholds of the MuS trigger paddles from -20 mV to -150 mV to emphasize muons and reduce the electromagnetic shower contribution. An increased threshold results in increase

in veto efficiency from $(99.823 \pm 0.012)\%$ to $(99.922 \pm 0.010)\%$. A larger threshold reduces the chance of trigger generation inside the hut due to low energy particles which may not give a hit in the CMV hut paddles resulting in inefficiency. This also reduces the rate of random coincidence of MuS trigger. The effect of removing or placing lead between successive layers of the plastic scintillators constituting the muon trigger MuS on the CMV detector efficiency was studied. With no lead in MuS for configuration (III), the veto efficiency dropped to $(99.16 \pm 0.01)\%$. This is significantly smaller than the efficiency with one layer of lead in configuration (II), strongly suggesting that γ -ray induced events are being misidentified as muons leading to a lower CMV efficiency. To test this hypothesis, configuration (IV) with three layers of lead were placed in between successive plastic scintillators of MuS was studied. In order to reduce the γ - γ coincidences, the fourth (IV) configuration had 3 layers of lead alternatively with respect to the PSs in MuS. The overall veto efficiency achieved in this case was $(99.978 \pm 0.003)\%$. This result gave us confidence to pursue the idea of SICAL but before proposing it we need to check the feasibility of CMV on a bigger proof-of-principle detector. CMV detector is planned for a 85 ton magnetized prototype ICAL called mini-ICAL. mini-ICAL is already operational at IICHEP, Madurai. The dimensions of mini-ICAL are $4\text{ m} \times 4\text{ m} \times 1.2\text{ m}$ having 10 layers of RPCs ($2\text{ m} \times 2\text{ m}$) populated in the central region of the magnet assembly having 11 layers of iron, each of thickness 5.6 cm.

Muon-induced neutral background for SICAL

To estimate the contribution of the false positives in ICAL, a GEANT4-based simulation was performed. In the simulation, a geometry encompassing a cavern ($80\text{ m} \times 26\text{ m} \times 26\text{ m}$) covered with a 3 cm thin plastic scintillator from 5 sides

along with rock of surface area $2 \text{ km} \times 2 \text{ km}$ was made. The ICAL detector was enclosed inside the rock and cavern assembly. The study was performed for a depth of 103 m of rock thickness. But propagating the muon along with all the secondaries produced in muon path takes a large amount of computational time. To reduce the time, the simulation was divided into two parts. In the first part, muons with 3D (E, θ, ϕ) flux distribution was generated by CORSIKA software [8] using SIBYLL model [9] and was propagated through 100 m of rock. The (x, y) positions were generated randomly over a surface of $2 \text{ km} \times 2 \text{ km}$. E, θ, ϕ, x, y of the muon was stored after it traverse the full thickness of rock. In this part of the simulation only muon ionization is taken into account as the physics process in GEANT4. Then this energy shifted 3D flux becomes the input to the second part of the simulation. In the second part, the rock dimensions were chosen to be $600 \text{ m} \times 600 \text{ m} \times 3 \text{ m}$ (thickness). The choice of thickness of rock was guided by the hadronic interaction length in iron which is 36 cm. This implies that the secondaries produced in, approximately, the last 36 cm of rock via muon-nuclear interaction will be able to come out of rock. But in the simulation we have considered the thickness of rock to be ~ 10 times the hadronic interaction length. In this simulation, all the secondaries produced are propagated through the rock volume. The muon which could exit rock was not propagated after CMVD because it will be already vetoed by CMVD. However all other particles are allowed to pass through CMVD and then ICAL. All the information of particles coming out of 3 m of rock was stored at the CMVD and was used to distinguish events with neutral particle coming with or without any accompanying charged particle. If in an event no charged particle having energy more than 10 MeV gets detected in CMVD but a neutral with energy more than

1 GeV passes through CMVD then we look for a reconstructed track in ICAL detector. This reconstructed track is considered to be false positive only if it is formed in the fiducial volume of ICAL. The fiducial volume in ICAL excludes top 4 layers of ICAL and 30 cm from all the sides of detector. Also, the track should have minimum 5 layer hit. With these condition we found that out of 6.48×10^{15} total number of muons there were 2 reconstructed tracks in the ICAL. This results in a false positive signal rate to be 0.015/day. The neutrino event rate of a ICAL sized detector is 4/day [5]. The false positive signal for SICAL is therefore 0.015/day with an upper bound of 0.05/day at 95% C.L. This makes SICAL a feasible proposition as the signal to noise ratio is ~ 80 .

Feasibility of using μ SR for internal magnetic field measurement at ICAL

The estimation of magnetic field inside the iron plates is crucial for reconstructing the momentum of neutrino. The magnetic field is usually measured by two techniques, method 1: as an average over a cross sectional area of the plate using the voltage induced in pickup coils wound around the plate and method 2: across gaps in a tiled magnetic layer by the use of an appropriately placed Hall probe. Measuring the magnetic field seen by a passing muon in the iron plate is a difficult problem. One possibility is to use the Muon Spin Rotation (μ SR) technique using stopped cosmic muons. The technique proposes to use cosmic ray muons, which have a partial longitudinal polarization. In view of this goal an iron plate (1 m \times 1 m \times 2 cm) was inserted within the gap between layer 2 and layer 3 in the cosmic ray muon stack of 12 RPCs at TIFR. GEANT4 based simulations have also been performed for the same to decide the thickness of iron plate. The simulation was done by incorporating full RPC stack geometry in GEANT4. Two different thicknesses of iron plate, 2 cm and 4 cm, were

investigated in the simulation. The detection efficiency of μ -decay is 31% and 16%, for 2 cm and 4 cm thick Iron plate respectively. Because of larger detection efficiency a 2 cm thick iron plate (placed between L3 and L2) was chosen in the experiment. The trigger was AND of L6, L5 and L4 which ensures that the muon has passed through the 3rd layer. For L2, the measured lifetime is $2.09 \pm 0.18 \mu\text{s}$. The muon lifetime could not be observed in L3 as the electric field goes down for a time ~ 10 msec around the region through which the muon has traversed, making a microsecond lifetime measurement impossible. Therefore, we moved to another small set-up with 5 layers of scintillators ($96 \times 32 \times 1 \text{ cm}^3$) with iron layer placed in between 3rd and 4th layer from the top. The trigger was generated by a coincidence of top three PSs within 50 ns time window and with anti-coincidence of PS just below the iron plate. The lifetime was measured in top and bottom PS to be 1.9 ± 0.2 (2.2 ± 0.2) μs , respectively. Asymmetry could not be measured in this set-up as a peak was observed at 400 ns in the decay spectrum. The second peak was caused due to ion-feedback in PMTs. To investigate the nature of signal due to ion-feedback, QDC measurements were also done without any conclusive results. Finally, the feasibility studies of μSR was performed for the mini-ICAL detector. Part of this work also involved active participation in the building of the mini-ICAL detector at Madurai with a team of engineers and researchers from INO collaboration. mini-ICAL is 85 ton detector which is magnetized by passing current through the copper coils, embedded in the magnet assembly. The magnetic field in mini-ICAL is currently measured by both the methods (1,2) described earlier. The Hall probe measurements show almost 90% of the detector with $B_{max} = 1.2 \text{ T}$ at a current of 900 A. The signal from μSR at mini-ICAL, could provide the first direct measurement of B-field

inside iron by using stopped cosmic muons.

List of Figures

1.1	A schematic showing various components of RPC.	6
1.2	The equivalent circuit of RPC.	8
1.3	The magnetic field map generated by Infolytica Magnet software in a $16\text{ m} \times 16\text{ m} \times 5.6\text{ cm}$ iron layer. The picture is taken from [23]. . .	10
1.4	A schematic showing the initial spin of muon while entering the system in the absence of any magnetic field.	15
1.5	A schematic showing the 180° spin oriented muon due to external magnetic field.	15
1.6	The schematic shows two extreme cases of pion decay in flight. The direction of pion momentum is towards right.	16
1.7	Cosmic pion energy spectrum. The picture is taken from [28]	17
2.1	One of the 14 PSs with WLS fibres (left) and ET enterprises 9807B PMT (right)	21
2.2	The circuit diagram for plateauing the hut scintillators.	23

2.3	The voltage versus efficiency plot of 3 hut paddles (H1,H2,H3) in the <i>left</i> figure and same plot for all four trigger paddles (N1,N2,N3,N4) in the <i>right</i> figure.	23
2.4	Picture of PS, before wrapping for MuL (<i>Left</i>) and MuS (<i>Right</i>). . .	24
2.5	Drawing of MuL set-up	25
2.6	3D model of trigger detector configurations and CMV hut. (a) CMV shield with 2 layers of scintillators on 4 walls and top with inner hut paddles (H1-H7) labeled in red and outer hut paddles (H8-H14) in black (b) CMV shield with 3 layers of scintillators on the top, with topmost layer paddles (H11,H12,H13) labeled in blue, middle layer paddles (H8,H9,H10) in black and bottom layer paddles (H3,H5,H6) in red and 1 layer of scintillators on the 4 walls labeled in red (c) MuL (d) MuS (e) MuS along with 3 Pb layers.	26
2.7	Photographs of the MuL (left) and MuS (right) trigger detectors inside the CMV detector with the top layers removed.	27
2.8	Screen shot of CRO showing the discriminated pulses of all the trigger paddles used to form trigger.	29
2.9	Screen shot of CRO showing three of the trigger paddles and the QDC gate window.	29
2.10	Logic diagram for 5-fold and 4-fold coincidence circuits.	30
2.11	QDC spectra of hut paddles.	30
2.12	QDC spectra of MuL trigger scintillators.	31
2.13	QDC spectra of MuS trigger scintillators.	32
2.14	TDC Spectra of trigger and CMV hut scintillators.	33
2.15	QDC spectra of MuL trigger scintillators with different thresholds. . .	35

2.16	Veto Efficiency as a function of time window.	37
2.17	(a) Exploded view showing placement of 3 scintillators on top of 5th layer RPC with pick-up panels shown in blue color and gas gap in grey color, (b) the positioning of scintillators in the RPC stack.	38
2.18	The inefficiency map of all hut scintillators. H6 was most inefficient (topmost right). Middle-left shows the inefficiency map of H6 after replacing the PMT.	39
2.19	Schematic view of mini-ICAL from top along with veto detector.	40
3.1	Schematic showing the geometry and placement of the blocks of rock and ICAL detector used in simulation.	46
3.2	A schematic of the SICAL detector at a depth of 103 m along with the CMVD.	47
3.3	Two-dimensional plot of incident muon energy E_μ and muon energy after 100 m rock E_μ' (left) and E_μ' distribution for 80 GeV (center) and 300 GeV (right) incident muon energy fitted to Crystal Ball fit function.	48
3.4	Cosmic muon energy spectra at different position as explained in the text.	48
3.5	Energy and theta spectra of neutrons (left top and left bottom) and K_L^0 s (right top and right bottom). Blue histogram shows the total neutrons (or K_L^0 s) coming out of rock and red histogram shows neutrons (or K_L^0 s) coming out without any accompanying charged particle.	50
3.6	Event rate estimation for ICAL detector taken from Ref. [5]	56

3.7	A schematic representation for the geometry used for the first part of the simulation. 3D cartoon picture (<i>left</i>), 2D side view (<i>center</i>) and top view (<i>right</i>).	58
3.8	The position distribution, (x,y) of events at the rock surface for N_0 (<i>left</i>), N_1 (<i>center</i>) and N_2 (<i>right</i>).	59
3.9	E (<i>top</i>), θ (<i>center</i>) and ϕ (<i>bottom</i>) distribution for N_0 (<i>left</i>), N_1 (<i>center</i>) and N_2 (<i>right</i>) for event selections N_0 , N_1 , N_2 as described in the text.	59
3.10	A schematic representation for the detector geometry used in the second part of the simulation.	60
3.11	The vertices of all the muon-nuclear interaction in different views.	62
3.12	Energy and theta spectra of neutrons (left top and left bottom) and K_L^0 s (right top and right bottom).	62
3.13	Reconstructed tracks of the two false positive events in the ICAL detector obtained from the simulation.	64
4.1	The mini-ICAL detector at IICHEP, Madurai.	70
4.2	A schematic showing the concrete base (gray color) with 12 different sizes pedestals (white color) along with two copper coils.	71
4.3	Schematic picture of four different sizes of iron plates used in m-ICAL (left) and placement of iron plates in a 4 m \times 4 m layer (right).	72
4.4	U section of the copper coil (left) and a schematic showing full coil after brazing both the section	73
4.5	Screenshot of the operating control panel of the magnet power supply.	74

4.6	The magnetic field inside one iron plate generated from MagNet software.	75
4.7	Schematic showing placement of Hall probes (<i>left</i>) and search coil (<i>right</i>) in iron plate.	76
4.8	B-I graph measured from one of the Hall probe strip located in the center of plate D and C1.	77
4.9	Closed loop gas system.	81
4.10	NINO (left) and ANUSPARSH (right) along with board.	82
4.11	Pressure vs time curve for one of the RPC gas gaps. The Red curve is for the RPC pressure and the Black curve is for ambient pressure.	86
4.12	Copper and brass jig for measuring the surface resistance of the graphite coating paint (top row), the middle row shows the surface resistance of one side of the gas gaps with 'H' and 'I' orientation of the jig and the other side is shown in the bottom row.	87
4.13	I-V characteristics of one of the RPC.	88
4.14	Few bend tracks in the m-ICAL detector at I=900 A	89
4.15	The trigger efficiencies of all the ten layers of RPC.	90
5.1	12 layer stack of RPC.	93
5.2	The geometry of the RPC stack and detector hall in 3D view, top view, side view and the schematic showing the RPC stack along with 2 cm thick iron plate placed in between layer 2 and layer 3. (<i>anti-clockwise from top left</i>)	94
5.3	The E, θ, ϕ spectra input to the simulation.	95
5.4	96

5.5	Schematic of the data acquisition system for 12 layer RPC stack.	97
5.6	Timing diagram of the separate TDC connected to layer 2 and layer 3.	99
5.7	Examples of tracks from the RPC stack. <i>Left</i> A track passing through all the layers of the stack. <i>Middle</i> An example of noisy event. <i>Right</i> A possible candidate of a decay event.	100
5.8	Time distribution of layer 2 (<i>Left</i>) and layer 3 (<i>Right</i>).	101
5.9	Set up of 5 layer PS stack (above) and the associated electronics (below).	102
5.10	Time distribution of top (<i>Left</i>) and bottom (<i>Right</i>) scintillators.	104
5.11	Screenshot form CRO showing ion feedback pulses for new and old PMTs.	104
5.12	The timing diagram for the changes in the HPTDC of RPC-DAQ module	106
5.13	Time distribution of μ^- (<i>Left</i>) and μ^+ (<i>Right</i>) scintillators.	108
5.14	The FFT of the timing spectrum for μ^+ (<i>left</i>). The plot of the ratio between the number of counts in each bin and the value obtained from the fit function (<i>right</i>).	108
5.15	Candidate muon decay events in layer 5 (a-d) and 4 (e-h).	110
5.16	Candidate muon decay events in layer 3 (a-d) and 2 (e-h).	111
5.17	Candidate muon decay events in layer 1 (a-d) and 0 (e-h).	112

List of Tables

1.1	Neutrino oscillation parameters	3
1.2	Summary of few experiments which measured cosmic muon polarization.	18
2.1	Grooves specifications in hut and trigger paddles.	22
2.2	Description of all detector configurations.	27
2.3	Various OR rates.	28
2.4	CMV efficiencies for individual parts of the detector at -20 mV threshold for configuration I and II.	33
2.5	Veto efficiencies for different thresholds of configuration III.	34
2.6	Veto efficiencies of configuration IV at -100 mV threshold for the trigger detectors.	36
3.1	Fraction of neutral secondaries produced in muon nuclear interaction.	49
3.2	Events (or particles) distribution of neutrons and K_L^0 for 10^{10} muons incident on the last 3 m of rock.	52

3.3	Break up of events with a specified number of charged particles (q) and neutral particles (n) for 10^{10} muons interacting with the last 3 m rock just above ICAL	54
3.4	Characteristics of the two events that are false positive signal at SICAL. V_x and V_y denotes the x and y position of the vertices of the reconstructed track.	64
4.1	Chemical, mechanical and magnetic properties of soft iron plates procured from HISSAR company.	71
4.2	The table summarizes all the components involved in the assembly of m-ICAL magnet assembly.	74
4.3	Spacer and plate layout.	77
4.4	Comparison of magnetic field from simulation and measured using search coil.	78
4.5	Specifications of NINO and ANUSPARSH	82
5.1	Parameters of the simulation	95

List of Abbreviations

α	Alpha
β	Beta
γ	Gamma
μSR	Muon Spin Rotation
ν_{μ}	Muon Neutrino
AFE	Analog Front End
ALICE	A Large Ion Collider Experiment
BARC	Bhabha Atomic Research Center
BeCu	Beryllium Copper
CAEN	Costruzioni Apparecchiature Elettroniche Nucleari S.p.A
CAMAC	Computer-Aided Measurement And Control

CAM	Control And Monitoring
CAU	Calibration and Auxiliary Unit
CC	Charge Current
CDR	Control/Data Router
CLGS	Closed Loop Gas System
CMVD	Cosmic Muon Veto Detector
CMV	Cosmic Muon Veto
CMZAS	Cosmic Muon Zenith Angle Spectrum
CORSIKA	COsmic Ray SIMulations for KAscade
CPT	Charge Conjugation Parity Time
CP	Charge Conjugation and Parity
DAQ	Data Acquisition
DFE	Digital Front End
ECL	Emitter Coupled logic
EMI	ElectroMagnetic Interference
FEM	Finite Element Methods
FIFO	First In First Out
FTM	Final Trigger Module

GaAs	Gallium Arsenide
GEANT4	GEometry ANd Tracking-4
GeV	Giga Electron Volt
GTLB	Global Trigger Logic Board
GUI	Graphical User Interface
HMC	Hybrid Micro Circuit
HPTDC	High Performance Time to Digital Converter
HV	High Voltage
ICAL	Iron Calorimeter
IDAQ	ICAL Data Acquisition
IH	Inverted Hierarchy
IICHEP	Inter Institutional Institute for High Energy Physics
INO	India based Neutrino Observatory
KGF	Kolar Gold Field
LAN	Local Area Network
LCWCS	Low Conductivity Water Cooling System
LVDS	Low Voltage Differential Signal
LV	Low Voltage

MeV	Mega Electron Volt
MIP	Minimum Ionizing Particle
MLU	Multiple Logic Unit
Mu2e	Muon-to-Electron Conversion Experiment
NIM	Nuclear Instrumentation Module
NOνA	NuMI Off-axis ν_e Appearance
Pb	Lead
PCB	Printed Circuit Board
PMT	Photo Multiplier Tube
PPS	Pulse Per Second
PS	Plastic Scintillator
QDC	Charge to Digital Converter
RPC	Resistive Plate Chamber
RTC	Real Time Clock
SF₆	Sulfur hexafluoride
SICAL	Shallow depth Iron Calorimeter
SIO₂	Silicon Di Oxide
SiPM	Silicon Photo Multiplier

SM	Standard Model
SRB	Signal Router Board
T2K	Tokai to Kamioka
TCAM	Trigger Control And Monitoring
TDC	Time to Digital Converter
TIFR	Tata Institute of Fundamental Research
TLB	Trigger Logic Board
TOF	Time Of Flight
TTR	Time/TDC router
WLS	Wave Length Shifting

Introduction

1.1 Neutrinos

Neutrinos are weakly interacting fundamental particles with spin $1/2$ and vanishingly small mass. Neutrinos were first postulated by Pauli in 1930 to explain the continuous energy spectrum of the beta particle emitted in a radioactive decay [1]. To conserve momentum and energy in the nuclear beta decay process, he suggested that a massless, or a very light, neutral particle is emitted together with the electron, which shares the transition energy, but escapes detection. Soon after in 1934, Fermi gave the theory of beta decay assuming the neutrino to be a spin $1/2$ particle [10]. In 1956 F. Reines and C. Cowan first experimentally detected the electron antineutrino from a nuclear reactor [11]. Madam C. S. Wu in 1956 showed that the parity is violated in the weak interaction, implying that only left handed neutrinos or right handed anti-neutrinos exist [12]. Lederman, Schwartz, Steinberger detected the muon-neutrino in an accelerator experiment in 1962 [13]. The detection of atmospheric neutrino was first realized in the

Kolar gold fields in 1965 [14] and shortly thereafter by Reines and collaborators at a South African mine [15]. Ray Davis in 1965 experimentally measured the solar neutrino flux for the first time [16]. However, he was detecting only 1/3 of what is expected from the theoretical calculations. Initially, the theoretical model for the sun was suspected to be wrong. However, subsequently other experiments also observed a similar deficiency in the solar neutrino flux [17]. This puzzle is popularly known as the solar neutrino puzzle. This puzzle was finally understood by invoking the phenomenon called neutrino oscillation where the neutrinos oscillate among the flavour states as they propagate. The flavour eigenstates (ν_e, ν_μ, ν_τ) can be represented as a super-position of three masses eigenstates (ν_1, ν_2, ν_3) with mass m_1, m_2 and m_3 as

$$|\nu_l\rangle = \sum_i U_{li}^* \nu_i \quad (1.1)$$

where $l = e, \mu, \tau$ is the index for the flavour eigenstates and $i = 1, 2, 3$ is the index for the mass eigenstates. The mixing matrix U is has the form

$$U = \begin{bmatrix} c_{12}c_{13} & s_{12}c_{13} & s_{13}e^{-i\delta_{13}} \\ -s_{12}c_{23} - c_{12}s_{23}s_{13}e^{i\delta_{13}} & c_{12}c_{23} - s_{12}s_{23}s_{13}e^{i\delta_{13}} & s_{23}c_{13} \\ s_{12}s_{23} - c_{12}c_{23}s_{13}e^{i\delta_{13}} & -c_{12}s_{23} - s_{12}c_{23}s_{13}e^{i\delta_{13}} & c_{23}c_{13} \end{bmatrix} \quad (1.2)$$

$$\times \text{diag}(e^{i\lambda_1}, e^{i\lambda_2}, e^{i\lambda_3})$$

where c_{ij} and s_{ij} are $\cos \theta_{ij}$ and $\sin \theta_{ij}$, respectively, θ_{ij} are the mixing angles, δ_{CP} is the CP phase angle (CP is not conserved if it is not equal to 0 or 180 degrees) and λ_i are the Majorana phases and are non-zero only if neutrinos are Majorana particles. The probability that a neutrino ν_α of energy E will oscillate

into ν_β after traversing a distance L can be expressed as

$$P_{\nu_\alpha \rightarrow \nu_\beta}(L, E) = \delta_{\alpha\beta} - 4 \sum_{i>j} \text{Re} (U_{\alpha i}^* U_{\beta i} U_{\alpha j} U_{\beta j}^*) \sin^2 \left(\frac{\Delta m_{ij}^2 L}{4E} \right) + 2 \sum_{i>j} \text{Im} (U_{\alpha i}^* U_{\beta i} U_{\alpha j} U_{\beta j}^*) \cos \left(\frac{\Delta m_{ij}^2 L}{2E} \right) \quad (1.3)$$

Two mass square differences have been measured and the global fit values are shown in Table. 1.1 Various neutrino oscillation experiments with solar, atmo-

TABLE 1.1: Best neutrino oscillation parameters obtained from global fit [18]. bfp corresponds to Best Fit Parameter.

Parameter	Normal hierarchy		Inverted hierarchy	
	bfp $\pm 1 \sigma$	3σ range	bfp $\pm 1 \sigma$	3σ range
$\sin^2 \theta_{12}$	$0.310^{+0.013}_{-0.012}$	0.275→0.350	$0.310^{+0.013}_{-0.012}$	0.275→0.350
$\theta_{12}/^\circ$	$33.82^{+0.78}_{-0.76}$	31.61→36.27	$33.82^{+0.78}_{-0.76}$	31.61→36.27
$\sin^2 \theta_{23}$	$0.580^{+0.017}_{-0.021}$	0.418→0.627	$0.584^{+0.016}_{-0.020}$	0.423→0.629
$\theta_{23}/^\circ$	$49.6^{+1.0}_{-1.2}$	40.3→52.4	$49.8^{+1.0}_{-1.1}$	40.6→52.5
$\sin^2 \theta_{13} (10^{-3})$	$22.41^{+0.65}_{-0.65}$	20.45→20.45	$22.64^{+0.66}_{-0.66}$	20.68→2.463
$\theta_{13}/^\circ$	$8.61^{+0.13}_{-0.13}$	8.22→8.99	$8.65^{+0.13}_{-0.13}$	8.27→9.03
$\delta_{CP}/^\circ$	215^{+40}_{-29}	125→392	284^{+27}_{-29}	196→360
$\frac{\Delta m_{21}^2}{10^{-5} eV^2}$	$7.39^{+0.21}_{-0.20}$	6.79→8.01	$7.39^{+0.21}_{-0.20}$	6.79→8.01
$\frac{\Delta m_{3l}^2}{10^{-3} eV^2}$	$+2.525^{+0.033}_{-0.032}$	+2.427→+2.625	$-2.512^{+0.034}_{-0.032}$	-2.611→-2.412

spheric, accelerator and nuclear reactor neutrinos have measured the neutrino oscillation parameters and the global fit data is summarized in Table1.1. It can be seen from the Table1.1 that though the absolute value of Δm_{32}^2 is known, the sign is not yet known. This allows two ways of ordering in the mass eigen values namely normal hierarchy (NH) with $m_1 < m_2 < m_3$ or inverted hierarchy with $m_3 < m_1 < m_2$. A worldwide effort is underway in order to fix the mass ordering with precise measurements of the neutrino oscillation parameters using different

detection techniques and different neutrino sources [19]. A review of the current and future experiments aiming to make precise measurements of the neutrino oscillation parameters can be found in [20].

1.2 ICAL

The India-based Neutrino Observatory (INO) is aiming to build a world-class underground laboratory with a vertical rock cover of ~ 1200 m for non-accelerator-based high energy physics, astrophysics and nuclear physics experiments requiring a low-background environment. The primary goal of this project is to study various properties of neutrinos using natural and lab made neutrino sources. In the last few decades there has been a tremendous growth in the field of neutrino physics. Yet many mysteries remain unresolved. Recent experiments have conclusively shown that at least two neutrinos possess a small but finite mass [21]. It is also found that the neutrinos oscillate from one flavour to other as they propagate. Many experiments have been performed to make a precise determination of the various parameters that determine this oscillation and the best obtained values are tabulated in Table 1.1. Importantly, the sign of the Δm_{atm} is not known. This allows for two different hierarchies, namely, normal or inverted hierarchy. To address some of these issues a 51 kton magnetized iron calorimeter detector is proposed to be built and housed at the INO site. Since ICAL is going to be a magnetized detector it will, unlike water Cerenkov detectors such as the 50 kton Super Kamiokande detector, be able to distinguish neutrino and antineutrino events. Some of the important physics goals of INO-ICAL are:

a) Address and help to solve the mass hierarchy problem using the matter effect.

- b) Precise measurement of θ_{23}
- c) Search for long range neutrino interactions, search for anomalous KGF events.

ICAL will be comprising of a total of 151 layers of iron enclosing 150 layers of RPCs[22] in the gaps. The thickness of each iron plates is planned to be 5.6 cm. The plates will be stacked on top of each other with a gap of 4 cm in between two consecutive layers. RPCs will be placed in these gaps. The total dimension of ICAL is 48 m (length) \times 16 m (width) \times 14.5 m (height) which is composed of 3 modules of dimension 16 m \times 16 m \times 14.5 m. In each layer of the ICAL, there will be 64 RPCs with a total of 28,800 RPCs overall. The number of electronic channels to be readout are 3.7×10^6 . The unit size of RPC which will be used in ICAL is $\sim 2 \text{ m} \times 2 \text{ m}$ and the design is described in the next section.

1.2.1 Resistive Plate Chamber (RPC)

RPC is a gaseous detector which works on the principle of ionization. It has a very good time resolution (comparable to plastic scintillator detector) and can give for position information about the ionizing particle. RPCs are being used in various cosmic ray and high energy physics experiments for timing and trigger generations. The energy deposited in the detector cannot be measured by the RPC because of the avalanche mode of operation. However, they are best for experiments where muon measurements are required. A muon with energy between about 1 and 100 GeV loses energy in a medium close to that of a minimum ionizing particle (MIP) and deposits roughly the same amount of energy every time in a given thickness of matter. This makes it eminently

suitable for ICAL where the neutrino will be detected indirectly by detecting the secondary muon. Another advantage of the RPC detector is its large coverage area at less expense as the cost per unit area is low in comparison to other particle detectors.

Construction

RPCs for the ICAL are constructed by sandwiching two glass plates of 3 mm thickness with a volume resistivity $10^{12} \Omega\text{-cm}$ and sealing all 4 sides to form a chamber. A uniform gap of 2 mm is maintained using polycarbonate spacers. Inlet and outlet paths are provided for flowing of gas. The chamber is flushed with gas mixture, where R134a is the main component and iso- C_4H_{10} and SF_6 (94.5%, 4.2% and 0.3% by volume, respectively) for photon and electron quenching, respectively. The gas is at a pressure of a few mbar above atmospheric pressure. Both top and bottom glasses are coated on the outside with conductive coating with uniform surface resistance of the order $1\text{M}\Omega/\square$. On application of high voltage $\sim 10\text{ kV}$ on glass electrode, a uniform electric field is created across the two plates inside the chamber. A schematic of RPC is shown in Fig. 1.1.

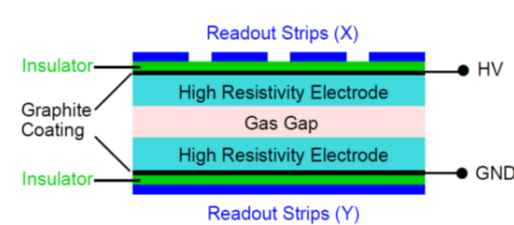


FIGURE 1.1: A schematic showing various components of RPC.

Principle

When the charged particle traverses the gas gap, it ionizes the gas as a result of which free electrons are produced. These free electrons move towards the anode as shown in the figure. The change in field due to the electron motion results a local discharge over about 0.1 cm^2 on the electrodes. This tiny discharge area is due to the high resistivity of glass electrode and quenching characteristics of the gas. The discharge induces electrical signals on external pickup strips on both sides orthogonal to each other as shown in figure, which can be used to record the location and time of ionization. To insulate pickup strips from high voltage graphite coating Mylar sheets of suitable thickness are used. The discharge area recharges slowly through the high resistivity glass plates and the recovery time is about (0.01 - 0.1) sec. The discharge area will be inactive for the dead time of the detector. The motions of positive ions are very slow, so for all particle interactions, RPC signals produced due to the motion of ion are negligible.

Modes of Operation

RPCs can be operated in two modes depending on the potential applied and ionization phenomenon viz. in the Avalanche mode and in the Streamer mode.

a) Avalanche mode: The gas mixture and potential are such that the avalanche produced by charged particle passing through the gas gap stops after sometime. This can be achieved by adding a suitable electron affinity gas SF_6 and optimum high voltage across the plates. Hence, the avalanche is controlled and discharge spread on the electrodes is of the order of 0.1 cm^2 . This reduces the dead time and dead space of the RPC. This makes the avalanche mode RPCs more suitable

for high rate experiments. A typical pulse amplitude is a few mV for a gas gain approximately 10^6 . The standard gas composition for the avalanche mode in an RPC is R134a 95.2%, iso- C_4H_{10} 4.5% and SF_6 0.3%.

b) Streamer mode: This mode can be achieved by removing the electron quenching gas and using an appropriate gas mixture. A standard gas composition for the streamer mode RPC is R134a 62%, Argon 30% and iso- C_4H_{10} 8%. The secondary ionization continues until there is a gas breakdown and a continuous discharge takes place, resulting in a very high gain of the order of 10^8 with amplitude going up to 100-200 mV. Due to the relatively long relaxation time of the resistive electrode, this mode is adequate for cosmic ray and low-rate accelerator experiments. RPCs operating in avalanche mode may also form streamers, however, this probability is reduced with the increase of fraction of electronegative gas.

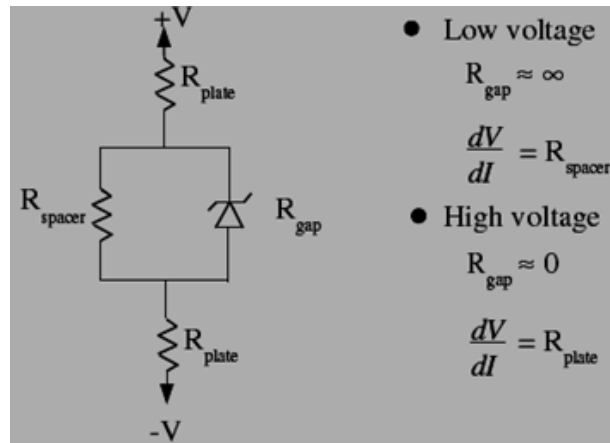


FIGURE 1.2: The equivalent circuit of RPC.

The equivalent circuit of RPC detector is shown Fig. 1.2. The conduction of charge mainly goes through the spacers because the resistance between the two glass plates R_{gap} is very high compared to R_{spacer} . As the voltage increases

the applied field between the gap increases results in increase of free electrons and reduces the gap resistance R_{gap} . At this moment the conduction takes place between the top plate and bottom plate via the gas gap.

1.2.2 ICAL Magnet

The ICAL magnet is designed for a magnetic field of 1.5 T in the iron and which is piecewise continuous in each of the 151 layers. The challenges in designing such a magnet were a) power efficiency, b) uniformity of the B-field and c) the generation of $B \sim 1$ T over a large fraction of the total volume of 51 kTon iron. The tile size of the iron plate was optimized to be $4\text{ m} \times 2\text{ m} \times 0.056\text{ m}$ as a good trade off between mechanical constraints imposed by cavern size and power economy in generation of magnetic field as described in [23]. The magnetic field profile with having continuous slots and containing four coils at 20 kA-turns was simulated by Infolytica MagNet software as discussed in [23] and is shown in Fig 1.3.

The ICAL will be sensitive to charge current (CC) interactions of ν_μ and its detection of is via detection of the charged muon in the final state. For example, a ν_μ , after interacting with iron, will give a μ^- as a final state particle. Depending upon the type of CC interaction, quasi elastic (QE) or deep inelastic (DIS), the nature of the final state particles and hence the hit pattern will change. For example in the case of the QE reaction, the muon will carry almost all the ν energy and only long tracks due to muon will be observed. Whereas in case of DIS, a part of ν energy will be given to the muon and rest will be shared between the hadrons produced. An event in ICAL comprises of the position and

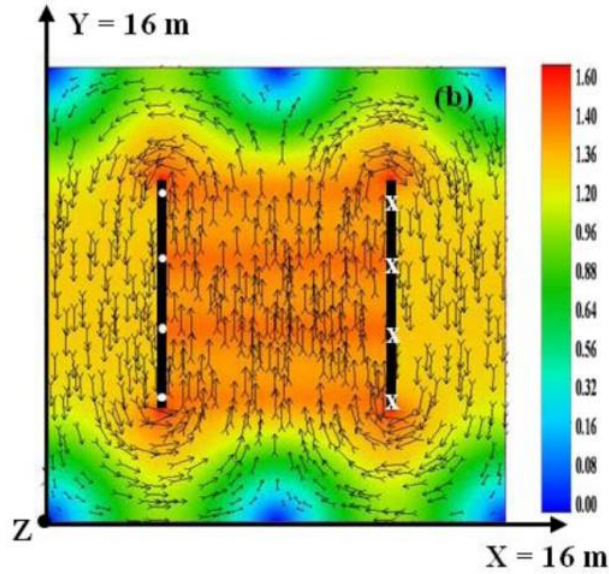


FIGURE 1.3: The magnetic field map generated by Infolytica Magnet software in a $16\text{ m} \times 16\text{ m} \times 5.6\text{ cm}$ iron layer. The picture is taken from [23].

time information arising from the charged particle interacting with the RPCs in their path. In case of QE reactions the muon tracks, with typically 1 to 2 hit per RPC (the average hit multiplicity in RPC is ~ 1.8 [24],[25]), will be observed. However in case of the DIS reaction, apart from the muon track, a cluster of hits due to hadrons will be observed. The fitting of tracks to the observed hits in the ICAL reconstruction code is performed using the Kalman filter technique. After fitting, the reconstruction efficiency of muons is observed to be more than 90% for energies above 2 GeV whereas the charge identification efficiency is found out to be 95%. The energy resolution of hadrons is found to be about 85% (36%) at 1 GeV (15 GeV). The χ^2 analysis quantifying the reach of ICAL with respect to the neutrino mass hierarchy can be found in [26]. The analysis shows that by combining both the muon and hadron momentum information the wrong hierarchy can be rejected with a significance of $\chi^2_{ICAL_{MH}} = 9.5$ with 10 years

of exposure time for a 51 kTon ICAL. The analysis was performed for maximal mixing angle $\sin^2\theta_{23} = 0.5$ and $\sin^2\theta_{13} = 0.1$.

1.3 SICAL

The rock overburden above the ICAL at the Pottipuram site significantly reduces the background arising due to cosmic ray muons (by a factor of $\sim 10^6$). The reduction in cosmic ray muon flux at a depth of 100 m is about 100. Hence, if a cosmic muon veto detector (CMVD) with an veto efficiency of 99.99% is built around ICAL then it may be possible to perform the ICAL experiment at a shallow depth (~ 100 m). The shallow depth ICAL (SICAL) will then have same the background due to muon as at the proposed INO site. At shallow depths, the most significant background is due to cosmic ray muons which can be vetoed with a high veto efficiency. However, the secondaries generated due to the muon-nucleus interaction with the rock material can be a serious concern and this aspects needs to be carefully investigated. High energy cosmic muons can undergo an inelastic interaction with the nucleus or could be absorbed. The secondary neutral particles produced in such interactions could escape detection in the veto detector and give rise to events in the ICAL that could mimic a neutrino interaction. The SICAL is a worthwhile proposition if the number of such false positives are reduced to a level that is significantly lower than the true positives (i.e. genuine neutrino events). While the outer parts of the ICAL detector could be used for this purpose it might be more efficient and versatile if one builds an efficient muon veto detector to identify and reject cosmic muon events. Such a detector could, if suitably configured, also be used for other physics. It may

therefore be appropriate to mention some of possible advantages of the SICAL detector viz.

- (1) a much larger choice of sites
- (2) much larger caverns, allowing much larger iron calorimeter detectors for neutrino science as well as applications such as neutrino tomography of the earth.
- (3) monitoring of RPCs using the much larger muon flux at 100 m depth as compared to that at 1 km depth
- (4) if shown to be feasible, using muon spin rotation to get additional information on the internal magnetic field [27]
- (5) increase the fiducial volume of ICAL,
- (6) enhancing the sensitivity for exotic searches such as verifying or falsifying the anomalous KGF events [14] and cosmogenic magnetic monopoles [6] using the CMVD and the ICAL.

It may be pointed out that while the present study was being carried out a large CMV system had already been designed for the Mu2e experiment at Fermilab.

1.4 mini-ICAL

Before building any detector it is necessary to study, validate and optimize various R & D issues on a smaller scale. For this purpose, prototypes need to be built as they help in understanding and studying the major engineering and technology aspects involved in constructing of a large detector like ICAL. Similar reasons led to the building of 4 prototypes, 2 stacks of RPCs of areas 1 m^2 and 4 m^2 each, and 2 with magnetized ICAL detectors. The fourth prototype whose design was very

similar to the ICAL design was commissioned at the Inter-Institutional Center for High Energy Physics (IICHEP), INO transit Campus at Madurai, Tamil Nadu and referred to hereafter as mini-ICAL or m-ICAL. It is 600 times smaller than the proposed ICAL detector at INO. The key role of mini-ICAL was to perform a detailed investigation of engineering and technological challenges which were anticipated to occur in ICAL such as:

- 1) Study the performance of the detector (RPC) and electronics in the presence of the magnetic field
- 2) Study the long term performance and stability of various detector components of mini-ICAL
- 3) Mechanical issues in handling of soft iron plates (including transportation) and assembly of the detector
- 4) In-situ brazing of copper coils and their performance
- 5) Comparison of simulated and measured magnetic field.

Along with this, there are various other uses of such a device. As it is an overground detector, we can study cosmic muons with mini-ICAL. The proposed physics goals were following :

- 1) to check the feasibility of muon spin rotation technique to estimate the internal magnetic field inside iron plates at ICAL
- 2) to study the efficiency of a large sized CMV detector covering mini-ICAL
- 3) to measure the angular and energy distributions of cosmic ray muons of either charge separately, which can provide useful inputs for improving neutrino flux simulations for Pottipuram.

1.5 Muon spin rotation

1.5.1 Basic principle

The decay of pion at rest results in a spin polarized muon. When such a spin polarized muon beam decays in an absorber (in the absence of magnetic field), placed between two detectors as shown in Fig. 1.4, the decay electron will be mostly detected in the back detector. This origin of this asymmetry is due to the parity non-conservation in the weak decay of a spin polarized muon. The application of an external magnetic field to such a system can lead in precession of muon spin before it decays as a result of which the probability of detecting the decayed electron in the front detector becomes non-zero. By observing the time difference between the muon arrival and the decay of muon, the lifetime of the muon can be measured. In a magnetic field the muon spin precesses leading to a time dependent sinusoidal modulation of the asymmetry. The oscillation frequency corresponds to the Larmor precession frequency which is directly proportional to the magnetic field at the location of the muon B_{loc} as:

$$\omega = \gamma B_{loc} \quad (1.4)$$

where γ is the gyromagnetic ratio given by $\frac{e-g}{2m}$, e being the charge of the muon, g the Lande g -factor and m , the mass of the muon. This phenomenon is called muon spin rotation which can be used to measure the magnetic field inside the sample or absorber.

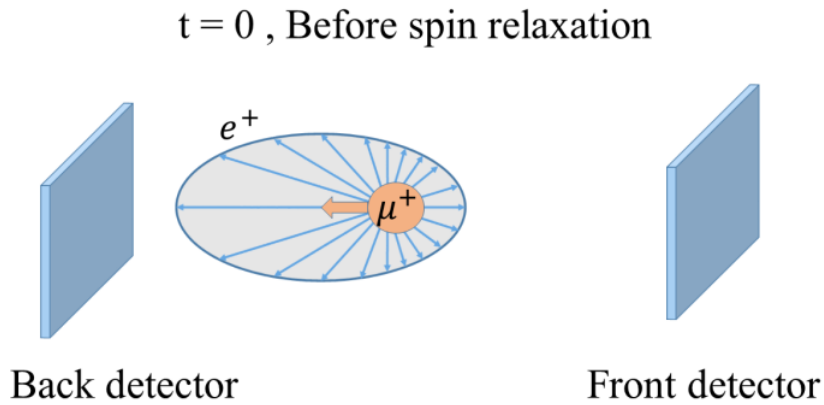


FIGURE 1.4: A schematic showing the initial spin of muon while entering the system in the absence of any magnetic field.

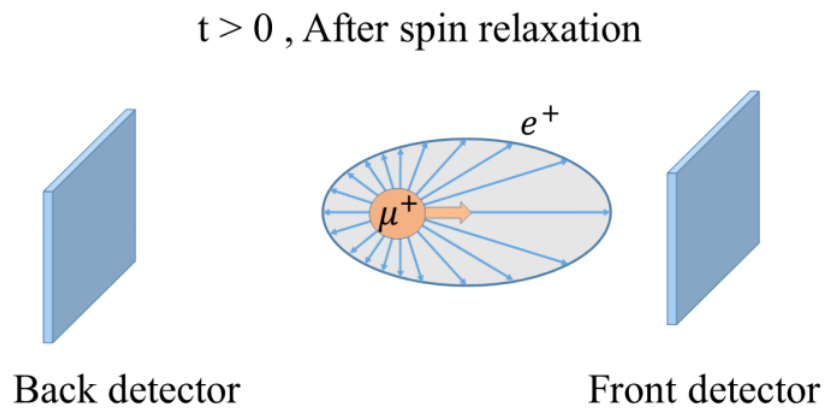


FIGURE 1.5: A schematic showing the 180° spin oriented muon due to external magnetic field.

1.5.2 Polarization of cosmic ray muon

The steep energy dependence of cosmic pion energy spectrum [2] is responsible for partial longitudinal polarization of the muon [3]. Let us consider two extreme cases of pion decay in flight. As shown in Fig. 1.6, Case 1 happens when the muon is emitted backward in the rest frame of the pion and Case 2 happens when the muon is emitted forward. The reason for considering the above two cases is to succinctly express the origin of polarization in cosmic muons. Though all

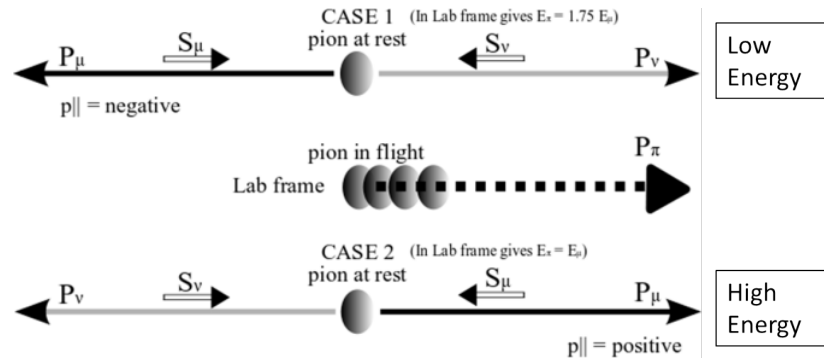


FIGURE 1.6: The schematic shows two extreme cases of pion decay in flight. The direction of pion momentum is towards right.

intermediate cases corresponding to intermediate energies of pions are possible in reality, let us assume for a moment that only these two cases are possible. Now since the Lorentz transformation of muon momentum to the laboratory frame does not alter its spin direction, if pions of these extreme case energies are equally produced, then the net polarization is zero. That is we get an equal number of forward and backward polarized muons. On the other hand an asymmetry in the energy spectrum would directly lead to a net polarization since the lower energy pions decaying into muons in the same direction is more in number than the higher energy pion decaying into a muon in the opposite direction. It is easier to extend the argument to the intermediate cases to see that a polarization is possible if the energy spectrum is not flat. In fact the energy spectrum of cosmic pions is a distribution that falls off sharply with increasing pion energy as shown in Fig. 1.7. The partial longitudinal polarization of cosmic-ray muons can be measured by stopping the muons in absorber and by observing the asymmetry in the distribution of their decay electrons. The angular distribution of the decay electrons is of the form $1 + aP\cos\theta$ (where a is the asymmetry coefficient and θ is the angle between the muon momentum direction (i.e. vertically downward)

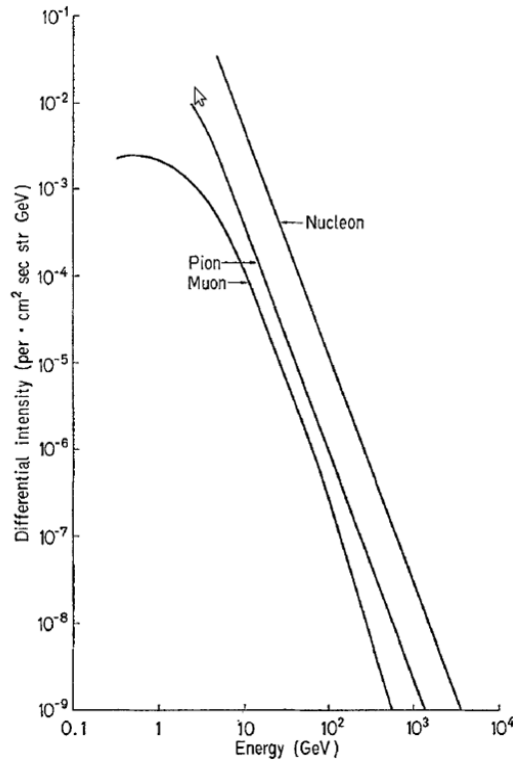


FIGURE 1.7: Cosmic pion energy spectrum. The picture is taken from [28]

and the momentum direction of the decay electron, and P is the degree of muon polarization. The up-down asymmetry R is related to the muon polarization P by the expression $\frac{U}{D} = R = \frac{1+a'P}{1-a'P}$ where a' is the effective asymmetry coefficient depending upon the decay electron energy and the experimental configuration, and U and D are respectively the numbers of electrons moving into the upward and downward hemispheres. Various experiments have observed the partial polarization of cosmic muons and a summary is given in the Table 1.2.

1.5.3 μ SR with cosmic muons

μ SR is a standard condensed matter technique to study the internal magnetic field in small samples using secondary beams of polarized muons [6]. Measuring the

TABLE 1.2: Summary of few experiments which measured cosmic muon polarization.

Group	Detector	Absorber	R
Fowler (1958) [29]	Plastic scintillator	Al/NaCl	1.14 ± 0.07
S.Johnson (1961) [30]	Plastic scintillator	Fe/Cu/S	1.18 ± 0.02 ($P_\mu = 0.31 \pm 0.03$)
S.N.Sen Gupta (1961) [31]	Cloud Chamber	Cu	1.17 ± 0.04 ($P_\mu = 0.34 \pm 0.09$)

magnetic field seen by a passing muon in the iron plate is still an open problem. The Muon Spin Rotation (μ SR) technique using stopped cosmic muons is one possibility of addressing this problem.

The thesis is organized as follows. Chapter 2 describes the construction and performance of a small cosmic muon veto (CMV) detector of dimensions $1 \text{ m} \times 1 \text{ m} \times 0.3 \text{ m}$. Chapter 3 presents results of a Monte Carlo study to estimate the contribution of this background and compare it with the event rate expected from atmospheric neutrinos for a shallow depth ICAL (SICAL) detector. In chapter 4, the commissioning of a 85 ton magnet prototype of the ICAL along with basic characterization tests of the RPC are described. The results of muon lifetime measurement with three different experimental setups are described as also an attempt to use the muon spin rotation technique to try to get some information about the magnetic field in iron is presented in Chapter 5. Chapter 6 has a summary of the thesis.

A Compact Cosmic Muon Veto Detector

The key requirement for a shallow depth ICAL (SICAL) is making an efficient Cosmic Muon Veto (CMV) detector with a desired veto efficiency of 99.99%. With this goal in mind, a beginning was made by building a small CMV detector at TIFR using refurbished plastic scintillator detectors. Such a high efficiency veto detector can also be used for other experiments [32], [33] which require low cosmic muon background. The choice of detector is crucial in designing a CMV because the intrinsic efficiency of the detector should be very high in order to achieve the desired veto efficiency [34]. Moreover, multiple layers of the detector may be required to achieve this efficiency. Plastic scintillators [35] are the natural choice because of their reasonably high light output, fast scintillation decay time, low cost and ease of configuring with large areal coverage and almost no maintenance. Large area detectors are essential for making a veto detector that surrounds large detectors such as ICAL.

Even though scintillators are a good choice for making a veto detector there are a few challenges that have to be overcome in order to achieve the desired high veto efficiency.

1. gaps and dead regions between the detectors can be major source of inefficiency as the particles can simply skip detection at such spaces. Ideally, one should use a single, large area detector on each of the 5 surfaces. But this cannot be done in practice. Instead we can attempt to reduce the gaps between scintillator modules of a convenient size and have a staggered geometry so as to cover as much of the gaps as possible.
2. When the muon trigger fires in on a γ -ray or neutron induced event, there may be no detection in the CMV detector. This can then be falsely attributed to inefficiency of the CMV detector.
3. Proper care should be taken by adjusting the threshold, both in the muon trigger as well as the CMV detector, in order to cut down the noise pulses.

The CMV assembly comprises of two main blocks, (a) the hut of plastic scintillator (PS) and (b) the muon trigger set-up. Two different sizes of PSs were used for the muon trigger whereas the hut paddles were the same throughout the course of the work. Firstly, a small trigger set-up was made by stacking 4 PSs one top of another. Next the trigger set-up was covered by a 5-sided scintillator hut. 4 PSs were placed to form 4 "walls" around the trigger set-up and 3 PSs were kept at the top forming the "ceiling". A layer of 3 cm thick lead was kept in between second and third PS of the muon trigger. The layer of Pb was kept in order to reduce coincidences due to low energy particles other than muon. A 4-fold coincidences in the trigger set-up ensures that the muon has passed through the CMV assembly. With this 4-fold coincidence as trigger we counted

the coincidences between the muon trigger and the PS hut. The veto efficiency is then the ratio of the 4-fold to 5-fold coincidence [36].

2.1 CMV assembly

CMV Hut Paddles

A small cosmic muon veto shield was made using 14 PSs of size 320 mm (width) \times 960 mm (length) \times 10 mm (thickness). The PS is made from *Bicron BC-408* with maximal emission wavelength at 425 nm. The attenuation length of the PS is 210 cm. Each paddle had grooves with dimension listed in Table 2.1. The Wavelength Shifting Fibers (WLS[37]) of diameter 1 mm, were used for light collection in the scintillator. 4 WLS fibers were placed in each groove and a total of 44 fibers were placed in 11 grooves. One such scintillator with all the fibers placed in the groove is shown in Fig. 2.1. All these fibers were



FIGURE 2.1: One of the 14 PSs with WLS fibres (left) and ET enterprises 9807B PMT (right)

collectively inserted in a "cookie" and used for the coupling of the fibers to the Photo Multiplier Tube (PMT). The scintillator was then wrapped with *Tyvek*TM *DuPont* sheet for achieving optimal light reflection. Further, the scintillator

TABLE 2.1: Grooves specifications in hut and trigger paddles.

Description	Trigger Paddle	Hut Paddle
Thickness	10 mm	10 mm
Groove Width	2 mm	4 mm
Groove Depth	2 mm	2 mm
Pitch	20 mm	30 mm
Fibers per groove	2	4

was covered by black opaque *Tedlar Polyvinyl Fluoride (PVF)* TM *DuPont* paper for shielding from external light. *Electron Tubes (ET 9807B)* make PMTs, were coupled with the scintillators. The 9807B is a 51 mm (2") diameter, end window photomultiplier with blue-green sensitive bi-alkali photo-cathode and 12 high gain, high stability, BeCu dynodes with linear focused design for good linearity and timing. The maximum quantum efficiency of the photo-cathode is 26% at about 400 nm which makes the PMT suitable for the scintillator used in the experiment. The scintillator, WLS fibers and PMT assembly were wrapped with black tape to prevent the ambient light entering the PS and also to provide some amount of physical protection. The applied HV to the PMT was varied to find the optimum operating value in the plateau region. The block diagram of the set-up is shown in Fig. 2.2 and the graph showing efficiency as a function of HV for three of PS is shown in Fig. 2.3. The operating HV was set to be 1900 V for all the hut paddles which is well on the plateau region as can be seen from the Fig. 2.3. These paddles were arranged in the form of an inner and outer cosmic veto "hut" each with 4 "walls" consisting of 4 paddles standing on the long edge forming a footprint of a square of inner dimension about 920 mm and 3 paddles forming the "ceiling". The top of the outer hut had paddles placed in a direction perpendicular to the ones in the inner hut "ceiling" as shown in Fig. 2.6a.

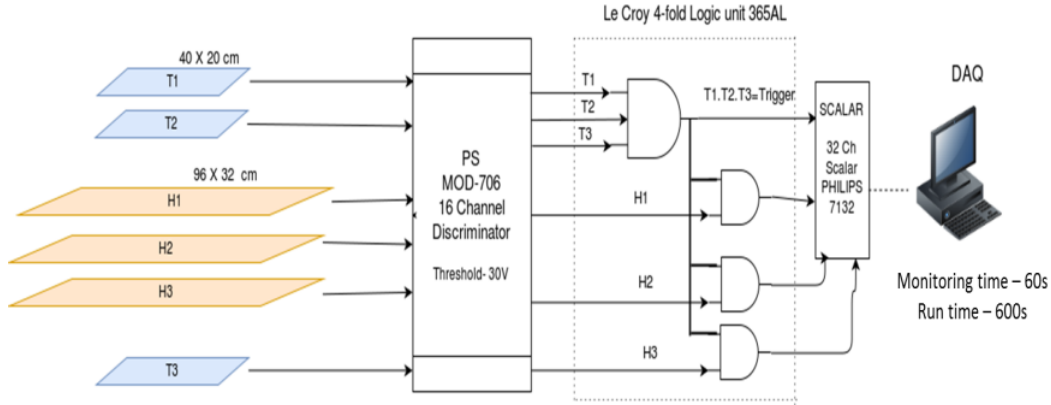


FIGURE 2.2: The circuit diagram for plateauing the hut scintillators.

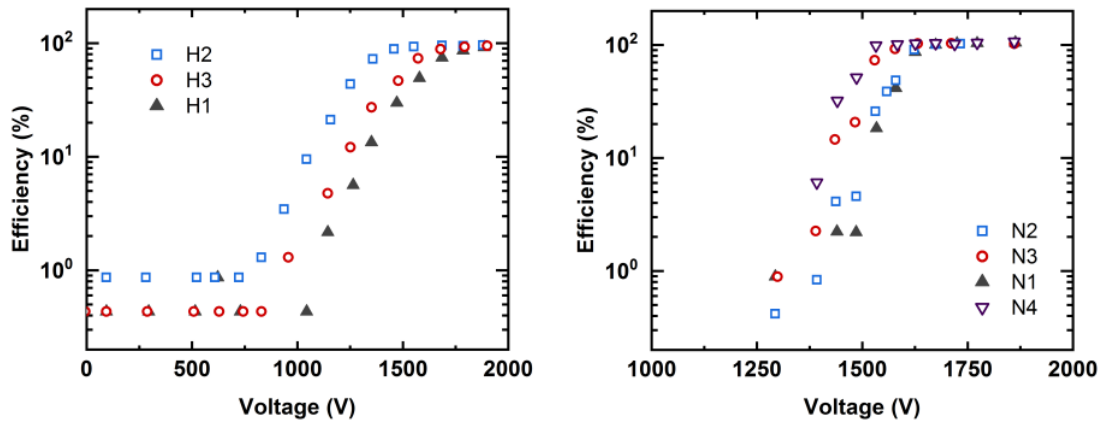


FIGURE 2.3: The voltage versus efficiency plot of 3 hut paddles (H1,H2,H3) in the *left* figure and same plot for all four trigger paddles (N1,N2,N3,N4) in the *right* figure.

Trigger Paddles

4 PSs, of the same make as hut paddles, but with smaller dimensions of 440 mm (width) \times 440 mm (length) \times 10 mm (thickness) were stacked one top of another to make the muon trigger setup. When a muon passes through all the PSs a trigger was generated by logical AND of all the scintillators. Due to the space constraint inside the hut, another set of smaller PS of dimension 150 mm (width) \times 200 mm

(length) \times 10 mm (thickness) were also used for the trigger generation. Light collection was done by light guide in this case. The PMTs used were same as in the hut paddles and has been described earlier. Both types of trigger paddles are shown in Fig. 2.4.

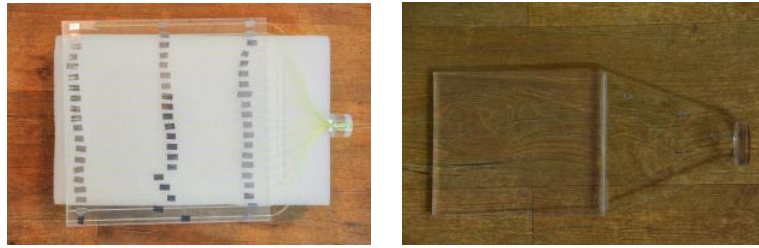


FIGURE 2.4: Picture of PS, before wrapping for MuL (*Left*) and MuS (*Right*).

All configurations of CMV

Four configurations of CMV was studied to optimize the veto efficiency. The trigger paddles are named as N_1 , N_2 , N_3 and N_4 with N_1 being the topmost PS and all hut paddles are named as H_1 - H_{14} . The description of all the configurations of hut and trigger scintillators is given in Table 2.2 and the schematic is shown in Fig. 2.6.

In the first configuration, 44 cm \times 44 cm (MuL i.e., Muon Large setup) PS, stacked one top of another were used as trigger paddles. A schematic of this configuration is shown in Fig. 2.5. A layer of 30 mm lead was placed in between N_2 and N_3 . This was done to reduce γ - γ coincidences which could be misinterpreted as a muon trigger and could be mistaken as the inefficiency of the veto. In this configuration, two layers of hut “inner” and “outer” were assembled with outer top layer placed perpendicular to the inner top layer as shown in Fig. 2.6a. As can be seen from the schematic (Fig. 2.5), the total area available inside the CMV hut was 92 cm \times 92 cm and the trigger set up was placed near one

corner. As a result the paddles near the trigger set up would participate more than the ones in the opposite corner.

In order to place the trigger set up more centrally, smaller paddles $15\text{ cm} \times 20\text{ cm}$ (MuS i.e., Muon Small setup), were used in the second configuration. A 30 mm thick layer of lead was kept in between N_2 and N_3 as shown in Fig. 2.6d.

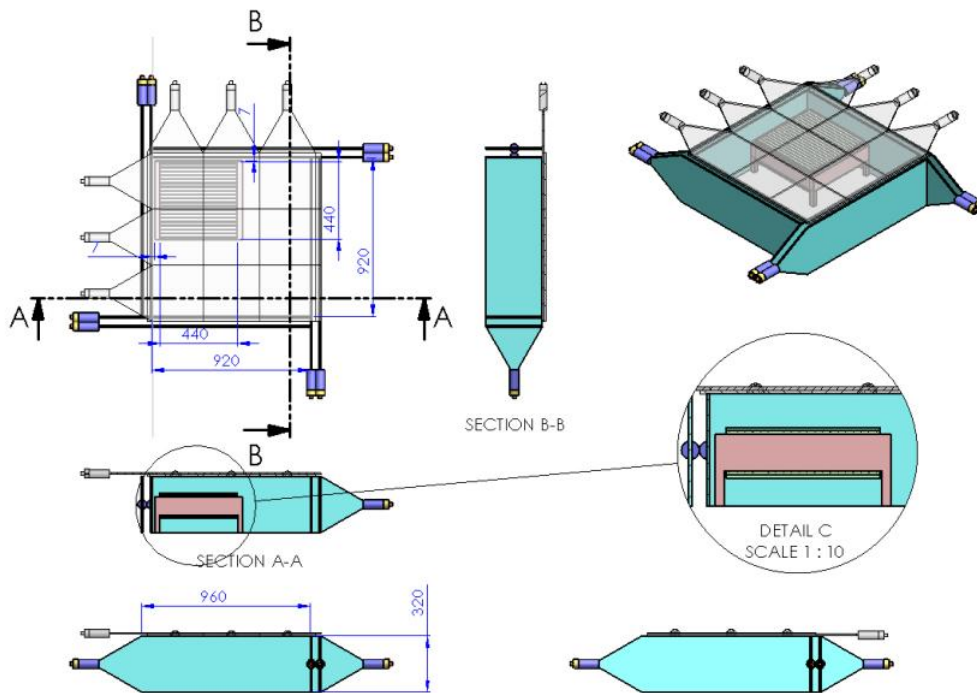


FIGURE 2.5: Drawing of MuL set-up

For studying the inefficiency of the CMV detector, with the MuS trigger detector, a third layer was added on top of the upper two layers. Three side paddles (H11, H12, H13) from the outer hut were used for this purpose as shown in Fig. 2.6b. The third layer of paddles on top was placed parallel to, and with an offset of 20 mm, from the 2nd layer of paddles so as to cover the gaps between the adjoining scintillators.

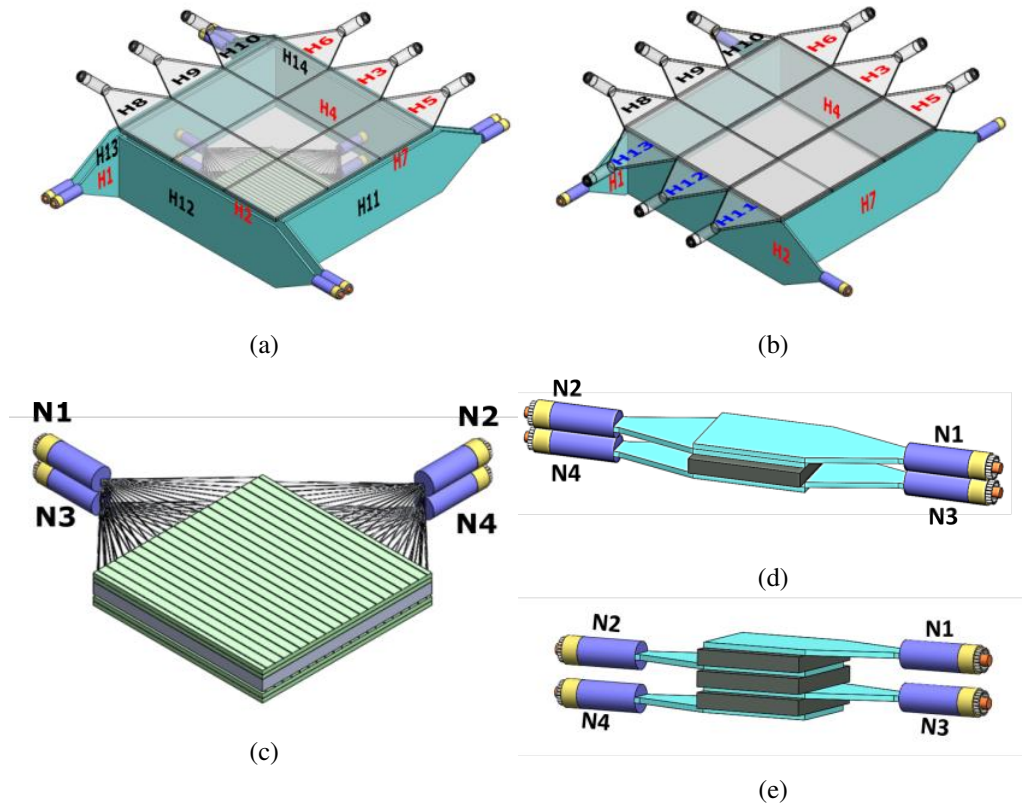


FIGURE 2.6: 3D model of trigger detector configurations and CMV hut. (a) CMV shield with 2 layers of scintillators on 4 walls and top with inner hut paddles (H1-H7) labeled in red and outer hut paddles (H8-H14) in black (b) CMV shield with 3 layers of scintillators on the top, with topmost layer paddles (H11,H12,H13) labeled in blue, middle layer paddles (H8,H9,H10) in black and bottom layer paddles (H3,H5,H6) in red and 1 layer of scintillators on the 4 walls labeled in red (c) MuL (d) MuS (e) MuS along with 3 Pb layers.

The triggers which are caused by γ -ray can be reduced by placing high Z material in between the gaps in the trigger set up. For this purpose, a layer of lead was kept in one of the gap. Furthermore, the coincidences triggered by γ -ray can be reduced by populating all the three gaps with same lead layers.

In the Configuration IV, lead layers were placed in between consecutive scintillators of MuS trigger detector and assembled as shown in Fig. 2.6e.



FIGURE 2.7: Photographs of the MuL (left) and MuS (right) trigger detectors inside the CMV detector with the top layers removed.

TABLE 2.2: Description of all detector configurations.

Configuration	No. of scintillator layers on the top in CMV detector	No. of scintillator layers at the sides in CMV detector	Trigger detector	No. of Pb layers	Figure No.
I	2	2	MuL	1	1(a,c)
II	2	2	MuS	1	1(a,d)
III	3	1	MuS	1	1(b,d)
IV	3	1	MuS	3	1(b,e)

2.2 Data Acquisition

A CAMAC based DAQ was used to acquire timing and latch information of all the paddles in the CMV. The analog signals from the trigger paddles were fanned out into two by using a 1×16 FIFO by Phillips Scientific model no. 740. One of the outputs was fed to the QDC which was used to integrate the total charge in a pulse of fixed time window. The other outputs were fed to a 8 channel

discriminator by Phillips Scientific, model no. 705 and then to a logic unit for generating a 4-fold coincidence trigger. In one of the PS (N1) fast logic signal was made narrow (~ 10 ns width) and delayed by about 20 ns while the other 3 had a width of about 50 ns before it is fed to the trigger generating 4-fold coincidence unit. This reduces the contribution of jitter due to N2, N3 and N4 to the timing data. An example showing the 4 signals is shown in Fig. 2.8. The muon trigger rate was ~ 15 Hz for MuL configuration and ~ 2 Hz for Mus (with one layer of lead). This trigger is shaped to a 130 ns pulse and connected as GATE input to the QDC. Three trigger paddles with GATE window is shown in Fig. 2.9. The logic signals of all the hut PSs were combined to make different OR signals as shown in Fig. 2.10 and their corresponding rates are mentioned in Table 2.3. The OR of 14 scintillators was then digitally ANDed with the muon trigger to form a 5-fold coincidence which was used for efficiency calculations. Fast signals from each of the scintillators were also fed to 2 TDCs for measuring the relative times with respect to the trigger. The time window was set to be 100 ns.

TABLE 2.3: Various OR rates.

Description	Rates (Hz)
Inner Wall	2350
Inner Top	540
Inner Hut	2830
Outer Wall	3450
Outer Top	2500
Outer Hut	5900

The time resolution was measured to be ~ 1 ns for trigger scintillators in the MuS configuration and ~ 2 ns for top hut scintillators. Typical time spectra are shown in Fig. 2.14. The photon transport within the scintillator results in a spread

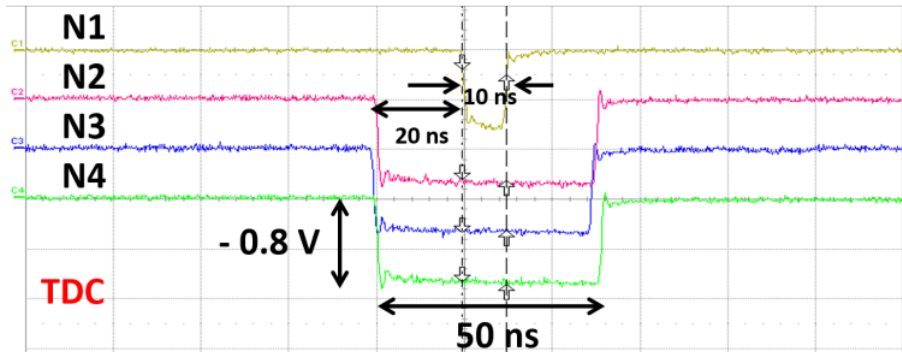


FIGURE 2.8: Screen shot of CRO showing the discriminated pulses of all the trigger paddles used to form trigger.

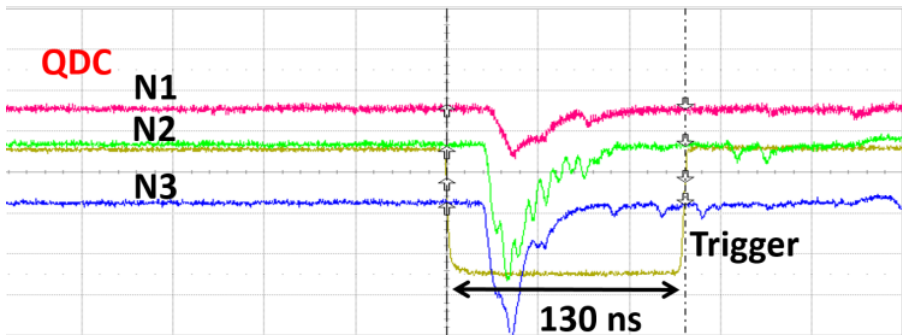


FIGURE 2.9: Screen shot of CRO showing three of the trigger paddles and the QDC gate window.

in timing. The hut scintillators are bigger in size than the trigger scintillators due to which the path-length transversed by the photon to reach the PMT is more. This results in a larger time resolution for the hut scintillators.

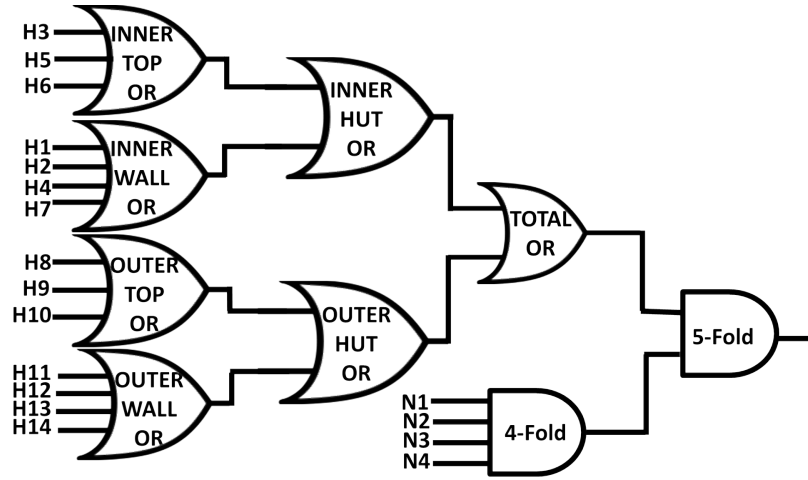


FIGURE 2.10: Logic diagram for 5-fold and 4-fold coincidence circuits.

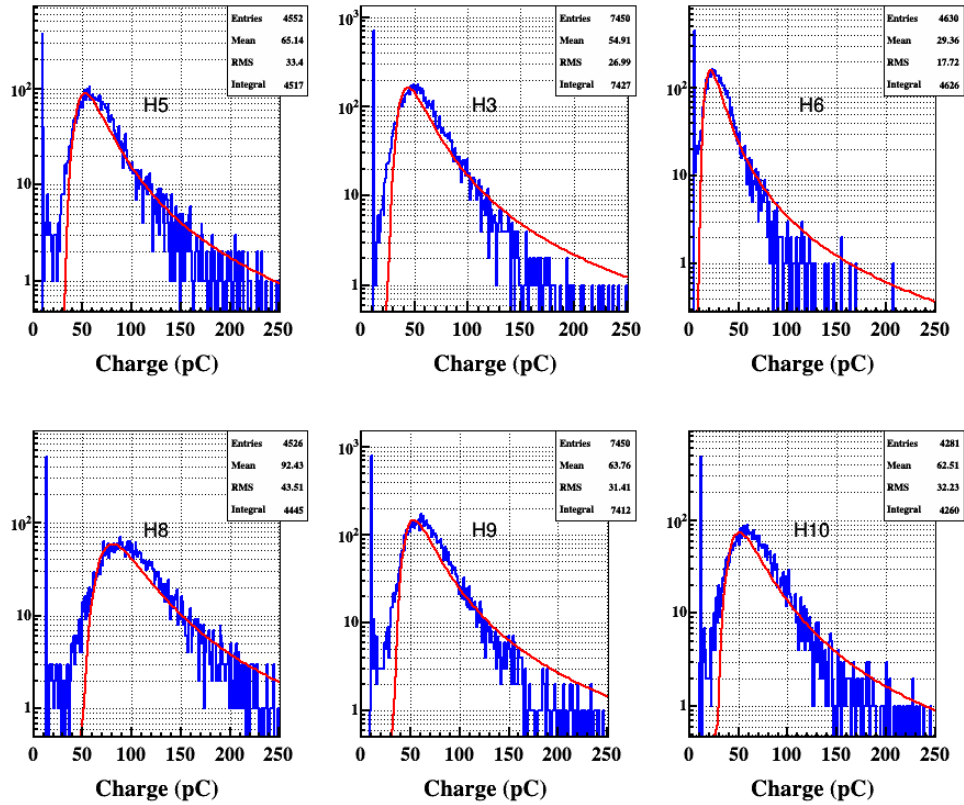


FIGURE 2.11: QDC spectra of hut paddles.

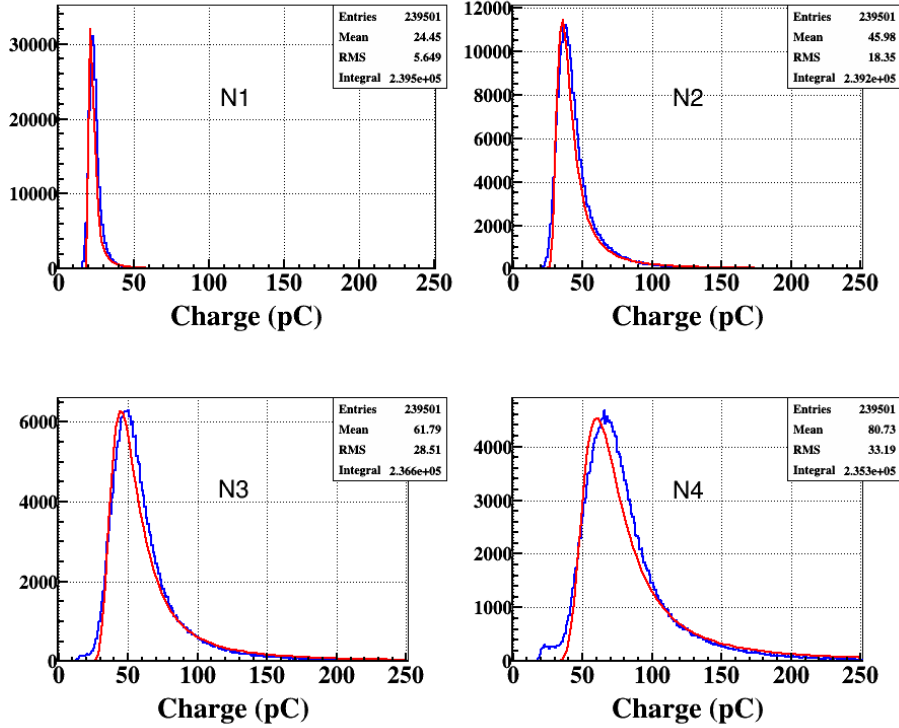


FIGURE 2.12: QDC spectra of MuL trigger scintillators.

2.3 Results and discussion

2.3.1 Cosmic Muon Rejection Efficiency

The efficiency for the rejection of cosmic muons from the ratio of the 5-fold to 4-fold coincidences was calculated after analyzing the event-by-event TDC data in a CAMAC based data acquisition system. Table 2.4 show the veto efficiencies for individual huts, inner and outer, as well as for the combined huts (ORed) for configurations I and II. The TDC was operated at a full scale range of 100 ns.

The analysis of the event-by-event TDC data gives an overall veto efficiency of $(99.880 \pm 0.007)\%$ for the configuration I. The inner and outer huts have

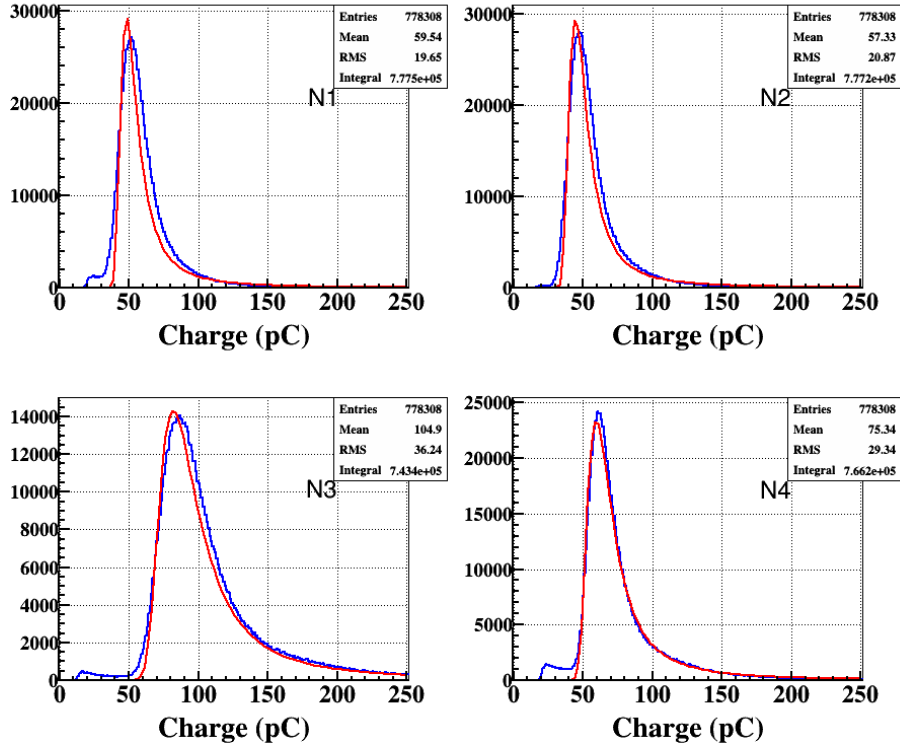


FIGURE 2.13: QDC spectra of MuS trigger scintillators.

individual efficiencies of $(99.420 \pm 0.015)\%$ and $(99.354 \pm 0.016)\%$, respectively. As might be expected from the geometry, the side detectors contribute a smaller, but important, veto efficiency with the nearer two sides contributing more than the farther two. The configuration II data gives an overall veto efficiency of $(99.847 \pm 0.005)\%$ with the inner and outer hut efficiencies being $(99.680 \pm 0.007)\%$ and $(99.652 \pm 0.007)\%$, respectively. It must be mentioned that the 4-fold coincidence in the muon trigger detector is assumed to arise from cosmic muons. If a small fraction of these is due to high energy neutral particle cascades generated in the topmost muon trigger detector or the lowermost part of the top veto detector, they may not generate a signal in the CMV hut and could

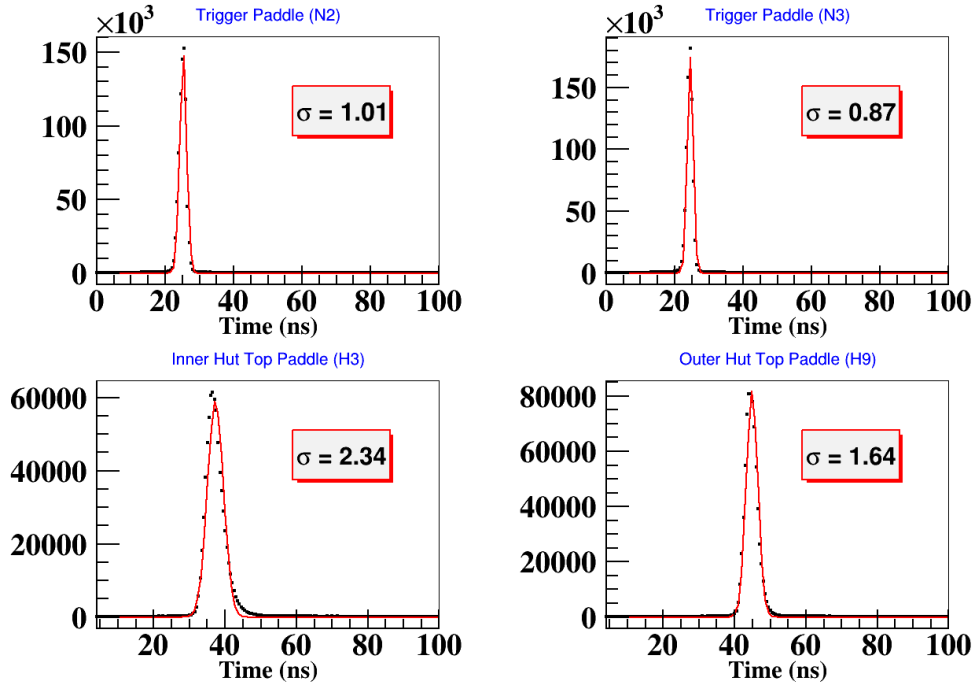


FIGURE 2.14: TDC Spectra of trigger and CMV hut scintillators.

TABLE 2.4: CMV efficiencies for individual parts of the detector at -20 mV threshold for configuration I and II.

Veto configuration	Veto efficiency (%) (Configuration I)	Veto efficiency (%) (Configuration II)
Only Inner hut top	91.347 ± 0.057	94.944 ± 0.026
Only Inner hut side	1.111 ± 0.021	0.085 ± 0.003
Inner hut top and side	6.972 ± 0.052	4.670 ± 0.025
Inner hut all	99.420 ± 0.015	99.680 ± 0.007
Only Outer hut top	93.026 ± 0.052	95.652 ± 0.024
Only Outer hut side	1.344 ± 0.023	0.099 ± 0.004
Outer hut top and side	4.632 ± 0.043	3.935 ± 0.023
Outer hut all	99.354 ± 0.016	99.652 ± 0.007
Inner + Outer huts	99.880 ± 0.007	99.847 ± 0.005

masquerade as a contribution to the inefficiency. The TDC information of each paddle was analyzed to extract the 5-fold contributions due to different parts of the CMV detector. In configuration II of the detector assembly, geometrically no

muon trajectory is possible which can generate a 5-fold due to contribution (a) only from the side scintillators or (b) from both side and top scintillators. But 0.1% of the total 5-folds were observed due to (a) and 4.5% due to (b). This could be a result of simultaneous arrival of many secondary or tertiary particles of cosmic showers.

For configuration III, a set of measurements was performed by varying the thresholds of the MuS trigger paddles from -20 mV to -150 mV to emphasize muons and reduce the electromagnetic shower contribution. The results from these runs are shown in Table 2.5. An increased threshold results in increase in veto efficiency from $(99.823 \pm 0.012)\%$ to $(99.922 \pm 0.010)\%$. A larger threshold reduces the chance of trigger generation inside the hut due to low energy particles which may not give a hit in the CMV hut paddles resulting in inefficiency. This also reduces the rate of random coincidence of MuS trigger.

TABLE 2.5: Veto efficiencies for different thresholds of configuration III.

Threshold (mV)	Veto efficiency (%)
-20	99.823 ± 0.012
-50	99.887 ± 0.011
-80	99.880 ± 0.011
-100	99.922 ± 0.010
-120	99.890 ± 0.014
-150	99.888 ± 0.013

2.3.2 γ -ray induced mis-identification rate

The effect of lead plates between successive layers of the PSs constituting the muon trigger MuS on the CMV detector efficiency was studied. With no lead in MuS for configuration III, the veto efficiency dropped to $(99.16 \pm 0.01)\%$. This

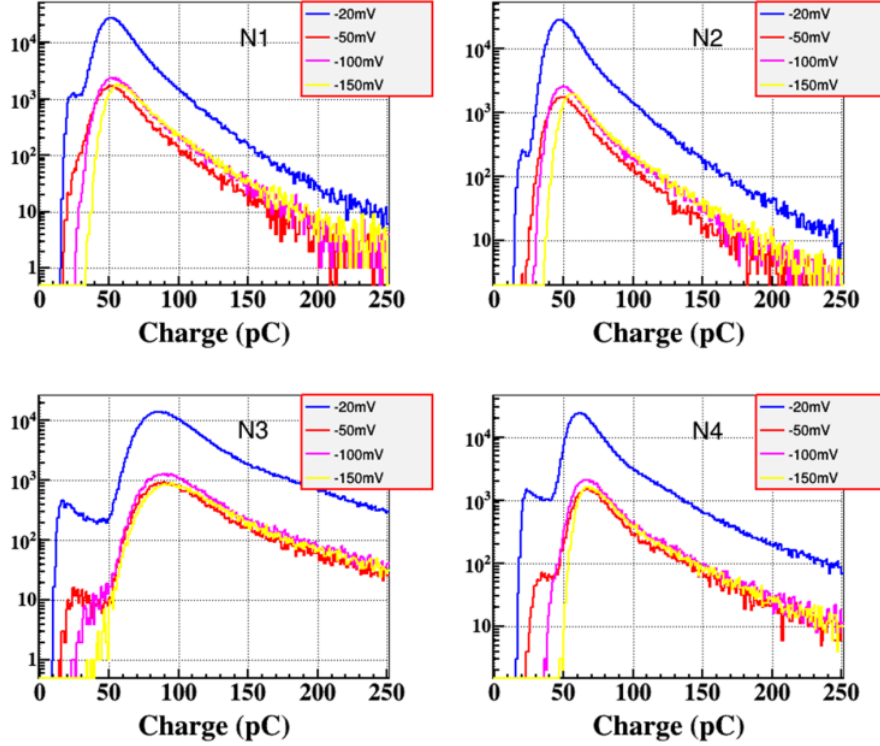


FIGURE 2.15: QDC spectra of MuL trigger scintillators with different thresholds.

is significantly smaller than the efficiency with one layer of lead in configuration II, as seen from Table 2.4 strongly suggesting that γ -ray induced events are being misidentified as muons leading to a lower CMV efficiency. To test this hypothesis, configuration IV with three layers of lead were placed in between successive PSs of MuS, as shown in Fig. 2.6e, was studied. The results are summarized in the Table 2.6.

The Veto efficiency was calculated in two ways:

1. Selecting events only from a prompt time window of 100 ns in the TDC data
2. Selecting events in different time windows starting from 40 ns to 80 ns in

TABLE 2.6: Veto efficiencies of configuration IV at -100 mV threshold for the trigger detectors.

Description	Veto efficiency(%) (with 100 ns prompt gate)	Veto efficiency(%) (from fit)
Top Layer	99.749 ± 0.006	99.52 ± 0.010
Middle layer	99.951 ± 0.002	99.920 ± 0.005
Bottom Layer	99.933 ± 0.003	99.908 ± 0.006
Top or middle Layers	99.970 ± 0.002	99.964 ± 0.004
Top or bottom Layer	99.973 ± 0.002	99.969 ± 0.004
Middle or bottom Layer	99.979 ± 0.002	99.975 ± 0.003
Any one Layer	99.981 ± 0.002	99.978 ± 0.003

steps of 10 ns.

These efficiencies were then plotted as a function of time window and fitted to a polynomial of order one. This was done in order to remove the contribution of chance coincidence to the efficiency calculations. The veto efficiency is the value where the fitted line cuts the y-axis i.e., the intercept of the curve. The typical plot is shown in Fig. 2.16 for the configuration where all three layers are used for the veto. The maximum veto efficiency of $(99.978 \pm 0.003)\%$ was achieved in this configuration. Since the CMV detector was assembled from old plastic scintillators that were available in our laboratory, the measured 99.98% veto efficiency is very encouraging. A better designed detector, such as the Mu2e CRV detector [32], could possibly give a much better efficiency.

2.3.3 Other sources of inefficiencies in CMV

The intrinsic efficiency scan of all the hut paddles was performed by using a stack of 12 layer Resistive Plate Chambers (RPC) at Tata Institute of Fundamental Research at Mumbai. The RPCs are of dimensions $\sim 1 \text{ m} \times 1 \text{ m}$ operated with

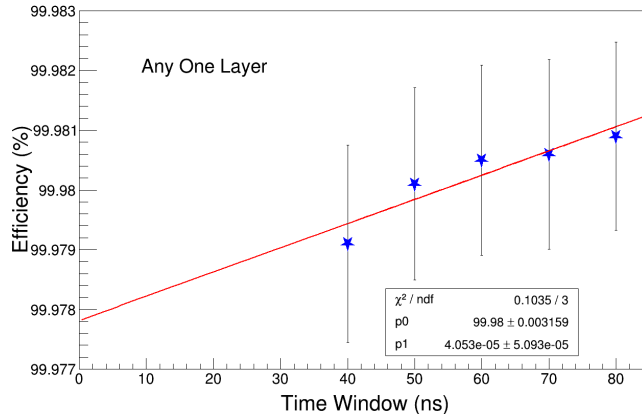


FIGURE 2.16: Veto Efficiency as a function of time window.

a gas mixture of Freon, Iso-butane and SF₆ in avalanche mode. Each RPC has 32 strips of width 28 mm and pitch of 30 mm for both X and Y sides. The stack is operational for the last 10 years and is used to characterize various detector and electronics components. The details of the RPC stack can be found in [38]. The basic purpose of the stack is to track cosmic ray muons by recording the position and timing information. Depending upon the measurement to be carried out respective hardware trigger can be set in the stack. The stack was used to investigate the source of inefficiency of the CMV paddles. For doing that we had placed three PSs side by side covering an area of 92 cm × 92 cm on top of layer 5 (as shown in Fig. 2.17) (where layer 0 corresponds to the bottom most RPC layer). The trigger was formed by an AND of signals from layers 4, 5, 6 and 7 which ensures that the passing muon encounters PS (under test) also along its path. The trigger rate was measured to be ~50 Hz. Hence, the efficiency for a 320 mm × 320 mm pixel can be measured to about 0.17% accuracy in a day. In principle the zones for checking the efficiency can be made as small as 30 mm × 30 mm but in that case we have to acquire data for longer durations. The hit

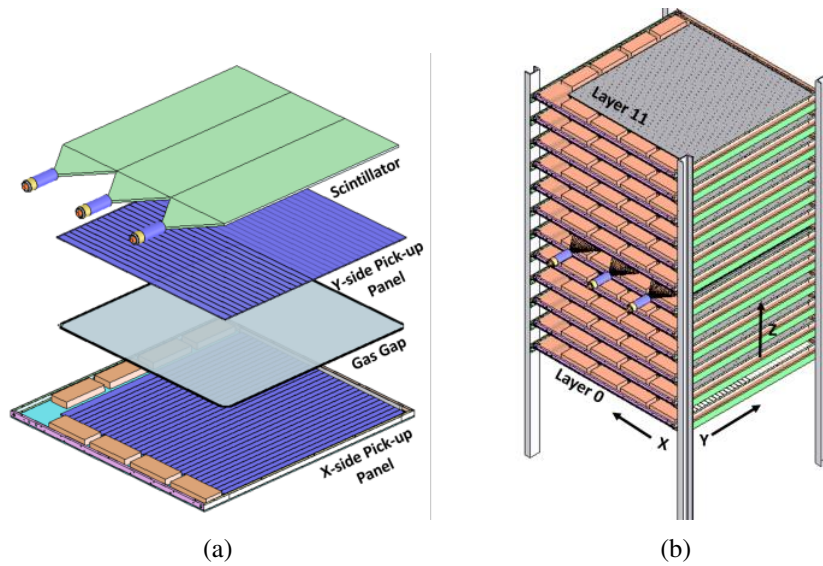


FIGURE 2.17: (a) Exploded view showing placement of 3 scintillators on top of 5th layer RPC with pick-up panels shown in blue color and gas gap in grey color, (b) the positioning of scintillators in the RPC stack.

information for PS was latched along with the hit information of the RPCs in the Data Acquisition system of RPC stack [39] for every event. The timing data was recorded in a separate commercially made multi-hit CAEN TDC (model no. V1190A [40]) having 32 channels. The signals from the paddles were connected to 3 channels of the TDC. And trigger from the RPC stack was used as trigger to the TDC. The total dead time of the RPC stack is ~ 5 ms and the time window kept in the TDC was $21 \mu\text{s}$. The efficiency map of all the PS is shown in Fig. 2.18. It can be seen from the figure that H6 paddle is less efficient in comparison to all others. However as it was placed at top side corner of the “inner” hut which was not directly on top of the trigger set-up in configuration I that is why it didn’t contribute in overall inefficiency. But in the configuration II the veto efficiency decreased as the trigger set-up was kept at the center which increased the participation of paddle H6. The efficiency scan of the paddles was done after

studying I and II configurations. For the subsequent runs we replaced the PMT of H6 paddle which increased the efficiency as shown in Fig. 2.18.

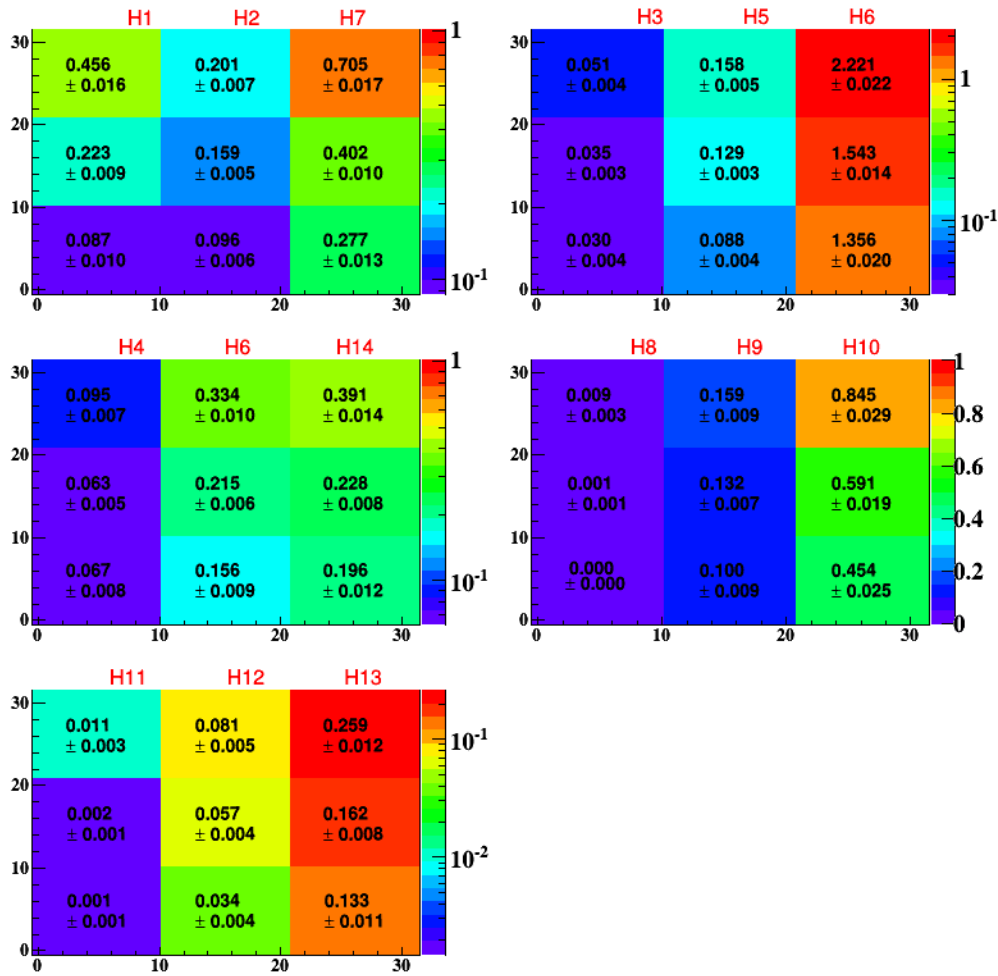


FIGURE 2.18: The inefficiency map of all hut scintillators. H6 was most inefficient (top-most right). Middle-left shows the inefficiency map of H6 after replacing the PMT.

2.4 Proof of principle demonstration in mini-ICAL

A bigger CMV is planned for the currently operational magnet prototype of ICAL named as mini-ICAL at IICHEP, Madurai. As the mini-ICAL detector, with 10 layers of RPC, has a magnet of dimensions $\sim 4 \text{ m} \times 4 \text{ m} \times 1.6 \text{ m}$ the CMV of dimensions $\sim 5 \text{ m} \times 5 \text{ m} \times 2 \text{ m}$ is needed. As each layer will be populated with 2 RPCs of dimensions $\sim 2 \text{ m} \times 2 \text{ m}$ the muon trigger rate is expected to be about 500 Hz leading to about 4.3×10^7 triggers/day. A CMV detector with an inefficiency of 10^{-6} for cosmic muons could be measured to an accuracy of 10 % within a couple of days while the corresponding figure for 10^{-4} would be about 1.6% in a day. The muon identification would be clean due to the tracking in the RPC detectors.

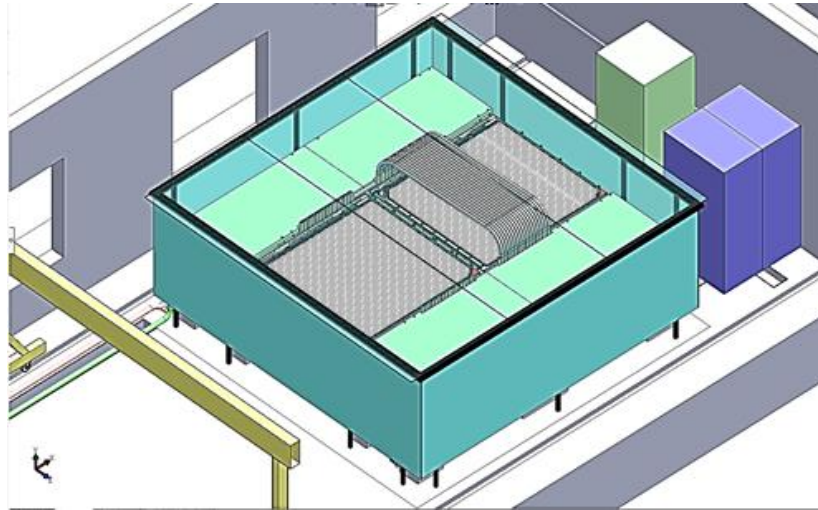


FIGURE 2.19: Schematic view of mini-ICAL from top along with veto detector.

2.5 Summary

In summary, the results of an experiment to measure the efficiency of a cosmic muon veto detector of about $\sim 1 \text{ m} \times 1 \text{ m} \times 0.3 \text{ m}$ dimensions are reported with the aim to assess the feasibility of building a larger version for a shallow depth ICAL detector. Efficiency maps of the plastic detectors used in the veto detector using a RPC stack for cosmic muons are also reported. The measured veto efficiency of $(99.978 \pm 0.003)\%$ with 3 layers of plastic at the top appears to be sufficiently encouraging as to justify building a larger "proof-of-principle" veto detector covering the mini-ICAL detector which will measure cosmic muons. Its success will determine whether or not one can build the much larger ICAL detector for atmospheric neutrinos at a shallow depth.

Muon induced neutral background for SICAL

The muons are highly penetrating particles as they don't interact much while passing through matter. Since they are about 200 times heavier than electrons, their energy loss in matter, upto energies of about 100 GeV, is predominantly through ionization leading to a large stopping length. This leads to muons being the only surviving primary cosmic ray particle at depths greater than about 10 m with the highest energy muons penetrating 1 km of rock and beyond. This makes the muon an important source of background in experiments searching for rare decays or events. The muon, being a charged particle, is easy to detect and can be vetoed as discussed in previous chapter. A secondary source of background is due to muon-nucleus interaction, mainly through deep inelastic scattering with nuclei. In this case one or more hadrons are produced. These could be a serious concern for many low background experiments. One such case is the SICAL detector where the neutrals can be produced as a result of interaction of muon

with the rock surrounding the cavern. While the charged particle(s) can be vetoed in the veto detector, the neutrals can simply escape detection in veto detector and go on to produce false positive signals in ICAL. The SICAL is a worthwhile proposition if the number of such false positives are reduced to a level that is significantly lower than the true positives (i.e. genuine neutrino events). It may not, therefore, be out of place to mention some of possible advantages of the SICAL detector viz.

- (1) a much larger choice of sites,
- (2) much larger caverns,
- (3) monitoring of RPCs using the much larger muon flux at 100 m depth as compared to that at 1 km depth,
- (4) if shown to be feasible, using muon spin rotation to get additional information on the internal magnetic field [41] and
- (5) enhancing the sensitivity for exotic searches including probing the origin of the anomalous KGF events [42] and cosmogenic magnetic monopoles [43] using the CMVD and the ICAL.

3.1 Simulation Framework

The Monte Carlo simulation was performed for two cases using GEANT4[7] simulation toolkit which is a C++ based software package equipped with various high energy physics and nuclear physics models, particle interactions, ability of tracking particles as they pass through matter and inclusion of complex detector geometries. The idea of the current simulation was to propagate the muons, which follow cosmic muon energy spectrum, in the 103 m of rock to find out the

distribution of the particles which survive and come out of the rock. The contribution of these particles in producing background events for the ICAL detector was studied. The energy (E), theta (θ) and phi (ϕ) distribution of cosmic ray muons was generated by CORSIKA [8] software using SIBYLL[9] model. The cosmic muon energy spectrum peaks at ~ 3 GeV but propagating the low energy muons throughout the rock volume of 100 m along with muon nuclear interactions lead to an undesirably high computational time. The hadrons produced in the upper part of the rock can not survive the remaining rock thickness. Therefore, in both the simulations the geometry was broken down into three blocks (A,B,C) as shown in Fig. 3.1. In block A, muons were propagated through 100 m of rock with only taking into account electromagnetic interactions in picture. As the hadronic interaction length is ~ 36 cm [44] this implies that the particles produced in only the last 36 cm or so of rock will be able to come out. This guided the thickness of block B as 3 m. Finally, the neutrals were propagated through ICAL detector which is referred as block C in Fig. 3.1. A GEANT4-based ICAL code was developed by INO collaboration and was being used for various physics studies. The same code was used during the course of this work. However, to incorporate rock, the geometry was modified depending upon the case under study.

In case I, a modular simulation was performed using a relatively simple geometry. The full geometry was broken down into 3 parts as shown in Fig. 3.1. The energy profile of the muon after traversing 100 m of rock from block A was given as input to the block B. And lastly, the neutrals coming out of the 3 m of rock with their respective energy and theta distributions, obtained from the simulation, were provided as input to block C representing ICAL. In this part, only vertically

downward going muons were considered. In case II, a more realistic geometry

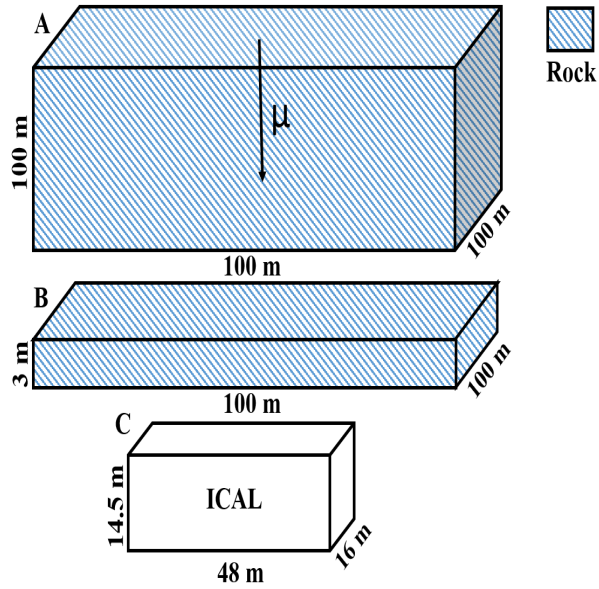


FIGURE 3.1: Schematic showing the geometry and placement of the blocks of rock and ICAL detector used in simulation.

was considered in this part which included an additional veto detector made up of plastic scintillator. The total overburden of rock was considered to be 103 m and the cosmic muon veto detector (CMVD) was placed against the inner walls of the cavern as shown in Fig. 3.2. Here the 3D muon flux (E, θ, ϕ) of was used in order to incorporate all possible angles of cosmic ray muons.

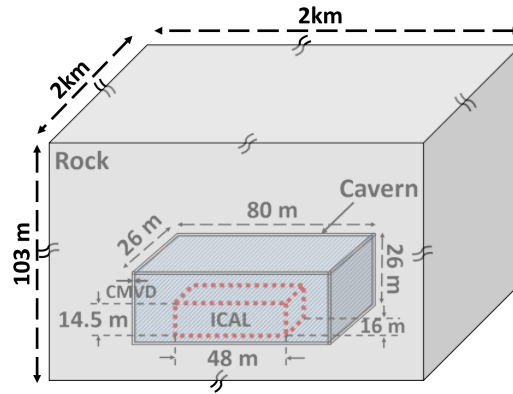


FIGURE 3.2: A schematic of the SICAL detector at a depth of 103 m along with the CMVD

3.2 Case I : Simplistic Geometry and Vertical muons

The dimensions of volume A were chosen to be $100\text{ m} \times 100\text{ m} \times 100\text{ m}$. The muons were propagated from the center of the top surface of volume A. The momentum direction was vertically downwards as shown in Fig. 3.1. The initial energy of muon E_μ , was generated uniformly ranging from 0.01 to 500 GeV. The energy of muon E_μ' , after traversing 100 m of rock was stored in a ROOT format. A 2D histogram between the initial energy (E_μ) and shifted energy (E_μ') is shown in Fig. 3.3. The entire range of E_μ' was divided into bins of width 1 GeV. The data in each bin was drawn in a separate histogram. And each histogram was fitted to a Crystal Ball [45] fit function. Two such histograms are shown in Fig. 3.3 for $E_\mu = 80\text{ GeV}$ and 300 GeV . Furthermore, in second set of simulation considering the muon-nuclear interaction in 3 m of rock the muons with shifted energy spectra were propagated in block B of rock. The dimensions of block B were $100\text{ m} \times 100\text{ m} \times 3\text{ m}$. The energy of muon was selected by CORSIKA flux

however for a given energy the shifted energy was chosen by taking a random energy from the Crystal Ball fit function for the corresponding energy histogram. This respectively shifts the energy of muon in correspondence to 100 m of rock. As it can be seen from the Fig. 3.4 the primary cosmic muon energy spectrum generated from CORSIKA at position A is in red, muon energy spectrum at position B i.e., after traversing 100 m of rock is in blue and the shifted muon energy spectrum is in pink. There is a sharp cut off at $E = 50$ GeV that signifies the minimum energy required by muon to traverse 100 m of rock material.

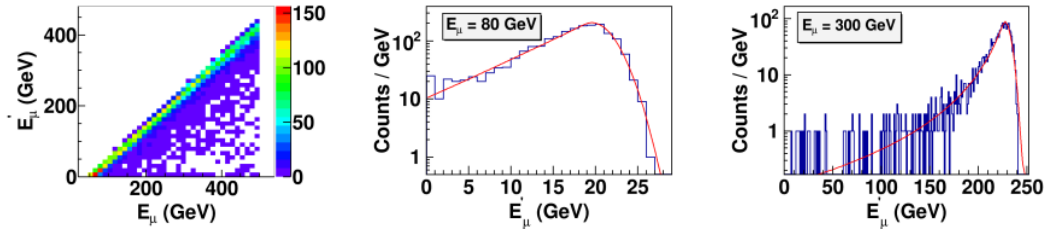


FIGURE 3.3: Two-dimensional plot of incident muon energy E_μ and muon energy after 100 m rock E'_μ (left) and E'_μ distribution for 80 GeV (center) and 300 GeV (right) incident muon energy fitted to Crystal Ball fit function.

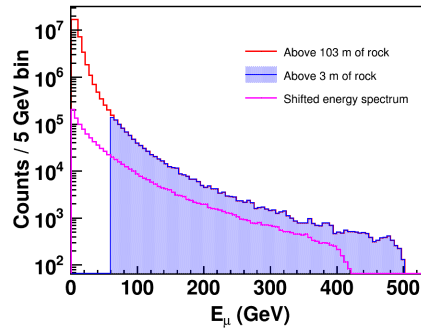


FIGURE 3.4: Cosmic muon energy spectra at different position as explained in the text.

The Kokoulin model [46] was used to simulate muon-nuclear interactions in the rock. The hadronic interactions of the secondaries were also considered. In the simulation, the primary muon, along with all the secondaries in the hadronic

cascade were propagated to the bottom of the block B shown in Fig. 3.1 and the associated information, like E , θ , ϕ , (x,y,z) positions at the end of the 3 m rock, about the particles were stored. The secondaries produced in muon-nuclear interactions with their fractions are listed in Table 3.1.

TABLE 3.1: Fraction of neutral secondaries produced in muon nuclear interaction.

Particles	Fraction (%)
n	93.8
π^0	4.9
K_L^0	0.65
Σ^0	0.21
η^0	0.16
η^1	0.05
λ^0	0.04
Σ^-	0.03
Σ^+	0.03
ρ^0	0.02
Ξ^0	0.001
Ξ^-	0.001

It should be noted that particles such as the neutron, K_L^0 and π^0 are produced in larger numbers in muon-nuclear interaction of muon with rock. It is therefore important to study their interactions with matter and particles produced in their decay.

- Although a neutron cannot produce a muon through its decay, it can interact with the Fe in the ICAL and produce charged pions and kaons which can decay and produce muons.
- The K_L^0 has a decay mode leading to muons and kaons with a branching ratio of 27 % which makes it important for the present study.

- The π^0 s produced are not of major concern as they have a very short lifetime ($\sim 10^{-16}$ sec) and decay into 2 γ -rays. Each γ -ray leads to an electromagnetic shower in the ICAL which can be very well distinguished out from clean muon trajectories.

So that leaves the neutron and K_L^0 as possible sources of backgrounds for SICAL. Typical energy and θ distributions of neutrons and K_L^0 s from this simulation are shown in Fig. 3.5.

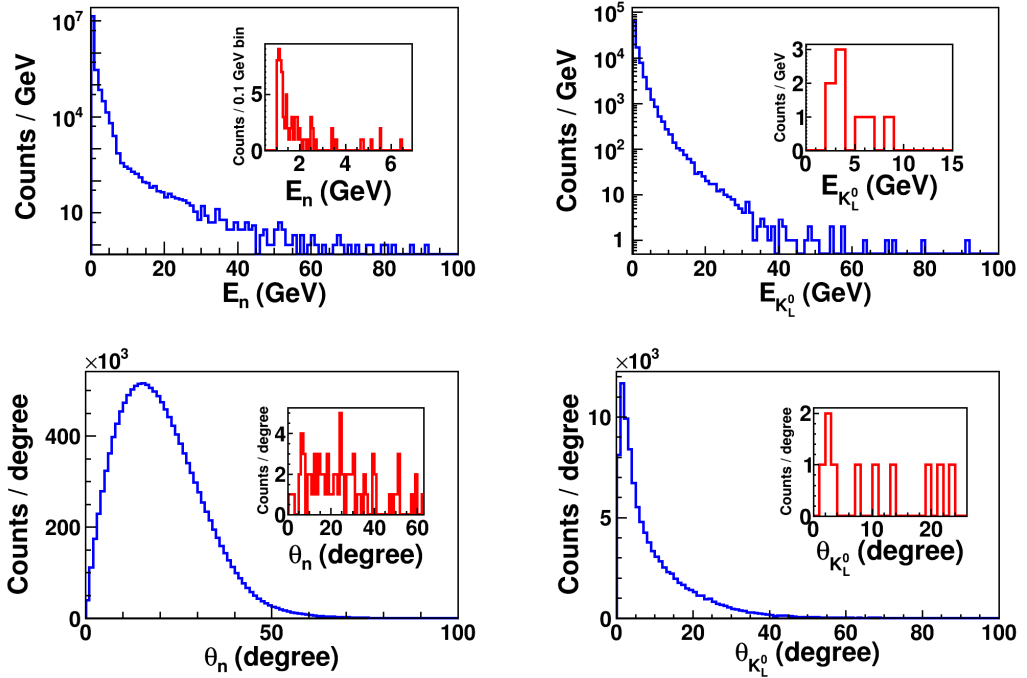


FIGURE 3.5: Energy and theta spectra of neutrons (left top and left bottom) and K_L^0 s (right top and right bottom). Blue histogram shows the total neutrons (or K_L^0 s) coming out of rock and red histogram shows neutrons (or K_L^0 s) coming out without any accompanying charged particle.

An estimate of the number of muon-nucleus events in 3m of rock was made. If muon-nuclear interaction cross section is $\sigma_{\mu N}$, the number of particle interaction

events N_{ev} for N_{inc} incident particles is given by

$$N_{ev} = \frac{\sigma_{\mu N} \cdot N_{inc} \cdot \rho \cdot \lambda \cdot N_A}{A} \quad (3.1)$$

If we consider the case where the muon-nucleus interaction cross-section $\sigma_{\mu N} = 1$ mb (from GEANT4), the density of standard rock (SiO_2) $\rho = 2.65$ gm-cm⁻³, the molecular weight $A = 60$ amu and the hadronic interaction length λ in $\text{SiO}_2 = 36$ cm, with N_A as Avogadro's number, the number of interactions in a hadronic interaction length is estimated to be :

$$\frac{N_{ev}}{N_{inc}} \sim 3 \times 10^{-3} \quad (3.2)$$

In the simulation, for a total of 10^{10} incident muons, there are $\sim 4.5 \times 10^7$ muon nuclear interactions which give $\frac{N_{ev}}{N_{inc}} = 4.5 \times 10^{-3}$ which corresponds well with the above estimation. The total secondaries produced were about 3.0×10^8 out of which 1.3×10^7 come out of the rock and the number of events in which no charged particle is present is about a hundred. The number of two most populous and relevant long lived neutrals, i.e. neutrons and K_L^0 coming out of the rock with and without any associated charged particles is tabulated in Table 3.2. Out of a total of $\sim 6.8 \times 10^6$ events, in roughly 8 % of them, neutrons and K_L^0 s having an energy more than 1 GeV, come out of the rock. The number of events with neutrals unaccompanied by any charged particle that are relevant for this study should satisfy the following conditions :

- (a) the charged particle coming out of the rock along with the neutral particle should have energy more than 50 MeV, as below this energy the charged particle may not give any signal in the veto detector,
- (b) the neutral particle should have energy greater than 1 GeV which is required

to produce a charged particle in nuclear interaction, which can pass through five layers of RPC detector in ICAL to mimic a muon in a ν_μ charged current interaction.

Table 3.2 describes the events (or particles) distribution of neutrons and K_L^0 for 10^{10} muons incident on the last 3 m of rock. N denotes the total number of events (or particles) produced, N_{out} denotes number of events (or particles) coming out of the rock and N'_{out} denotes the number of events (or particles) coming out of the rock with out any accompanying charged particle.

	<i>neutron</i>		K_L^0	
	No. of Events	No. of Particles	No. of Events	No. of Particles
N (all E)	29378181	83254316	273864	316862
N_{out} (all E)	6670889	12579456	80852	87059
N_{out} (E > 1 GeV)	485790	511498	46770	49475
N'_{out} (E > 1 GeV)	111	111	10	11

TABLE 3.2: Events (or particles) distribution of neutrons and K_L^0 for 10^{10} muons incident on the last 3 m of rock.

3.2.1 False positive event rate in ICAL due to muon-induced neutrals

Any event that is generated as a result of interaction of particles different from a neutrino but is very likely to be classified as a neutrino induced event in the ICAL detector is called a false positive. All the secondaries resulting from the muon-nuclear interactions, as listed in Table 3.1, were propagated in the ICAL simulation code [47] with their respective (E, θ) distributions taken from previous simulation (as shown in Fig. 3.5). The incident particle was chosen in accordance

with the fraction by which it was produced. A trajectory of a charged particle due to false positive signal is considered to be track-like if it satisfies two criterion :

- 1) The fitted track should have hits in minimum 5 layers of ICAL detector and
- 2) $\chi^2/ndf < 10$ of the fitted track.

After performing the simulation for certain number of events, the fraction in which a track-like signal F_{trk} was obtained is

$$F_{trk} = 2 \times 10^{-3} \quad (3.3)$$

Due to almost 100% efficiency of the veto detector, a large fraction of all the secondaries coming out of the rock would be vetoed. However, due to the small inefficiency, the rest will traverse the veto detector undetected. From an earlier measurement with a small Cosmic Muon Veto detector [36] the veto efficiency achieved was 99.987% which is equivalent to a reduction in muon flux, resulting in reducing false positive events, by about 10^4 . So, the number of secondaries coming out of rock which could lead to false positive events will also effectively reduce by a factor of 10^4 . The fraction of false positives due to neutrals in ICAL is given as,

$$F_{FP} = N_{out} \times F_{trk} \times (\epsilon_{veto})^{n_q} \quad (3.4)$$

where n_q is the number of charged particles coming out of the rock along with at least one neutral particle, N_{out} ($E > 1$ GeV) is the number of events in which neutron or K_L^0 comes out of the rock with $E > 1$ GeV and ϵ_{veto} is the veto inefficiency. While the probability of not detecting only one charged particle is more than the probability of not detecting at least one out of two, for the sake of completeness the event-wise break-up is done for estimating the F_{FP} . Table

3.4 shows the distribution of events with different number of charged and neutral particles coming out of rock.

TABLE 3.3: Break up of events with a specified number of charged particles (q) and neutral particles (n) for 10^{10} muons interacting with the last 3 m rock just above ICAL

Configuration	N_{out} (E > 1 GeV)	F_{FP}
0 q & 1 n	120	2.4×10^{-1}
0 q & 2 n	1	2×10^{-3}
0 q & 3 n	0	0
1 q & 1 n	119381	2.3×10^{-2}
1 q & 2 n	0	0
1 q & 3 n	0	0
2 q & 1 n	70430	1.4×10^{-6}
2 q & 2 n	4636	9.3×10^{-8}
2 q & 3 n	0	0
Others	329818	0
Total	524386	2×10^{-1}

- The total number of incident muons in the simulation at 100 m depth was 10^8 .
- The cross section was multiplied by a factor of 100 so effective number of simulated muons after 100 m of rock becomes 10^{10} .
- As the surface flux reduces after traversing 100 m rock by a factor of ~ 100 , the effective number of muons at surface will be 10^{12} .
- From Eq. 3.4, the fractional false positive signal rate comes out to be 0.2×10^{-12} .
- The primary cosmic ray muon flux at sea level is $70 \text{ m}^{-2} \text{ sec}^{-1} \text{ sr}^{-1}$ from [44]. The dimensions of each module of ICAL are $16 \text{ m} \times 16 \text{ m} \times 14.5 \text{ m}$

and there will be three such modules resulting in a total surface area of $48\text{ m} \times 16\text{ m}$. For an overground ICAL the muon event rate will be $\sim 10^{10}/\text{day}$.

- The false positive rate becomes

$$0.2 \times 10^{-12} \times 10^{10}/\text{day} = 0.002/\text{day} \quad (3.5)$$

3.2.2 Neutrino event rate for ICAL detector

If $\sigma_{CC} = 10^{-38}\text{ cm}^2$ [44] is the ν_{μ} and $\bar{\nu}_{\mu}$ inclusive scattering cross section (per nucleon), $\rho = 7.8\text{ gm-cm}^{-3}$ is the density of iron (Fe) then from Eq. 2.1 the $\frac{N_{ev}}{N_{inc}} \sim 4 \times 10^{-14}$ for 150 layers of iron in ICAL. The primary cosmic neutrino flux from [48] is $10^3\text{ m}^{-2}\text{ sec}^{-1}\text{ sr}^{-1}$ which gives the neutrino event rate for ICAL to be $\sim 3/\text{day}$. The neutrino event rate at INO-ICAL using a Monte Carlo simulation is reported by A. Kumar *et al.* [5], where the ICAL geometry and Honda flux [48] were used as inputs in the NUANCE [49] event generator. As it can be seen from Fig. 3.6, the total number of events simulated for 10 years of exposure is 14642, with 10217 events for μ^{-} and 4425 events for μ^{+} . Therefore, the neutrino event rate is estimated to be $\sim 4/\text{day}$. This simulation matches within 25% with the above estimate.

The signal to false positive for SICAL is therefore, about 1000 which makes SICAL a feasible proposition. The primary muon background is much larger at 100 m depth as compared to that at 1 km and will be identified and removed in the same way as in the original plan of ICAL detector with about 1 km rock over-burden by using the algorithm to detect events in fiducial volume of ICAL detector.

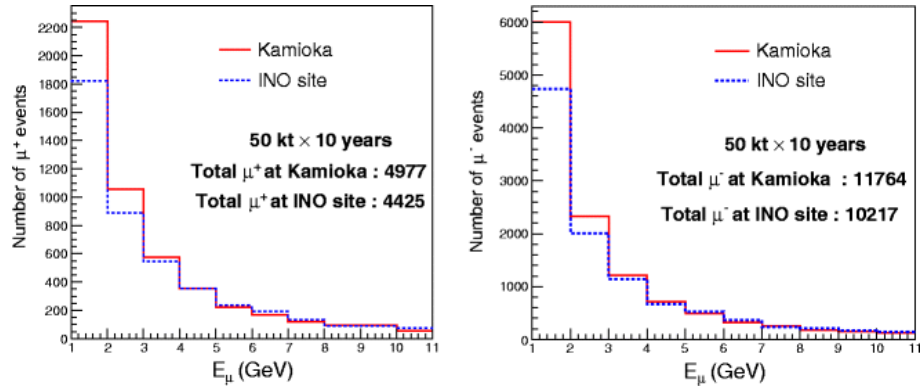


FIGURE 3.6: Event rate estimation for ICAL detector taken from Ref. [5]

3.3 Case II : Cavern Hugging Configuration of CMVD

A more realistic simulation was performed and is discussed in the section. In this case a full geometry was constructed in GEANT4 as shown in Fig. 3.2. The major blocks of the geometry along-with their dimensions are listed below :-

- 1) Rock of density $\rho = 2.23$ gm/cc and dimensions $2 \text{ km} \times 2 \text{ km} \times 103 \text{ m}$ (thickness),
- 2) Cavern of dimensions $(80 \text{ m} \times 26 \text{ m} \times 26 \text{ m})$,
- 3) CMVD made up of 3 cm thick plastic scintillator material, placed up against the walls and the ceiling of cavern,
- 4) ICAL detector of dimensions $(48 \text{ m} \times 16 \text{ m} \times 14.5 \text{ m})$ with 151 layers of iron along with 150 layers of RPCs placed inside the gaps between iron layers.

In this part also, in order to save the computational time the rock overburden was studied by dividing into two parts. In the first part, a simple cuboid of rock was considered with dimensions $2 \text{ km} \times 2 \text{ km} \times 100 \text{ m}$. At sea level (N_0) muons with the (x,y) positions generated uniformly over the surface area of 2 km

$\times 2$ km were simulated. For these N_0 muons the 3D flux (E, θ, ϕ) was generated from CORSIKA software by using SIBYLL model. The choice of the surface area was governed by the fact that the plane should be large enough to consider all possible angles of cosmic muons that could potentially lead to false positive events in ICAL. The cosmic muon zenith angle spectrum (CMZAS) ranges from 180° (vertically down muon) to 90° (horizontal muon). Ideally, an infinite plane is required to consider all possible angles. In the simulation, we have taken $2 \text{ km} \times 2 \text{ km}$ surface area of the 100 m rock which covers angles from 180° to 95° of CMZAS. Therefore, we want to emphasize that 95% of all the possible angles are selected in the simulation. But the flux is almost negligible for angles less than 95° hence with the chosen surface area, 99.9% of the CMZAS is covered. Furthermore, a small volume 'V' as shown in Fig. 3.7 was constructed. Only if the muon direction chosen randomly from 3D flux intersected with any of the two planes of volume 'V' then the muon was propagated in GEANT4. This led to a reduction of 6×10^2 in N_0 as depending upon the angle many of the muons are not in the direction pointing towards ICAL. All such muons will have no muon-nuclear interaction in rock which can cause false positive signals in the ICAL detector. As the muon propagates through rock it may also undergo multiple scattering which can ultimately lead to changing the direction of muon. Due to this reason the dimension of the volume 'V' was substantially doubled than the size of CMVD in all the directions. Another important factor of reduction in N_0 is due to the low energy muons and the secondaries produced by them. As we know that muon is a minimum ionizing particle (MIP) which implies that muon would deposit 46 GeV in passing through the 100 m of rock following the formula for stopping power $\frac{1}{\rho} \frac{dE}{dx} \sim 2 \text{ MeVg}^{-1} \text{cm}^2$. Therefore, to propagate the muon, E_μ

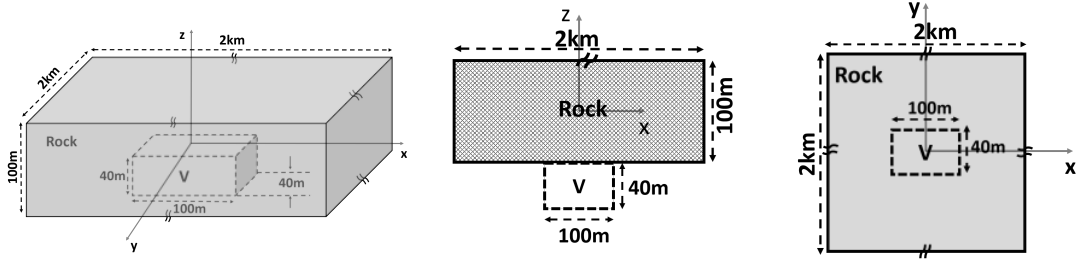


FIGURE 3.7: A schematic representation for the geometry used for the first part of the simulation. 3D cartoon picture (*left*), 2D side view (*center*) and top view (*right*).

> 46 GeV is required. However muons traversing matter at larger angles (θ) will move $100 \times \cos\theta$ m in rock. Only if $E > \frac{E_{th}}{\cos\theta}$, the muon were selected for further propagation. This reduced N_0 by another factor of 1.2×10^2 . So considering both the factor :-

- 1) solid angle coverage and
- 2) reduction in muon flux due to energy loss of muon.

$$N_1 = 7.2 \times 10^4 \times N_0 \quad (3.6)$$

Also, it was observed in the simulation that with $E_{th} = 46$ GeV the fraction of muon coming out is 65% because for high energy muons there are losses other than ionization energy loss whereas for $E_{th} = 48$ GeV, 82% of muons were coming out of rock. We have used $E_{th} = 48$ GeV in this simulation. Due to energy threshold the N_1 reduces to N_2 .

$$N_2 = 0.82 \times N_1 \quad (3.7)$$

The muon-nuclear interaction is not important in this part of the simulation, hence, it was excluded in the physics list of GEANT4. The (x,y) position at the

rock surface for N_0 , N_1 and N_2 is shown in Fig. 3.8 and the corresponding E , θ and ϕ distribution is shown in Fig. 3.9 for a subset of the data.

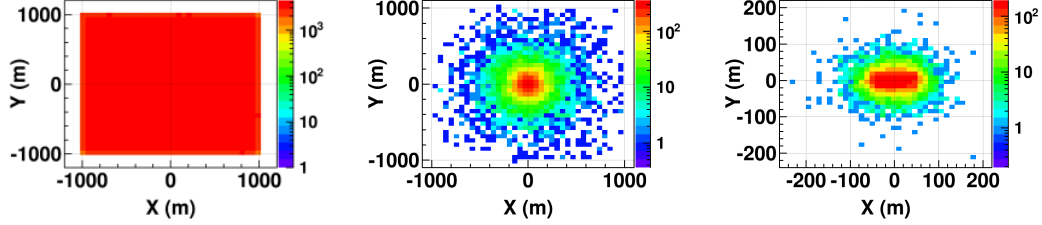


FIGURE 3.8: The position distribution, (x,y) of events at the rock surface for N_0 (left), N_1 (center) and N_2 (right).

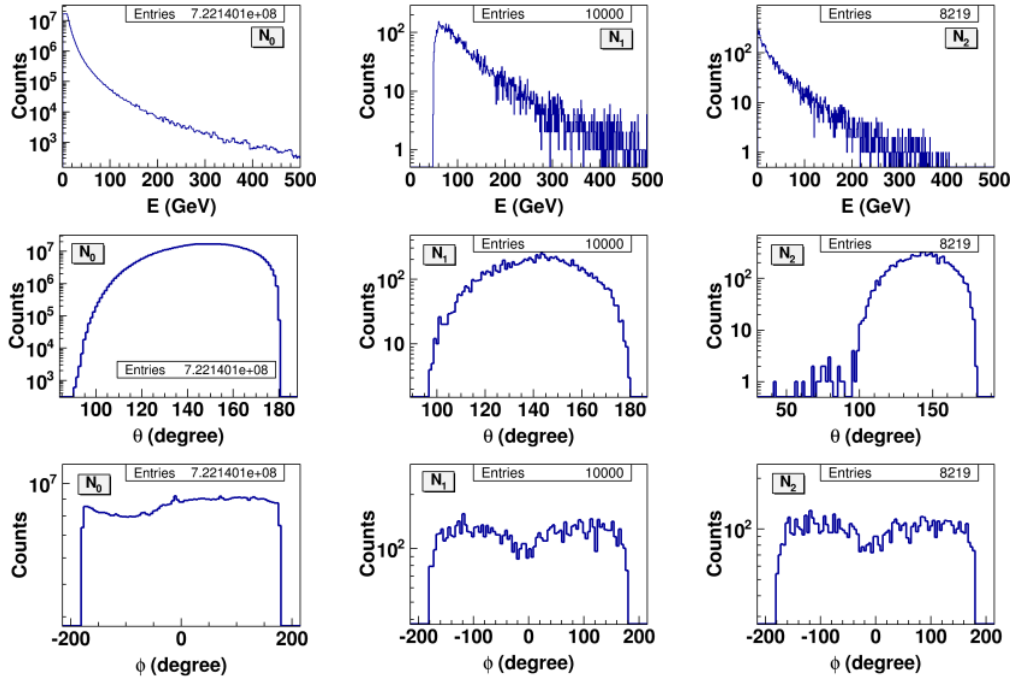


FIGURE 3.9: E (top), θ (center) and ϕ (bottom) distribution for N_0 (left), N_1 (center) and N_2 (right) for event selections N_0 , N_1 , N_2 as described in the text.

The detector geometry used for the second part of the simulation is shown in Fig. 3.10. In this part, the muon-induced neutral background for the SICAL detector is studied. For this, $N_2(7.38 \times 10^8)$ muons with E , θ and ϕ distribution

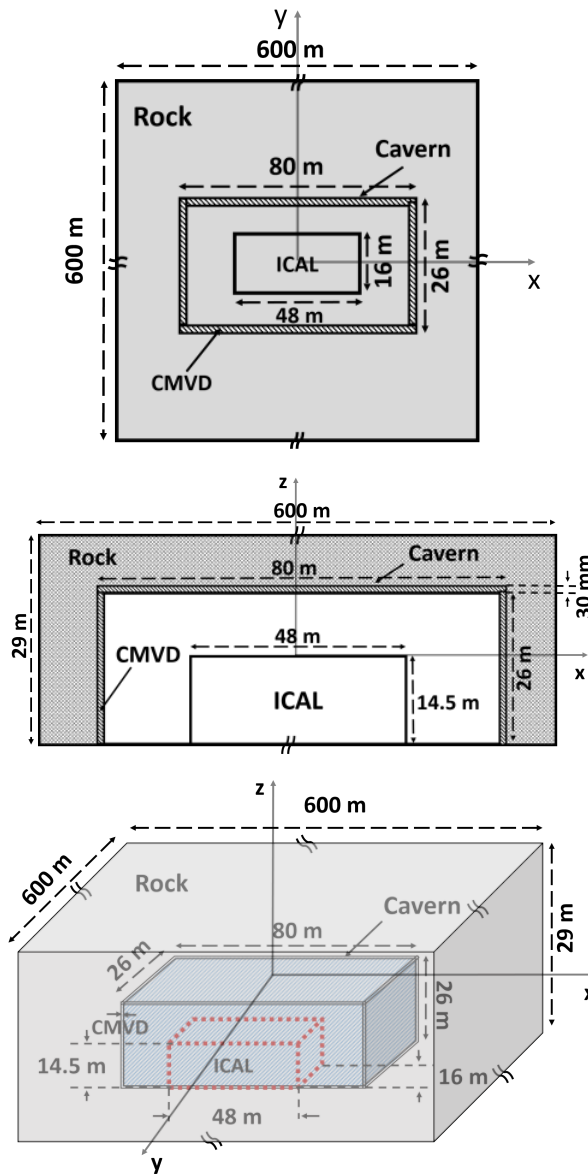


FIGURE 3.10: A schematic representation for the detector geometry used in the second part of the simulation.

as shown in Fig. 3.9 (*bottom*) are propagated from the top surface of the 3 m rock having the same (x,y) coordinates as shown in Fig. 3.8 (*right*) obtained from the first part. It is legitimate to consider that the neutrals produced in muon-nuclear

interactions, mostly from the last part of the 3 m depth of rock, could exit the rock. The choice of 3 m was guided by the hadronic interaction length λ for rock which is 36 cm [44] i.e. ~ 10 times smaller. This was verified by performing the simulation for 5 m and 10 m of rock which produced, within error, the same number of outgoing neutral particles as with 3 m rock. Following this argument, only $N_3(3.69 \times 10^8)$ muons out of N_2 , that are expected to pass through rock material of 3 m surrounding the cavern, are allowed to propagate. The cross-section for the muon nuclear interaction was increased by a factor 100 to reduce the computation time. The hadronic interactions of the secondaries are also considered. All the particles (both neutral and charged) that are coming out of the rock and entering through the cavern are recorded in the scintillator of the CMVD. As the muon-nuclear cross-section is increased by a factor of 100, the charged particles (predominantly muons) will create extraneous interactions. Hence, they were not propagated beyond the CMVD once detected in the scintillator. In contrast, the neutrals were allowed to propagate through the cavern towards the ICAL detector.

3.4 Results and discussions

The total number of muon-nuclear interactions in the rock are found to be 5.58×10^8 and the vertices of these interactions are shown in Fig. 3.11. It can be seen that the number of interactions increases with the distance traversed by the muon in the rock as expected. The number of secondaries produced due to muon-nuclear interactions is 4.95×10^9 and out of this 2.7×10^9 could come out of the rock. As discussed in the previous section that the two most important

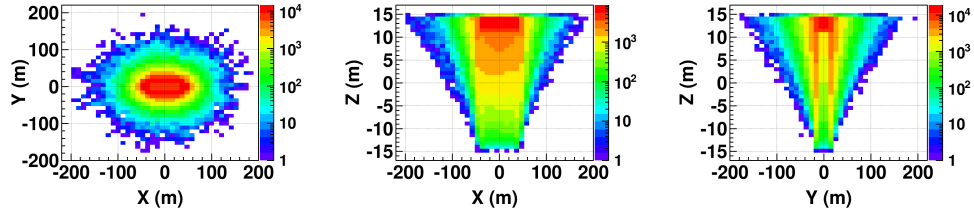
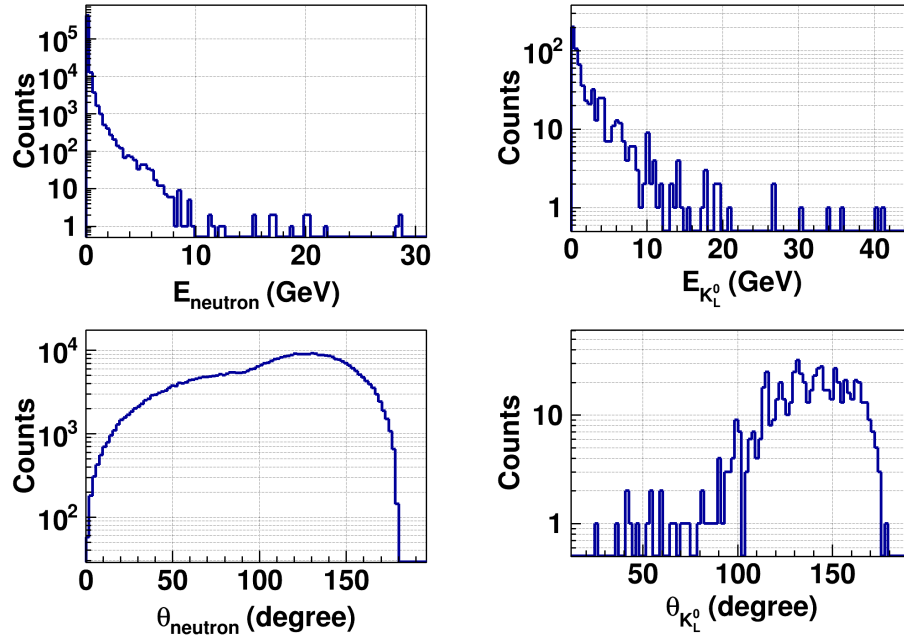


FIGURE 3.11: The vertices of all the muon-nuclear interaction in different views.

muon-induced neutral background are neutrons and K_L^0 . The total number of neutrons and K_L^0 that are produced due to muon-nuclear interaction were 1.08×10^9 & 4.23×10^6 , respectively. In this part also, the neutral particles having

FIGURE 3.12: Energy and theta spectra of neutrons (left top and left bottom) and K_L^0 s (right top and right bottom).

more than 1 GeV were counted as relevant ones. Only those events in which neutrals have energy > 1 GeV are considered for further estimation of muon-induced neutral background in the ICAL. Further, the number of such events which could lead to false positive events in ICAL were:-

- a) Events in which neutrals are accompanied by no charged particle
- b) Events in which neutrals are accompanied by charged particles having kinetic energy less than 10 MeV as below this energy the charged particle may not give any signal in the CMVD.

All these events were then reconstructed in the ICAL detector using the Kalman filter technique [50, 51]. The fiducial volume of the ICAL detector was also considered in this case and it was defined as volume excluding the region of the top 4 layers and 30 cm from all the four sides of the ICAL detector. The conditions on the track to be qualified as relevant one were:-

- 1) The fitted track should have hits in minimum 5 layers of ICAL detector,
- 2) $\chi^2/ndf < 10$ of the fitted track and
- 3) The should be well contained inside the fiducial volume of the ICAL detector.

Consequently, 2 out of 9×10^8 simulated events have resulted in false positive events. These are shown in Fig. 3.13 and the relevant parameters are listed in Table 3.4. This also provides an upper bound of 6.3 false positive events at ICAL with a confidence level [44] (C.L.) of 95%. In Fig. 3.13, the co-ordinates of ICAL in simulation geometry were (-24 m, 24 m) along X-axis, (-8 m, 8 m) along Y-axis and the Z-axis denotes the layer number. There were total 150 layers and the bottom most layer was numbered as zero. Due to almost 100% efficiency of the veto detector, a large fraction of all the primary muons coming out of the rock would be vetoed. From an earlier measurement with a small Cosmic Muon Veto detector [36] the veto efficiency achieved was 99.987% which is equivalent to a reduction in muon flux by about 10^4 . Nevertheless, due to the small inefficiency, a part of the total primary cosmic muons will leak through the veto detector undetected. It should be emphasized that, the number of such muons will be

comparable to the muon background level in the ICAL detector placed at a depth of 1 km. This residual primary muon background will be identified and removed in the same way as in the original plan of the ICAL detector with about 1 km rock over-burden by using the algorithm to detect events in the fiducial volume of the ICAL detector.

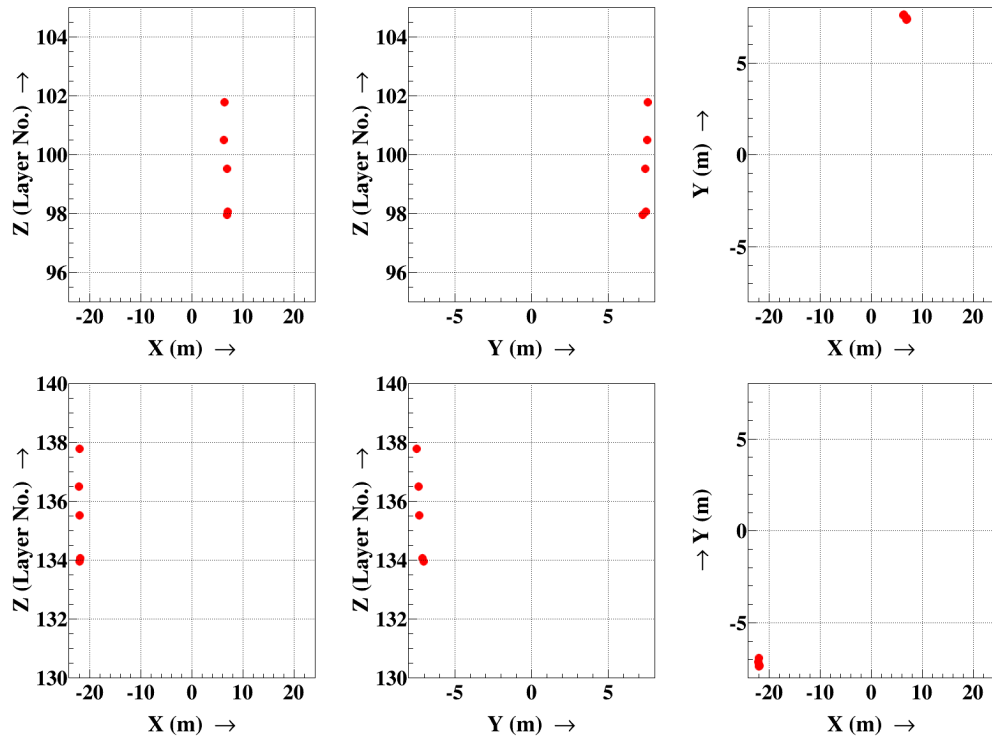


FIGURE 3.13: Reconstructed tracks of the two false positive events in the ICAL detector obtained from the simulation.

TABLE 3.4: Characteristics of the two events that are false positive signal at SICAL. V_x and V_y denotes the x and y position of the vertices of the reconstructed track.

No. of hits	χ^2/ndf	θ (rad)	ϕ (rad)	V_x (m)	V_y (m)	Layer No.
5	0.37	2.34	2.33	6.63	7.65	101
5	0.24	2.17	-1.44	-21.8	-7.48	137

3.5 Estimation of false positive event rate in the SICAL due to muon-induced neutrals.

- The total number of muons simulated in GEANT4 = 9×10^8
- Equivalent number of muons at the sea level = $9 \times 10^8 \times 120 \times 600 = 6.5 \times 10^{13}$
- As the muon nuclear cross section was enhanced by a factor of 100 therefore total no of muons at the sea level becomes 6.5×10^{15}
- The primary cosmic ray muon flux at the sea level is $70 \text{ m}^{-2} \text{ sec}^{-1} \text{ sr}^{-1}$ [44] that leads for an surface area $2 \text{ km} \times 2 \text{ km}$, about 4.8×10^{13} cosmic muons per day.
- The equivalent number of muons simulated (N) then corresponds to

$$N = \frac{6.5 \times 10^{13}}{4.8 \times 10^{13}} = 135 \text{ days} \quad (3.8)$$

- The false positive rate becomes

$$\frac{2 \text{ events}}{135 \text{ days}} = 0.015/\text{day} \quad (3.9)$$

with an upper bound of 0.05 /day at 95% confidence level.

The neutrino event rate at INO-ICAL is ~ 4 per day. The false positive to signal for the SICAL detector is therefore, about $\sim 0.4\%$ with an upper bound of $\sim 1.2\%$ at 95% C.L. which makes the SICAL a feasible proposition.

It may be relevant to examine an issue of false vetoes, discussed in the context in the IceCube [52], that may potentially affect the ICAL. The cosmic ray

interaction with the upper atmosphere leading to neutrinos is also associated with muons. However, the tracking capability of the ICAL detector in combination with the CMVD should be able to clearly identify the event due to muon neutrinos as opposed to the those originating from the upper atmosphere and giving a track at a physically different location.

While the energy and angle dependence of the muon spectrum is pretty robust there could be some leeway in the deep inelastic partial differential cross sections used in GEANT4. A more foolproof test of this idea would be to place a reasonable sized ICAL prototype detector at a shallow depth of ~ 30 m, enclose it in a CMVD and quantify the false positive which could mimic neutrino events in the ICAL, at the same time comparing with the simulations at that depth.

3.6 Summary

In summary, we have presented results of simulations which support the possibility of locating the INO-ICAL detector at a shallow location with a rock overburden of ~ 100 m when used with an efficient cosmic ray shield with an efficiency of about 99.99% for detecting charged particles. The main background is due to neutral, long lived and energetic particles produced in the last few metres of rock either unaccompanied by or associated with charged particles which go undetected. This fraction has been estimated to be much smaller ($\sim 0.4\%$ with an upper bound of $\sim 1.2\%$ at 95% C.L.) than the signal due to atmospheric neutrinos. Therefore, the proposal of a the SICAL detector opens up the possibility of having a much larger choice of locations, saving time due to the shorter tunnel and allowing for much larger caverns. However, it must be mentioned that it is

necessary that a proof-of-principle detector be built at an even shallower depth with about 30 m rock overburden, together with the Cosmic Veto Detector, to validate the simulation.

Commissioning of mini-ICAL detector

The mini-ICAL (m-ICAL) detector has been commissioned at the Inter Institutional Center of High Energy Physics (IICHEP), Madurai in Tamil Nadu. The dimensions of m-ICAL are $4\text{ m} \times 4\text{ m} \times 1.2\text{ m}$. The magnet assembly weighs 85 ton and comprises of 11 layers of 5.6 cm thick iron plates. Presently, there are 10 layers of active detectors (RPCs) placed centrally inside the gaps available between the iron layers to track muons. The full $4\text{ m} \times 2\text{ m}$ area of m-ICAL detector is planned to be populated by 10 more RPCs in the second phase of detector installation.

4.1 m-ICAL magnet

The main components of the m-ICAL magnet assembly are the soft iron plates, the copper coils in 2 parts (U- and C-), sense coils wound around chosen plates on layers 0, 5 and 10 and aluminium strips fixed on the iron plates to guide the



FIGURE 4.1: The mini-ICAL detector at IICHEP, Madurai.

RPC trays. The foundation of the m-ICAL magnet was made with a concrete base and pedestal arrangement which can withstand the weight of 85 ton. The dimensions of base were $4.6\text{ m} \times 4.6\text{ m} \times 0.2\text{ m}$. On top of which 12 concrete pedestals of different sizes were made as shown in Fig. 4.2. On top of every pedestal a sheet of stainless steel was placed. On top these pedestals the iron plates were arranged.

Placement of iron plates

The soft iron plates were desired to have high magnetic permeability, low percentage of carbon, good mechanical strength and reasonable cost. Iron plates were procured from the ESSAR steel plant at Hazira [53] with chemical, mechanical and magnetic properties listed in Table 4.1. Four different sizes of iron plates (A, B, C and D) were machined as shown in Fig. 4.3 (left picture). All four pieces were cut from a single iron plate (of dimensions $4.02\text{ m} \times 4.02\text{ m} \times 5.6\text{ cm}$). The plates were sand blasted and painted to protect them from corrosion. As shown in the schematic in Fig. 4.3 (right picture), two pieces each of three types and a

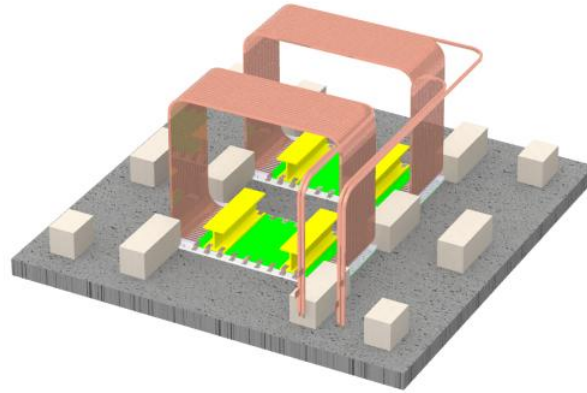


FIGURE 4.2: A schematic showing the concrete base (gray color) with 12 different sizes pedestals (white color) along with two copper coils.

single piece of the fourth type were used to were arranged to make a square of dimension $4\text{ m} \times 4\text{ m}$. Four different types of spacers, made up of non magnetic

TABLE 4.1: Chemical, mechanical and magnetic properties of soft iron plates procured from HISSAR company.

Parameter	Value
Material	Soft iron steel
Chemical composition	%C 0.015, %Mn 0.37, %P 0.012, %S 0.008, %Si 0.188, %Al 0.001, N 50ppm, 99.406% Fe)
Young's modulus	200 GPa
Density	7850 kg/m^3
Poisson's ratio	0.3
Yield strength	200 MPa (Min.)
Magnetic Property	Knee point 1.5 Tesla, H_{1T} 300 A/m, $H_{1.5T}$ 900 A/m

material, were used to maintain a gap of 45mm between two consecutive iron layers. All the spacers configurations are shown in Fig. 4.3. The spacers were placed and aligned exactly on top of the pedestals in order to transfer the load to the concrete pedestal. The plates were stuck together with locating pins of edge, intermediate and corner spacers with press fit arrangement. The locating pins were also made from stainless steel material. The role of middle spacers was to

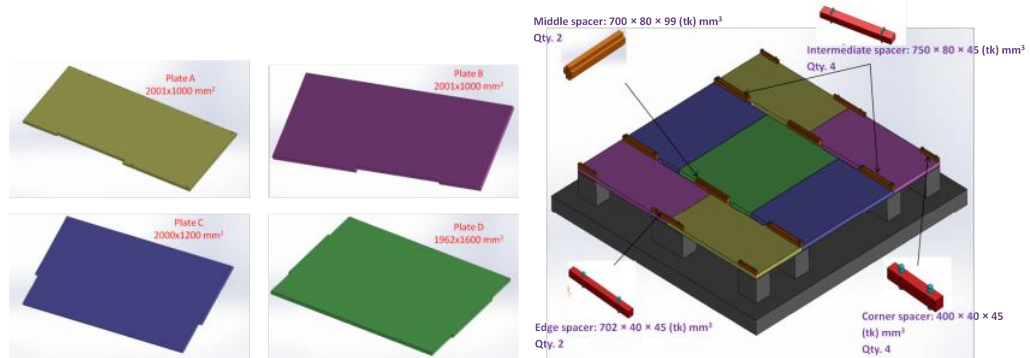


FIGURE 4.3: Schematic picture of four different sizes of iron plates used in m-ICAL (left) and placement of iron plates in a $4\text{ m} \times 4\text{ m}$ layer (right).

hold properly the middle iron plate and prevent it from sagging. The gap left in iron layer is for the passage of copper coils through it.

Copper Coils

The copper used for making the coils was 99.99% pure with a thermal conductivity of about $390\text{ Wm}^{-1}\text{K}^{-1}$. Two coils were placed symmetrically with 18 turns in each coil with a gap of 12 mm between each turn. The cross section of the copper conductor was $30\text{ mm} \times 30\text{ mm}$ with a bore diameter of 17 mm. The ball test method was used to examine the inner hole dimension of the coil after and during bending. The maximum current needed for a field of 1.5 Tesla was about 1000 A. Indeed this was also consistent with the rating of the DC power supply for the magnet. The coils were made in two sections 'U' and 'C'. The 'U' sections of the coil were mounted first on a G10 sheet. A G10 spacer was used to maintain equal spacing in between copper coils and insulate the coils from iron plates. While placing iron plates in each layer care had been taken to leave proper gaps for the passage of 'U' section of the coils through the gaps as shown

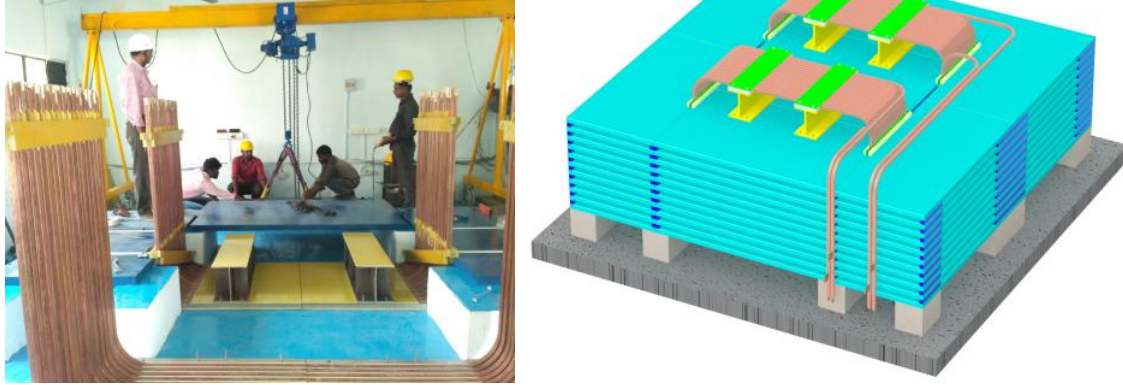


FIGURE 4.4: U section of the copper coil (left) and a schematic showing full coil after brazing both the section

in Fig 4.4 (left). The height of pedestal is 0.32 m and the bottom extension of the coil below the magnet bottom layer was kept to be 0.295 m whereas on the top, an extension was provided with 0.36 m high coil. This makes the total length of the coil to be $1.066 + 0.295 + 0.36 = 1.721$ m and the width was 2.002 m. After placing all the 11 layers of iron plates the 'C' sections of the coil were brazed along with 'U' sections of the coil on top to complete the copper loops as shown in the Fig 4.4 (right).

Magnet Power Supply

A 30V 1500A DC current supply (made by Danfysik) was used for powering the copper coils. The power supply is provided with both manual and computer control. A user friendly GUI was developed at VECC and Fig 4.5 shows a picture of the power supply and the control panel. A low conductivity water cooling system (LCWCS) was used for cooling the copper coils as well as the magnet power supply. The salient features of m-ICAL assembly are briefly described in Table 4.2.

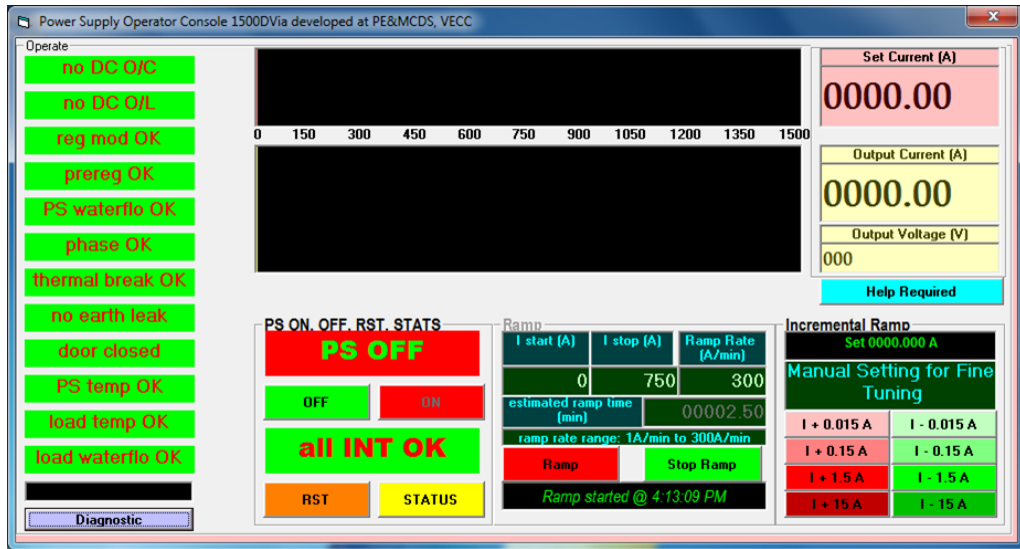


FIGURE 4.5: Screenshot of the operating control panel of the magnet power supply.

TABLE 4.2: The table summarizes all the components involved in the assembly of m-ICAL magnet assembly.

Parameter	Values
Magnet Size (only iron stack)	4 m x 4 m x 1.06 m
Weight	85 Ton
Magnetic field uniformity	F > 1T for 90% area
No. of Iron Layers	11 layers
Gap between two plate layers	45 mm
No. of copper coil / Turn in each coil	02/18
Induction (AT rating)	24,000 (Nominal)
Copper turn cross section (mm)	30 x 30 x ϕ 17 bore
Conductor material	Oxygen free copper
Coil cooling	Low conductivity DM water
Coil slot	Length 800 mm and width 80 mm at coil
Between two coils	40 cm

While assembling the iron stack, layers 0, 5 and 10 were pasted with search coils using tapes and 3 mm shims were kept in between adjacent plates for fixing the gap for hall probe PCB strips. This was done to perform the magnetic field measurements.

4.1.1 Magnetic field measurement system

There are various Finite Element Methods (FEM) [54] based software packages to generate the B-field map in the material under study. In order to get accurate results the chosen mesh size needs to be small and the degree of polynomial should be high during the course of computation of the magnetic field. Both the conditions demand high computational time and memory. As a result a proper optimization of mesh size and degree of polynomial is required to reduce the computational time and memory. Also, to validate simulation results, a

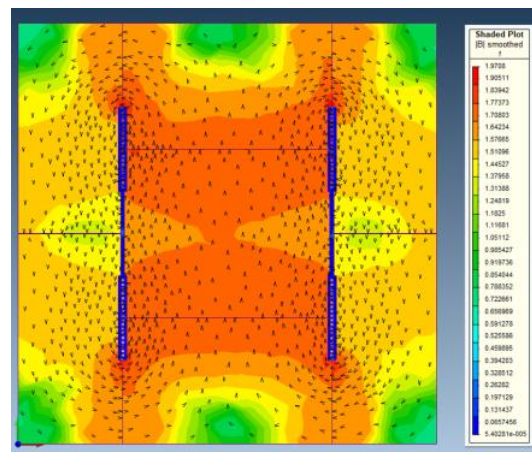


FIGURE 4.6: The magnetic field inside one iron plate generated from MagNet software.

measurement of the B-field in m-ICAL is needed. Therefore the magnetic field was measured by using two standard techniques

a) **Hall probe sensors** :- In the presence of a transverse magnetic field, the moving charges in a current carrying material deviate from the straight line path as they experience the Lorentz force due to the applied B-field. This leads to a voltage difference (V_H) in the direction perpendicular to both current and applied B-field. This voltage is directly proportional to the applied B-field. This phenomenon is

called the Hall effect and often employed to measure the static as well as dynamic magnetic fields. As mentioned in last section that in three layers of iron (0, 5 and

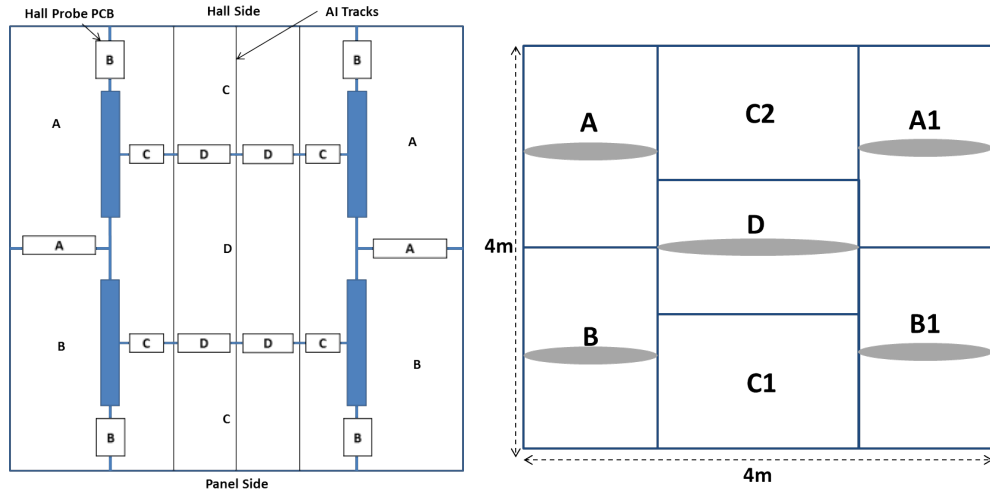


FIGURE 4.7: Schematic showing placement of Hall probes (*left*) and search coil (*right*) in iron plate.

10) provisions were made for placing Hall probe [55] sensors. The Hall sensors used were made of GaAs Mono Crystal material capable of measuring magnetic fields of strength up to 3 Tesla. It supports full scale accuracy of 0.2% with an output voltage of 110 to 150 mV at $B=100$ mT, $I=8$ mA, $V=6$ V and input power 150 mW. The Hall sensors were mounted on PCB strips which could be inserted in the air gaps between iron layers so that the sensor current was perpendicular to the B-field. The strips were wrapped with Mylar sheets which prevents any physical damage to the PCBs. Four configurations of Hall probe PCB strips were used namely A, B, C, D and described in Table 4.3 and their position in the iron layer is shown in Fig. 4.7

In the first phase of detector installation only the zeroth iron layer was populated with total 14 hall probe strips (totaling to 150 hall sensors) and the magnetic field

TABLE 4.3: Spacer and plate layout.

Type	No. of Strips	Shape	Dimensions (mm)	No. of sensors
A	2	T	$900 \times 37 \times 1.5$	15
B	4	T	$720 \times 37 \times 1.5$	15
C	4	Mounted on Al stand	$252 \times 37 \times 1.5$	4
D	4	Mounted on Al stand	$600 \times 37 \times 1.5$	11

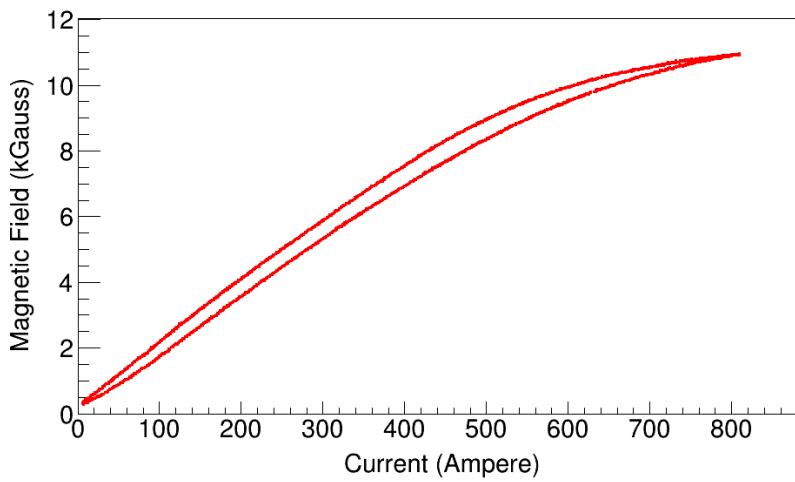


FIGURE 4.8: B-I graph measured from one of the Hall probe strip located in the center of plate D and C1.

measurements were performed for the same. It was found that at 900 A current 90% of the hall sensors were showing the magnetic field to be more than 1.3 T. A measurement from sensor D is shown in Fig. 4.8 while ramping up and ramping down the current in the coils.

b) **Search coils** :- The plates A, B, A1, B1 and D as labeled in Fig. 4.7 were wound by Teflon coated wires hereafter referred to as search coils[56]. Each wire had a single turn with a cross section of 0.25 mm^2 and 2 sets were installed for redundancy in case of breakage of any one of them. Analog signals from the search coils were amplified and integrated over a period of time to get the field

value. Each plate had 4 search coils (2 locations, 2 coils per location). A flux meter was provided for search coils wound on each plate except for the D type plate for which two flux meters are provided. A total 6 flux meters were fixed on the concrete pedestals. Drift can be adjusted to zero by pressing the drift button and reset button is provided to reset the integrator. The specifications of the flux meter are given below.

Full Scale range: 3250 k Maxwell Turns

Resolution: 650 Maxwell Turns

Accuracy: 3%

The terminals of one search coil or series combination of search coils from a plate are connected with wire coming from corresponding flux meter box using spring terminal connectors. It was ensured that the connection should be in such a way that the polarity of flux meter output matches with the expected polarity. The connection has to be reversed in case polarity does not match. Also, each flux meter is connected with the control panel. The average field in the plates with the search coil was calculated from simulation. Corresponding values have been compared with those measured using search coil method. The observations are given below in Table 4.4. The variations in the average field measured and

TABLE 4.4: Comparison of magnetic field from simulation and measured using search coil.

Plate	Average field from Simulation (T)	Field measured using search coil (T)
B	1.233	0.96
B1	1.313	1.4
A	1.235	1.3
D	1.6	1.5

simulated values are within 6% to 30% of the Hall probe measurements whereas the corresponding numbers using search coil is around 4.6% to 28%. The variations could rise from assembly tolerance and plate machining as also due to the accuracy of the measurement system which is about 10%. The magnetic measurement accuracy may be further improved by multi-point calibration of each hall probe sensor up to 1 T field. The search coil based measurement result may be further improved by reducing the drift, both in the short and long term.

4.2 Detector

The central $\sim 2\text{ m} \times 2\text{ m}$ area was populated by RPCs in between 10 gaps of the magnet assembly. In this section, various steps involved in the RPC assembly, the detector components, electronics and DAQ are discussed.

4.2.1 RPC assembly

RPC assembly comprises of three main components viz., gas gap, pick up panels and the front end electronics to amplify and process the raw pulses from RPCs. The gas gaps used in the m-ICAL were fabricated at the Saint Gobain company in Sriperumbudur, near Chennai, India. A gas gap was made by putting together two 3 mm thick float glass plates of bulk resistivity $\sim 10^{12}\Omega\text{cm}$ and dimension $1.8\text{ m} \times 1.7\text{ m}$. A uniform gap of 2 mm was maintained by placing 2 mm thick plastic buttons in an optimized grid fashion inside the gap and side spacers around the edges. The glass plates were glued with the buttons and side spacers by the use of 3M Scotch-weld epoxy adhesive DP190 Gray [57] in a duo-pack cartridge. Due to high resistivity of the glass electrodes a coating of conductive paint from

Nerolac (of surface resistance $\sim 100 - 300 \text{ k}\Omega/\square$) was done on both sides of the assembled RPC gas gap. This coating helps in uniform application of high voltage over the gas gap and limiting the fast pulse spatially. The gas gap was then sandwiched between two honeycomb pick up panels. The side of the pick up panel which faces the glass plate was pasted with copper tapes of size 2.8 cm with a gap of 0.2 cm and the other side was pasted with thin aluminium sheet. The pick up panels were placed with copper strips orthogonal to each other to measure the X,Y position of the hit. Two mylar sheets were cleaned and cut exactly of the size of the glass plates and were placed in between the gas gap and the pick up panels. This was done to electrically isolate the graphite coating with the copper strips in the pick up panel. The side spacers were provided by nozzles for flowing gas inside the chamber. The gas mixture of 95.2% R134a ($\text{C}_2\text{H}_2\text{F}_4$ or Tetra fluoroethane), 0.3% Sulphur Hexafluoride (SF_6) and 4.5% of Isobutane ($i\text{C}_4\text{H}_{10}$) with pressure few mbar (above atmospheric pressure) was flushed in the RPCs. A closed loop gas system procured from a Mumbai based vendor was employed for the gas circulation in 10 RPCs in m-ICAL.

4.2.2 Gas system

An automated gas circulation system was required for mixing and circulating the gas mixture inside all RPCs. To have an economical and environment friendly experiment the gas circulation system should be configured to operate in closed loop mode of operation where the mixed gas coming out of RPCs is re-compressed, purified and recirculated again in the RPCs. To standardize this technique, a Closed Loop Gas System (CLGS) [58] was installed for the m-ICAL detector.

CLGS was designed with a flow rate of few $0.01 \text{ m}^3/\text{h}$ and a gas renewal rate of $\sim 0.3 \text{ m}^3/\text{h}$. A schematic showing the flow of mixture of gases in CLGS is shown in Fig. 4.9.

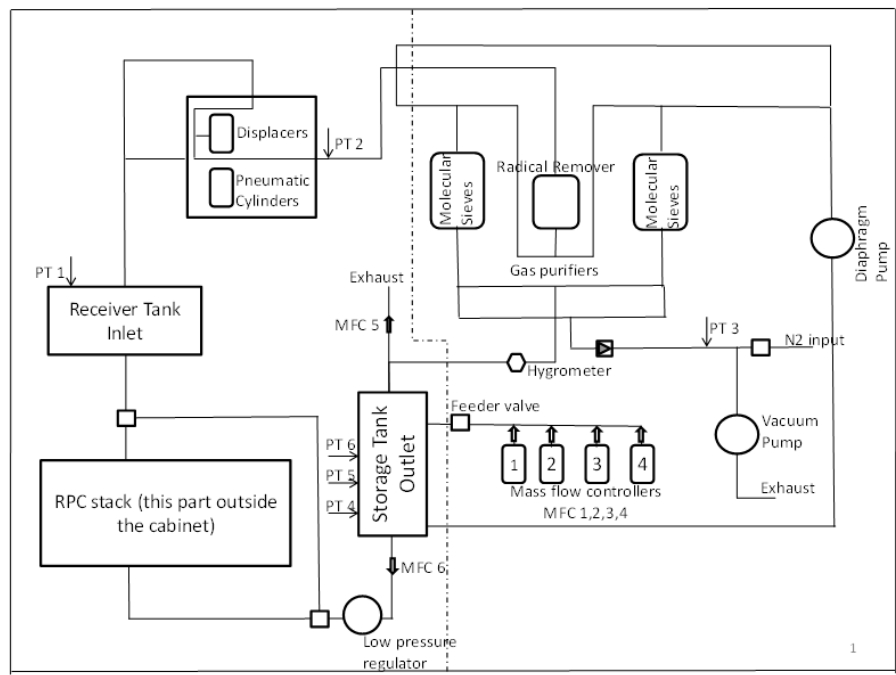


FIGURE 4.9: Closed loop gas system.

4.2.3 Electronics and Data Acquisition

Front End Electronics

The mini ICAL electronics process 1280 electronic channels and records the X-Y co-ordinates and time of flight of interaction of trajectory in the detector on satisfying the trigger criteria. The fully packed RPC and Front End electronics were placed in a tray of dimensions $1910 \text{ mm} \times 1950 \text{ mm}$. For a single RPC there were total 128 (64 from each X and Y side) signals which were collected by coaxial cables and connected to the pre-amplifiers and further digitized by

the discriminators. An 8 channel, preamp-discriminator board was connected to RPC pickup panel readout. Two types of pre-amplifiers were used in the m-ICAL detector namely those based on the ASICs, NINO[59] and ANUSPARSH[60], as shown in Fig. 4.10. The specifications of the pre-amplifiers are mentioned in Table 4.5. Only one of the layers of m-ICAL was connected to ANUSPARSH pre-amplifiers and the signals from the remaining nine layers were amplified using NINO pre-amplifiers.

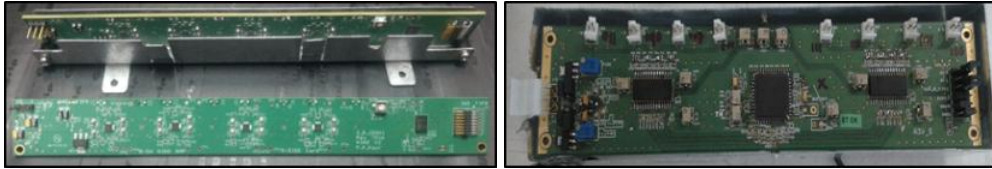


FIGURE 4.10: NINO (left) and ANUSPARSH (right) along with board.

TABLE 4.5: Specifications of NINO and ANUSPARSH

Description	NINO	ANUSPARSH
No. of channels per pre-amp board	8	8
Size of the board	200 mm × 23 mm	200 mm × 45 mm
Outputs	LVDS	LVDS
Power Consumption	70 mW/ch	32 mW/ch
Bandwidth	620MHz	500MHz
Amplifier type	Trans impedance	Voltage
Threshold	80fC	25mV
Developed by	ALICE Experiment Switzerland	BARC India

Each RPC had a dedicated FPGA based data acquisition module called RPC-DAQ [61] which was placed on one corner of the tray. It has 128 channels which receives 128 LVDS input signals from Front End Preamp boards of one RPC. The major functionalities of RPC-DAQ comprises of latching the input signals on trigger, reading timing information from High performance Time to Digital

Converter (HPTDC[62]) chip, rate monitor, pre-trigger generation, ambient parameter monitor and front-end control.

Trigger, Data Acquisition and Calibration for mini-ICAL

The pre-triggers from RPC-DAQs are processed through $M \times N/P$ fold trigger criteria in a central trigger system [63] to produce a final trigger. On a final trigger, each RPC-DAQ records locally the x-y hit data, time of flight (TOF) relative to final trigger arrival and trigger time stamp as event data. The event data packets from all RPCs are pushed over ethernet[64] links independently to back-end servers called data concentrators. The event builder server collates segmented event data packets with reference to trigger data packet using event time stamp recorded from Real Time Clocks (RTCs). The centralized calibration system is used to set and synchronise RTCs in all data recording nodes. The final trigger arrival time offsets at each recording node are also recorded along with RTC time stamp in the calibration event. These trigger time offsets are added to TOF measurements in respective RPCs to get the TOF data for the whole detector with common reference.

Trigger logic

The embedded RPC-DAQ processes 64 signals each in X & Y planes and produce four M fold (where $M=1$ to 4 consecutive pick-up signals) pre-triggers per plane using a coincidence window of 50ns. These pre-triggers from 10 RPC-DAQs are processed separately for X and Y planes in a centralized Trigger system using N fold trigger criteria where N is the M fold pre-triggers from consecutive N RPC layers. The final trigger is derived from $M \times N$ criteria either in X and Y

planes and the $M \times N$ combinations adapted in Mini-ICAL are $1 \times 5, 2 \times 4, 3 \times 3, 4 \times 2$.

Data acquisition

On a final trigger, the trajectory data is recorded locally in the embedded electronics of RPCs(RPC-DAQ) processing 64 pick-up signals each in X and Y planes. On a final trigger arrival in a RPC-DAQ, the RPC-DAQ latches the GPS synchronized Real Time Clock(RTC) event time stamp and x-y pick-up signal hits and the time to digital converter (HPTDC) measures TOF of hits relative to final trigger arrival. The RPC event data packet mainly comprises of event number, event time stamp, x-y pick-up signals hit data and time of flight measurement of hits. The centralized trigger logic records trigger data packet on every final trigger which mainly comprised of event number and time stamp. These data packets are pushed to back end servers over Ethernet links for event building in the whole detector. The RPC-DAQs as well as trigger systems periodically monitors the health of RPCs and trigger system respectively. These monitor data packets are also pushed over ethernet to the back-end monitoring servers. The RPC DAQ also interfaces over a SPI link to control and monitor the high voltage applied to RPC and its current.

Calibration and Auxiliary Unit (CAU)

The primary task of the calibration events [65] is to set and synchronize the RTCs in all the event nodes. The calibration unit also supplies a common stable reference clock of 10 MHz and 1 PPS GPS signal to all the nodes for synchronization. The relative time offsets of final trigger arrival at each node are recorded with a precision of 100ps in the periodic calibration events during the observation.

Power Supply

For powering up the front end electronics and applying high voltage to the RPCs, two types of power supply modules were used. The Front-End electronics was powered by a common low voltage power line driven by CAEN's EASY 3000 System with 3 Mod. A3025 [66] power supply boards. The RPCs were biased to $\sim \pm 4900\text{V}$ using CAEN's SY2527 Multichannel Power Supply System with the 1832 P and N HV modules. In one of the layers RPC is being biased with HV module indigenously developed by BARC. Eventually all layers would go on these home made modules.

4.3 Basic test of the RPCs

Before assembling the RPC, there are certain preliminary tests which needs to be performed for qualification of the gas gaps. Three such tests are listed in the text below.

Leak test

After gluing the gas gap it becomes essential to find out whether it is leaky or not. The first test which the RPC undergoes was leak test which was performed for all the gas gaps before assembling the RPC. There is conventional manometer method in which the leak could be identified by observing the changes in the level of water column over a long period of time. However, the major drawback of such a method is that it should be performed in non-varying ambient pressure and temperature. Due to the high dependence of RPC gas gap pressure on the ambient pressure it is almost impossible to detect small leaks by conventional manometer techniques. Therefore, a new Raspberry Pi based leak test set up, as

discussed in [67] was used to perform leak test for the gas gap used in m-ICAL. The basic aim of new leak test set up is to monitor the pressure inside RPC gas

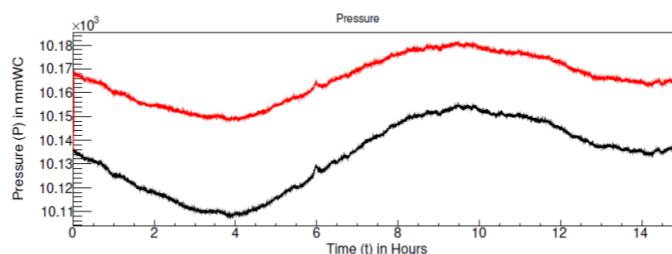


FIGURE 4.11: Pressure vs time curve for one of the RPC gas gaps. The Red curve is for the RPC pressure and the Black curve is for ambient pressure.

gap in the presence of variation in ambient conditions. All the gas gaps were subjected to a leak test by pressurizing the gap up to 45 mm Water Column and sealing it. Two sensors were used, one for measuring the ambient pressure and second one measuring the RPC gas gap pressure. Only those gas gaps were selected in which the RPC gas gap pressure is maintained. Typical pressure vs time for a period of 14 hours is shown in Fig. 4.11.

Surface resistivity measurement

The second test was to measure the surface resistivity [68] of the glass gas gap for checking the uniformity of the applied graphite coat. It was measured by using indigenously developed jig (shown in Fig. 4.12) made up of copper with dimension $15\text{ cm} \times 15\text{ cm}$. The surface resistance of all the gas gap was measured in two orientations of the jig 'H' and 'I'. A typical 2D surface resistance map of both side of the gas gap is shown in Fig. 4.12. A gap was accepted if 95% of the area was having surface resistance more than or equal to $0.5\text{ M}\Omega/\square$. After these two tests of the gas gaps, they were packed by placing honeycomb based pick-up panels at top and bottom and the packed RPC was subjected to high voltage test.

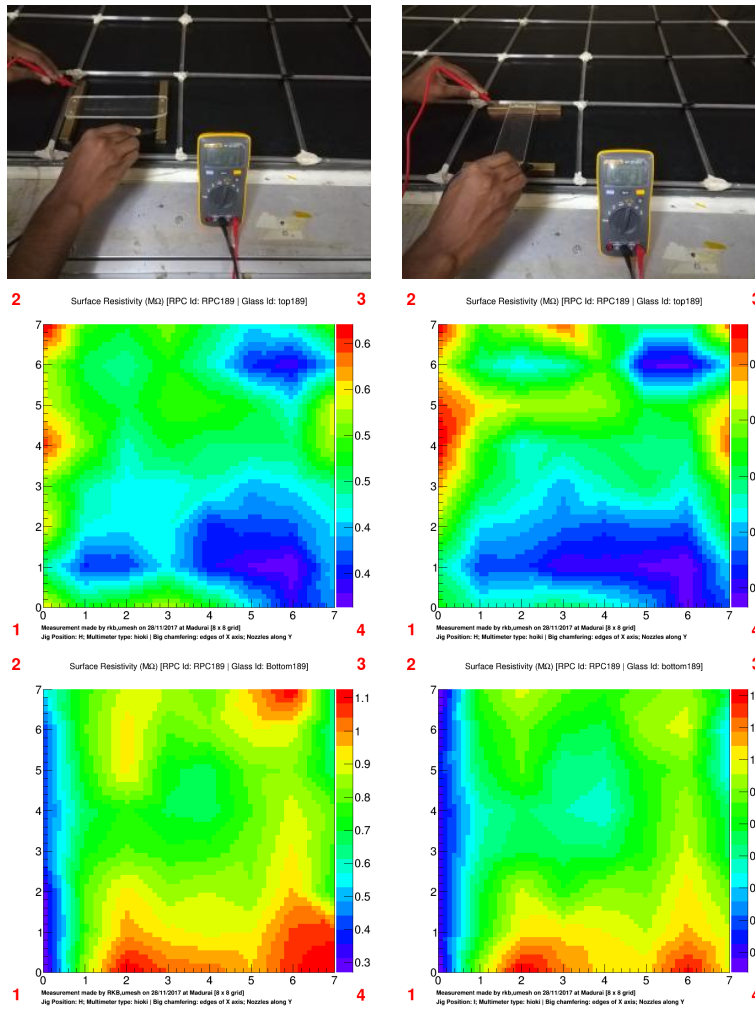


FIGURE 4.12: Copper and brass jig for measuring the surface resistance of the graphite coating paint (top row), the middle row shows the surface resistance of one side of the gas gaps with ‘H’ and ‘T’ orientation of the jig and the other side is shown in the bottom row.

I-V characteristics

I-V characteristics of all the RPCs were measured before pushing them inside the m-ICAL magnet assembly. A CAEN based power supply with model number PS 191 was used for this purpose. Fig. 4.13 shows the current vs high voltage curve for one of the RPC. At low voltages the current is only due the resistance

of spacers and buttons but as the HV increases the RPC gas gap resistance becomes low and it starts conducting. This is reason for getting two slopes in I-V characteristics curve. If the I-V response was not satisfactory it was rejected and

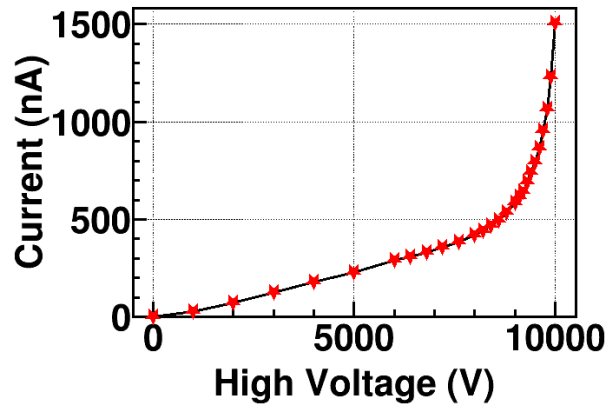


FIGURE 4.13: I-V characteristics of one of the RPC.

a new one tested. The trays with RPCs which had passed the tests mentioned were then pushed inside the m-ICAL magnet assembly after mounting the front end electronics board on the tray.

4.4 Muon trajectories and efficiency of RPC

After pushing all the RPC in the iron stack data was recorded at 900 A current in the coils and the first few tracks are shown in Fig. 4.14. It should be pointed out that depending upon the flow of current in the coils, the magnetic field is in the Y direction therefore bending of the muon tracks is in X direction. The trigger criteria was logic AND of any 5 out of 8 consecutive layers. The trigger rate was observed to be ~ 300 Hz. For calculating the efficiency of each RPC, 15 hours of data was taken with the same trigger criteria. The efficiency measurement was performed in the absence of any magnetic field. Only the events with maximum

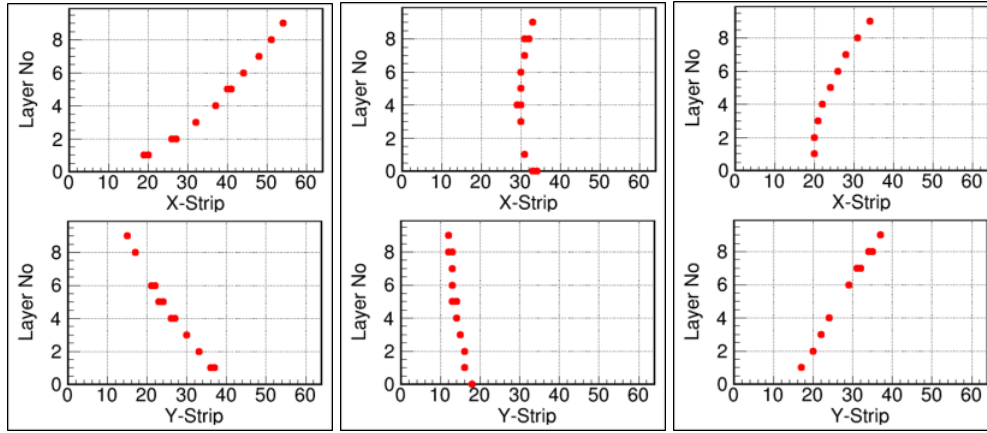


FIGURE 4.14: Few bend tracks in the m-ICAL detector at I=900 A

three consecutive strip hits in a layer are considered for this study. This criterion helps in removing a noisy layer without discarding the entire event. Independent fitting was performed in XZ and YZ planes using the accepted hit positions in all layers. A track was fitted with a straight line in both planes using the equation, $x(y) = a \cdot z + b$ where x or y is the hit position (average strip position) from the X- or Y- plane respectively for Z-th layer, 'a' is the slope and 'b' is the intercept. The exact position of the muon trajectory in all the RPC layers can be estimated using these four parameters. The fit was performed only if there are minimum 4 layer hit with the selected X and Y positions and χ^2/ndf of the fit was less than 8. The layer under study is excluded from the fit. Efficiency was measured by the presence of signal hit around the expected position. The pixel wise efficiency plot of all the layers is shown in Fig. 4.15.

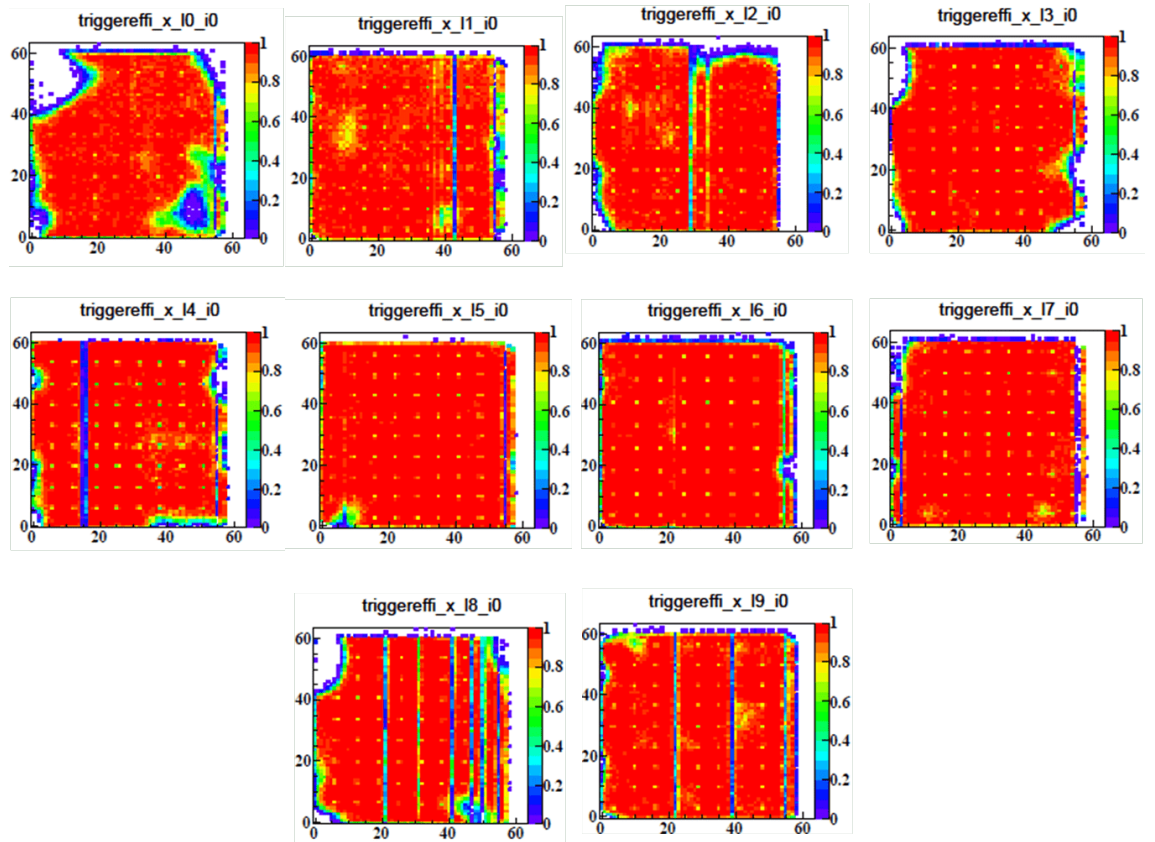


FIGURE 4.15: The trigger efficiencies of all the ten layers of RPC.

4.5 Summary

A $4\text{ m} \times 4\text{ m}$ magnet prototype detector of ICAL (m-ICAL) was built at IICHEP, Madurai. It is a 85-ton magnetized detector with 11 layers of iron and 10 layers of RPCs. Ten $2\text{ m} \times 2\text{ m}$ RPCs were assembled and characterized by performing various measurements. The magnetic field was measured in the gaps in the lowest layer of m-ICAL using the Hall probes. In addition the fringe field outside, but in proximity to, the m-ICAL detector was also mapped.

An attempt to measure the magnetic field in iron using Muon Spin Rotation in mini-ICAL

Cosmic ray muons have a partial longitudinal polarization of about 23% [69] as a result of two factors - parity violation in the weak decay of pions (produced in cosmic ray protons interactions with the upper atmosphere) and a sharply falling energy spectrum of these pions. If these partially polarized muons are stopped in an absorber then the degree of polarization of the absorber can be studied by detecting the decay electron. For measuring the polarization, the absorber should be symmetrically placed in between two charged particle detectors, placed above and below it, which can measure the arrival time of the muon and the time of decay by detecting the electron. Depending upon the absorber there will be a difference in the counts of the detected electrons in the two detectors. For example a 100% polarized muon beam is completely depolarized in iron as measured

by [30] because in the absence of any polarizing magnetic field the domains inside the iron are randomly oriented. An introduction to the μ SR technique for measuring internal magnetic fields in condensed matter has already been given in Chapter 1. Before setting up the experiment for measuring the magnetic field inside iron using the μ SR technique, it was thought worthwhile to attempt measuring the depolarization of cosmic muons in iron. With this motivation, as a first step, lifetime measurements of stopped cosmic muons inside the soft iron were performed using a 12 layer RPC stack (section 5.1) and a plastic scintillator based detector (section 5.2). An attempt to measure the magnetic field inside iron in the magnetized mini-ICAL is also described in the section 5.3 of this chapter.

5.1 Studies with 12 layer stack of RPC

A 12 layer RPC detector stack (without magnet) has been working at the Tata Institute of Fundamental Research, Mumbai since the last 10 years or so. It has been used to study the cosmic muon flux and carry out R & D on the RPC detectors and associated electronics [38]. The total height of the stack is 176 cm and the gap between two layers is 16 cm which makes it possible to carry out muon lifetime measurement by inserting a reasonably thick iron plate in the gap. A support stand was made to place the iron plate in one of the gaps in the RPC stack. After inserting the support structure the available gap reduces to 5 cm. A 5.6 cm thick iron plate is going to be used in the ICAL detector, therefore it would have been ideal to measure the lifetime of muon in 6 cm thick iron plate by stacking 3 layers of available iron plates (2 cm thick) in the lab. However, the available space allows placement of either 4 cm (two layers) or 2 cm (1 layer)



FIGURE 5.1: 12 layer stack of RPC.

thick iron plate(s) in the gap. The number of decay electrons that come out of the 4 cm iron plate is expected to be significantly smaller than those from a 2 cm thick plate. For the preliminary studies it was essential to use the thickness of iron plate which would result in maximum detection efficiency. A GEANT4 based Monte Carlo simulation was carried out by incorporating the full geometry of the 12 layer RPC stack to compare the decay electron detection efficiency for the 2 cm and 4 cm thick iron plate.

5.1.1 GEANT4 based simulation

The complete geometry of the RPC stack along with the detector hall which is made up of concrete was input in the GEANT4 simulation as shown in Fig. 5.2. In the geometry, an iron plate of surface area $1\text{ m} \times 1\text{ m}$ was placed in the gap between the layer 2 and the layer 3. Muons with energy distribution varying

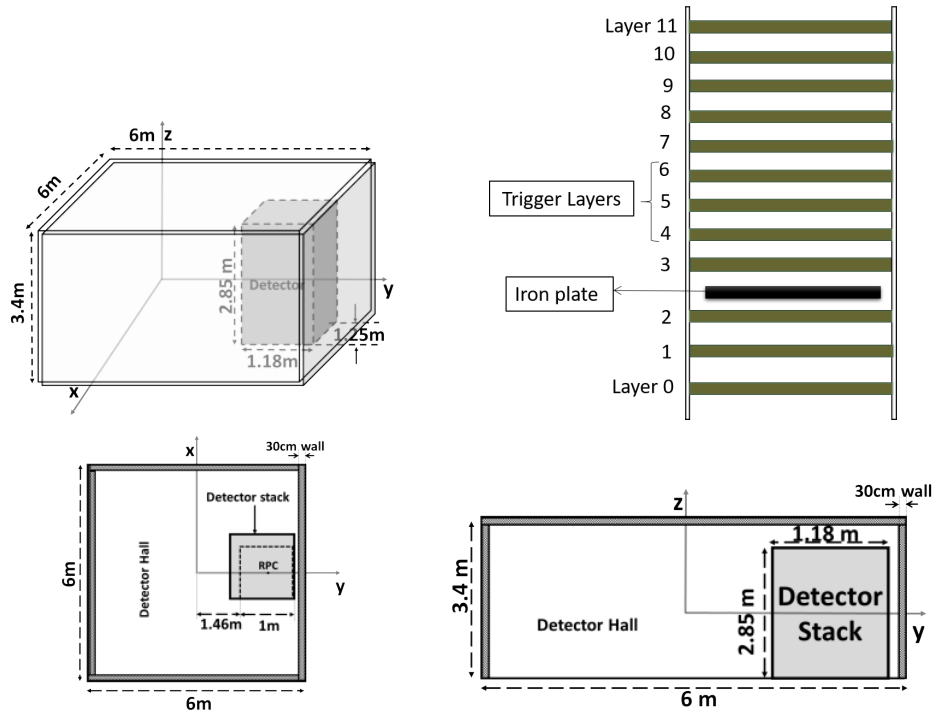
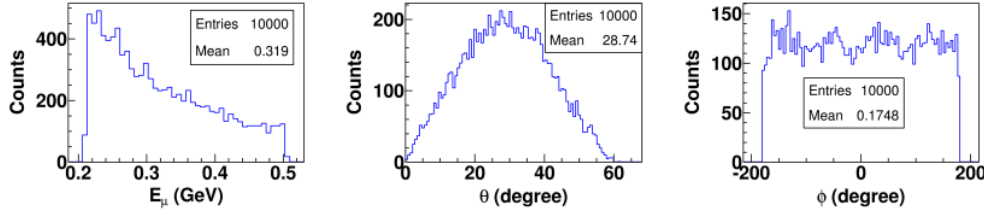


FIGURE 5.2: The geometry of the RPC stack and detector hall in 3D view, top view, side view and the schematic showing the RPC stack along with 2 cm thick iron plate placed in between layer 2 and layer 3. (*anti-clockwise from top left*)

as $E^{-2.7}$ were generated randomly at the surface of the ceiling and allowed to travel downwards to the detector. The zenith angle, θ was generated using $\cos^2\theta$ distribution in the range of 0 to 60 degree. The azimuthal angle, ϕ was generated randomly from -180 to +180 degree. The energy of the muon was generated in the energy range of 0.2 GeV to 0.5 GeV. The input (E, θ, ϕ) spectra given as input to the simulation is shown in Fig. 5.3. Coincidence of muons in L6, L5, L4 and L3 was used as a trigger for the muon decay event. For every random set of (X, Y, θ, ϕ) , the intersection of the line passing through the point (X, Y) and all four trigger layers was checked. Only if the line intersects with the trigger layers, then the given set (X, Y, θ, ϕ) was accepted. Two thicknesses of the iron plate,

FIGURE 5.3: The E, θ, ϕ spectra input to the simulation.

2 cm and 4 cm, were considered in the simulation.

TABLE 5.1: Parameters of the simulation

Description	2 cm thick iron plate	4 cm thick iron plate
Total no. of events	10000	10000
No. of muon decays	803	1553
Detected decay in RPC	248	254
Detection efficiency	31%	16%

The outcome of the simulation is summarized in Table 5.1. It can be seen from the Table 5.1 that the detection efficiency is ~ 2 times more for 2 cm thick iron plate.

5.1.2 Experimental Set up

An iron plate ($1 \text{ m} \times 1 \text{ m} \times 0.02 \text{ m}$) was placed between the 2nd and 3rd layers in the RPC stack to perform the experiment as shown in Fig. 5.4. The detector consists of 12 layers of $1 \text{ m} \times 1 \text{ m}$ RPCs, stacked one on top of another with a gap of 16 cm. Each RPC is having 32 readout strips on both sides of the RPC gas gap. The strip pitch is 3 cm as the width of the strip is 2.8 cm and the gap between two strips is 0.2 cm. The two readout planes of RPC were labeled as X and Y where the strips in the X plane were orthogonal to the strips in the Y plane. The RPCs were operated in the avalanche mode and the efficiency of the

layers was about 95% at an operating voltage of 9.9 kV. The time resolution of the chambers is ~ 1 ns. For ensuring the passage of muons through layer 3, the

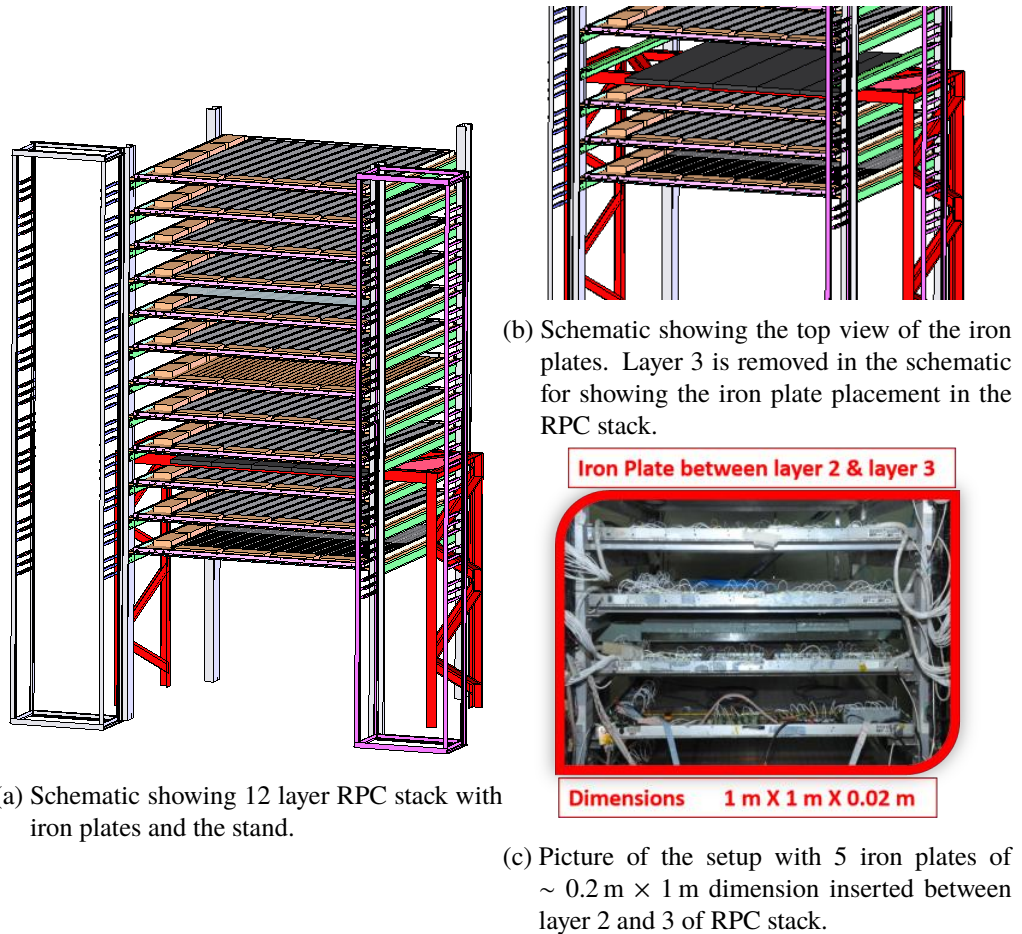


FIGURE 5.4

trigger was generated by a logical AND of L6 & L5 & L4 and the trigger rate was observed to be ~ 50 Hz. If the muon decays in the absorber (iron) then the decay electron can be detected in either L2 (bottom) or L3 (top) which will generate a delayed signal in the respective layer.

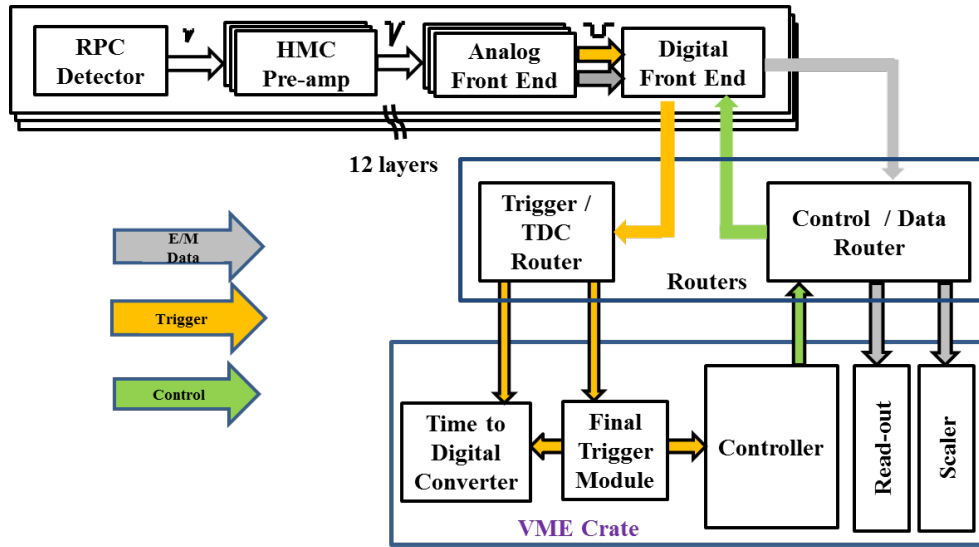


FIGURE 5.5: Schematic of the data acquisition system for 12 layer RPC stack.

5.1.3 Electronics readout and DAQ

A block diagram of the signal electronics readout is shown in Fig. 5.5. The hit position and timing information of the events occurring with a specified pattern in the RPC stack was stored in the DAQ. There are total 768 electronic readout channels in the RPC stack. Therefore, the challenge of the DAQ design was to handle this many number of channels. As the RPCs were operated in the Avalanche mode, the amplitude of a typical RPC pulse was low (~ 2.5 mV across a 50Ω load). Hence, a Hybrid Micro Circuit (HMC¹) based preamplifier is used with a gain of ~ 80 for amplifying the pulses. These pulses were amplified by using a high speed, low noise pre-amplifier. Depending upon the polarity of the induced signal two different types of pre-amps were used, namely, BMC 1595 and BMC 1597 (with gain 10) for the first stage. In the second stage BMC 1513 was used with a gain of 10. The analog and amplified output from the pre-amps

¹designed by the Electronics Division of Bhabha Atomic Research Centre (BARC), Mumbai and fabricated at the Bharat Electronics Ltd. (BEL), Bengaluru

were given to the AFE (Analog Front End) boards. In the AFE, the amplified signals were discriminated by a threshold of -20 mV. Level 0 trigger signals were also formed in the AFE by logically OR-ing the discriminated pulses from every 8th channel. The pulse width was shaped to 100 ns.

All the discriminator pulses and level 0 trigger signals were then fed to the DFE (Digital Front End) board. In the DFE, the width of the discriminator signal was increased to 750 ns. The pulse width was increased in order to take into account the trigger latency in the DAQ system. The fold signals (or level 1 signals) were also formed in the DFE. This board communicates with two routers namely Trigger/TDC router (TTR) and Control/Data Router (CDR). The TTR board routes the level 1 signals to the FTM for the final trigger formation. Once the trigger is generated in the FTM, it is sent to the INO controller and multi hit TDC (CAEN model V1190, which is based on CERN developed HPTDC). The INO controller sends a signal to the CDR board by which it generates the control signals to read the strip hit data from the DFEs. So for a particular event the hit information and the timing information of the layers 0-1 and 4-11 was stored in the backend (iDaq).

However, two separate TDCs (CAEN V1190 and V1290) were connected to all the strips of Layer 2 and Layer 3. A separate VME crate was used for the separate TDCs. The trigger from iDAQ was fanned out into two signals, out of which one was delayed by $10 \mu\text{s}$ and was given to TDC as a trigger. Another trigger signal as a input to NIM to ECL Converter, for giving trigger as one of ECL input to TDC as reference channel. The timing diagram for the separate TDC is shown in Fig. 5.6.

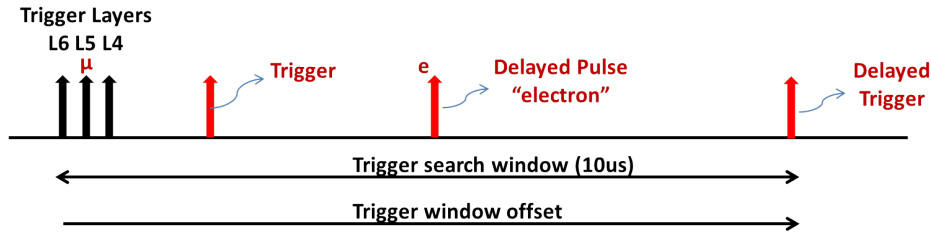


FIGURE 5.6: Timing diagram of the separate TDC connected to layer 2 and layer 3.

5.1.4 Data Analysis

The triggered events are stored in a binary file in the form of (X,Y) positions of the hits and a time for each layer. However, for layer 2 and 3 the strip hit information was stored in a separate multi-hit TDC as for a muon decay event time data for both the muon and the decay electron is needed. An example of three different types of events is shown in Fig. 5.7. Fig. 5.7(*Left*) shows a clean muon track passing through all the layers of the stack. Here as Layer 2 and 3 were removed from the DAQ that is the reason of not seeing any hit in these layers. An example of a noisy event is shown in Fig. 5.7(*Middle*). The track shown in Fig. 5.7(*Right*) is a possible muon decay event. The noise events can be filtered out by fitting the tracks with a straight line fit and looking at the goodness of the fit. Therefore, a straight line fit algorithm was used to fit the tracks in the RPC stack event by event. The expected strip hit in layer 2 or layer 3 can be predicted by extrapolating the straight line. For a particular expected strip, the TDC value was checked with respect to the trigger timing. It should be pointed out that there is no prompt signal in the bottom detector (layer 2) as muon has decayed in the iron which is just above the layer 2. Therefore, events in which the timing in the bottom detector in the expected strip is more than the trigger timing are identified as possible muon decay events. In case of layer 3 both the prompt

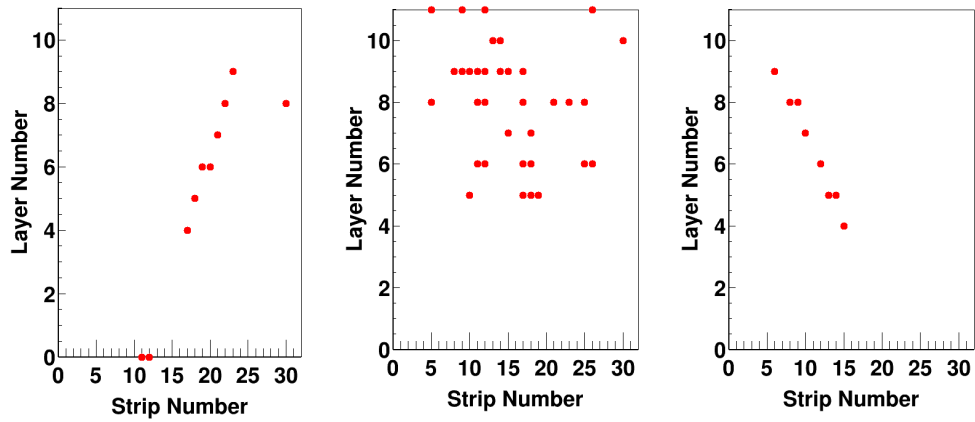


FIGURE 5.7: Examples of tracks from the RPC stack. *Left* A track passing through all the layers of the stack. *Middle* An example of noisy event. *Right* A possible candidate of a decay event.

muon signal and the delayed electron were present, therefore, the signals were considered when the timing of second hit is more than the trigger time. This event selection criteria is summarized below:

Layer 2

- No Prompt in layer 2
- If 1st hit timing in the expected strip > trigger timing
- Time delay = (time of 1st hit – Trigger time)

Layer 3

- Both Prompt & Delayed are there in layer 3
- If, 2nd hit timing > trigger timing
- Time delay = (time of 2nd hit – time of 1st hit)

The distribution for the muon lifetime is shown in Fig. 5.8. The data was fitted to the equation:

$$\Delta t = A \exp\left(\frac{t}{\tau}\right) + C \quad (5.1)$$

The fitted muon lifetime obtained for layer 2 and layer 3 are (2.09 ± 0.18) and $(0.148 \pm 0.007) \mu\text{s}$ respectively. The muon lifetime obtained in the layer 2 detector is in good agreement with the best known value [70]. However the measured muon lifetime in layer 3 is significantly less than the expected value. This is due to the fact that the passage of a muon induces an avalanche in the RPC and reduces the electric field locally, making it “dead”, for few ms. It should be pointed out that, in the case of magnetized iron the B-field can be extracted only from the time spectra of detector below the Iron plate.

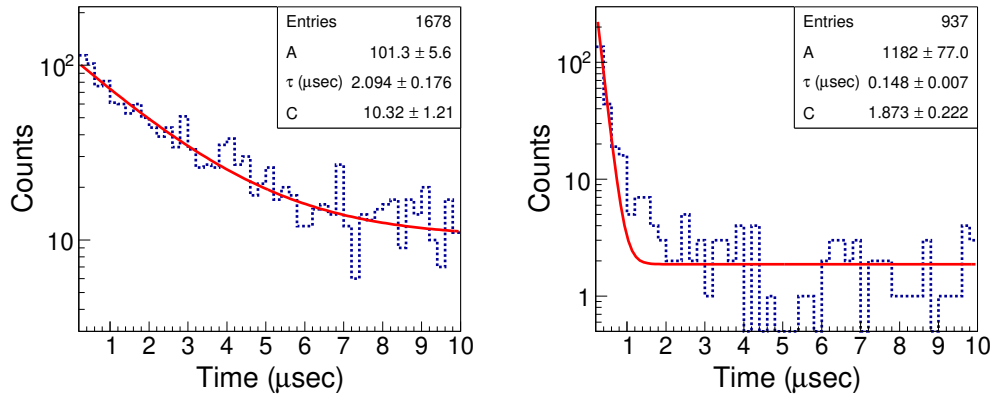


FIGURE 5.8: Time distribution of layer 2 (*Left*) and layer 3 (*Right*).

5.2 Studies with 5 layer stack of plastic scintillators

To overcome the limitation of the “dead time” in RPC, a plastic scintillator (PS) based experiment for observing the decay asymmetry in iron was conducted.

Five plastic scintillators (A,B,C,D,E) of dimension 96 cm × 32 cm × 1 cm were stacked one on top of other as shown in Fig. 5.9. Iron plate of dimension 90 cm × 40 cm × 2 cm was placed in the gap between PS D and E. A NIM based data

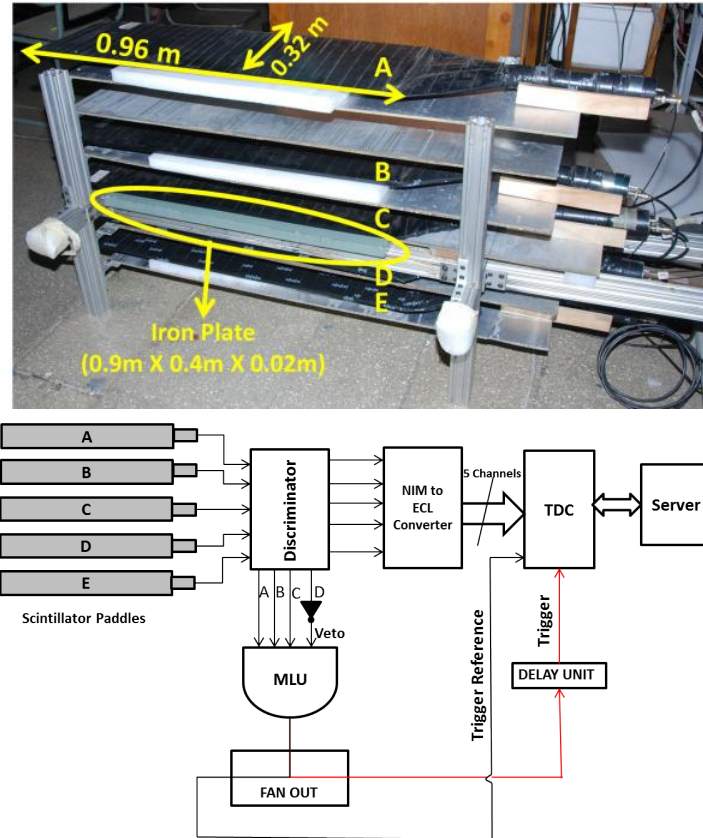


FIGURE 5.9: Set up of 5 layer PS stack (above) and the associated electronics (below).

acquisition was used for this experiment. The analog signals from all the PS were fed to CAEN discriminator (Model No. 841) with threshold 20 mV. The discriminator output was fanned out into two paths, one of which was given to the Majority Logic Unit (MLU) for generating the trigger ($A \cdot B \cdot C \cdot \bar{D}$) and other output (for all the PS) was given through NIM to ECL converter to the CAEN TDC (model no. V1190). The TDC timings of all the PS were stored. The

trigger was generated by a logical AND of A, B, C and not-D. Trigger was also fanned out into two signals. One of the triggers was fed to the TDC as reference for storing timing data of the trigger and the other trigger signal was fed to a TDC as a trigger with a delay of $10 \mu\text{s}$. If a muon passing through the stack stops in the Iron plate then the decay e^- could be detected in the top or bottom scintillator after a certain delay ($\sim 2 \mu\text{s}$). The time difference was considered as

For top scintillator:

the time differences between the trigger and delayed co-incidence of B&C.

For bottom scintillator:

the time differences between the trigger and delayed co-incidence of D&E.

The TDC data was analyzed by a C++ and ROOT based code. The histogram for the time difference of top and bottom PS are shown in and the histogram plots are shown in Fig. 5.10, left and right respectively. The time spectra were fit to Eq. 5.1. For top and bottom scintillator, the measured lifetime (τ) is (1.9 ± 0.2) and $(2.2 \pm 0.2) \mu\text{s}$ respectively, which, within errors, is consistent with known value of lifetime. However, the asymmetry could not be measured in this set-up due to ion feedback in PMTs due to after-pulsing in the PMTs that were used as shown in Fig. 5.11 as old PMT. Due to the ion feedback 10% of the times there was second pulse after $\sim 400 \text{ ns}$ of the muon pulse in the PMT resulting in a peak at 400 ns in the lifetime curve.

5.2.1 Ion Feedback in PMT

Ion feedback [71],[72] is a well known and undesirable phenomenon in a PMT which hinders it from becoming an ideal detector. The positive ions, if present

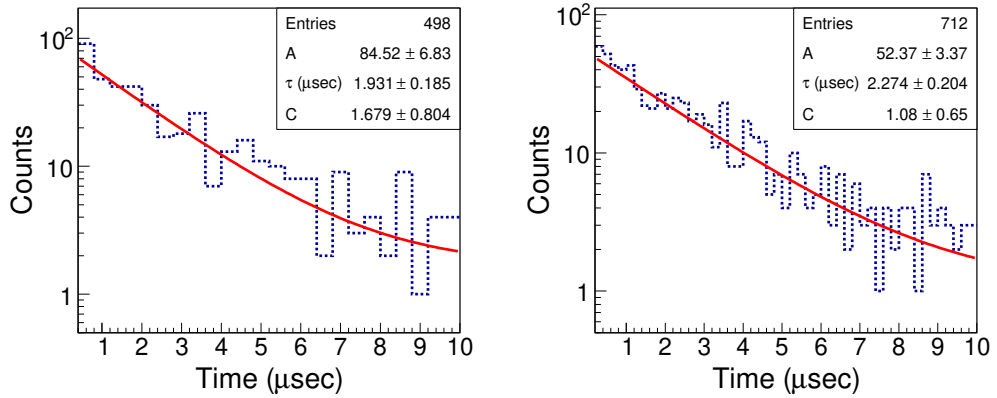


FIGURE 5.10: Time distribution of top (*Left*) and bottom (*Right*) scintillators.

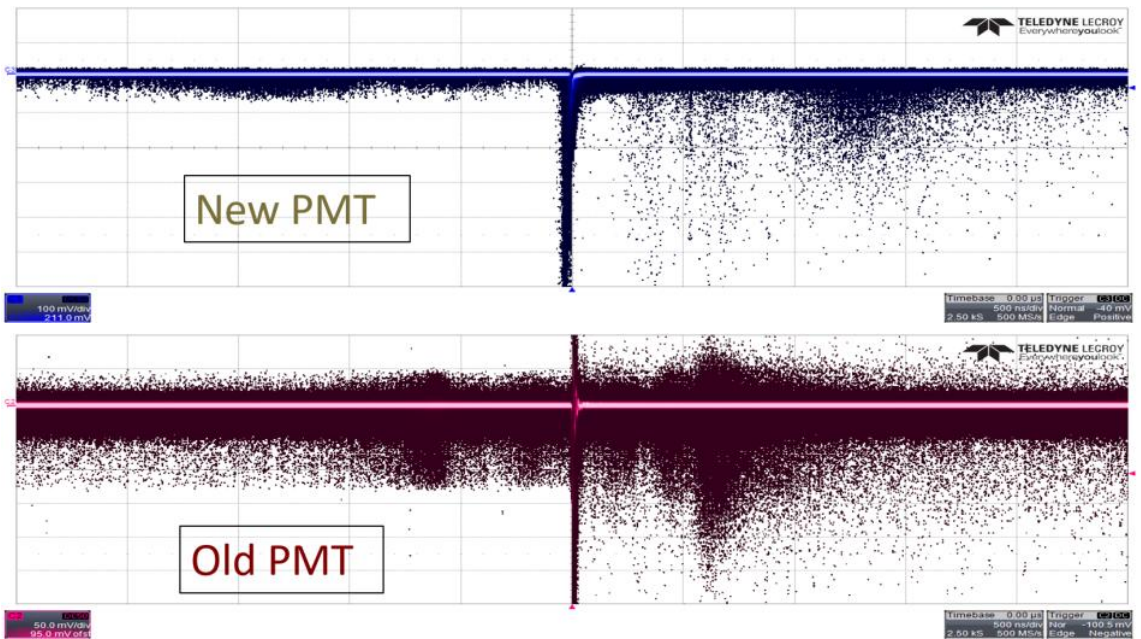


FIGURE 5.11: Screenshot from CRO showing ion feedback pulses for new and old PMTs.

in the vacuum tube, get accelerated towards the photocathode. This leads to damaging of the photocathode material and also, results in the noise as the ion can bombard on the photocathode and eject out few electrons which can mimic a photon induced signal in a PMT. A few reasons for the presence of ions in the

vacuum tubes are listed in what follows:

- 1) due to some residual gas in PMT,
- 2) sputtering - accelerated electrons from the cathode strike the first dynode and sputter out ions which travel back to cathode and emit secondary electrons,
- 3) hydrogen or oxygen ions which are absorbed from water molecule,
- 4) Cesium ions are particularly abundant in devices with in situ photocathode activation procedure.

As demonstrated in [73], the insertion of an electrostatic potential barrier close to the anode solves the ion feedback problem.

An attempt was made to reduce these after pulsing in the PMTs by reducing the voltage between the cathode and the first dynode. It was found that if this voltage was reduced by a factor of 2 the number of ion feedback pulses reduce by a factor of 10.

5.3 Search for μ SR signal in mini-ICAL

As described in Chapter 4, the mini-ICAL is a magnetized detector having 11 layer of iron plates. Hence, an attempt was made to measure the magnetic field inside the iron plates using the μ SR technique. The hardware trigger was set to be a logical AND of L9, L8, L7 and L6 (by convention L9 corresponds to topmost RPC layer) for this purpose. The trigger rate was observed to be ~ 200 Hz. This trigger condition led to observe the decay of muon in 6 bottom (L5 to L0) iron layers. The position (X,Y,Z) along with the TDC time was stored as hit information for every event, where (X,Y) was obtained from the strip number and Z was given by the layer number. The TDC trigger matching window (maximum

range of the TDC) was set to $21.5 \mu\text{sec}$. The trigger signal was fanned out into two signals. While one of the signal was fed to one of the TDC channels as the reference signal, the other was delayed by $21.5 \mu\text{sec}$ and used as the trigger for the TDC as shown in 5.12. When the TDC receives a trigger it latches all the time stamps which were available in the buffer. The reference signal was used as the time stamp of the muon trigger (t_m). A total of ~ 98 hours of data was

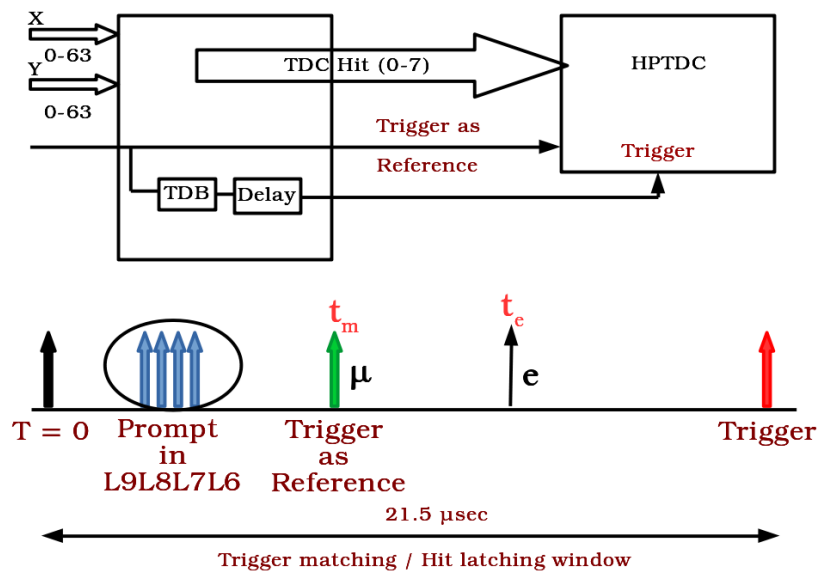


FIGURE 5.12: The timing diagram for the changes in the HPTDC of RPC-DAQ module

acquired. The average magnetic field during the measurement was 1.3 T. The data was analyzed off-line with a ROOT based C++ code. The analysis was done in three steps. In the first step, the noisy events were rejected by applying criteria on the event multiplicity and number of layers with hit. The filtered event should have

- At least one hit in all layers above the iron layer at which the muon decayed
- No hit in all the layers below the iron layer at which the muon decayed
- Hit multiplicity in the layer ≤ 3 with consecutive strip hits

In the second step, the filtered muon tracks were fitted with both linear and circular fit with signals within 30 ns time window. Since, magnetic field was applied in the Y direction, there should be no curvature in the Y side hits. Hence, the Y side tracks were fitted only with linear fit. The muon tracks were further filtered on the basis of the goodness of the fit. A χ^2 error for the straight line fit and the circular fit was accepted to be 25 and 50, respectively. In the last step, an expected XY position (X_0, Y_0) of the muon track in the layer below the iron plate was extrapolated from the fitted tracks. The tracks in which the expected XY position, in the layer below the iron plate, lie between 0 to 64 and has atleast one TDC hit were selected for further analysis. The hit within ± 2 strips of the X_0, Y_0 was identified as a decay electron and the TDC time of which was stored as t_e . The position and time of typical muon decay like events corresponding to all the 6 layers are shown in Fig. 5.15-5.17 (*left* X side and *right* Y side). The time difference between $\Delta t = t_e - t_m$ was plotted in a histogram with a bin size of 20 ns and the data was fitted with the Eq. 5.1 and the lifetime for the muon was calculated. Since the applied magnetic field was in the Y direction, the tracks with curvature in -X and +X direction are identified as μ^+ and μ^- , respectively. The distribution of Δt for μ^+ and μ^- along with the fit to the Eqn. 5.1 shown in Fig. 5.8. The muon lifetime obtained for the μ^+ and μ^- are $(2.21 \pm 0.01) \mu s$ and $(0.27 \pm 0.02) \mu s$, respectively.

In order to find the oscillation frequency (ω) a Fast Fourier Transform (FFT) of the Δt distribution with finer bin (500 ps) was calculated and is plotted in Fig. 5.14 (*left*). No peak could be seen at the expected frequency $\nu = 135.5 \frac{MHz}{T} \cdot 1.5 T = 203 \text{ MHz}$. The oscillatory behavior of the early part (upto 100 ns) of the μ^+

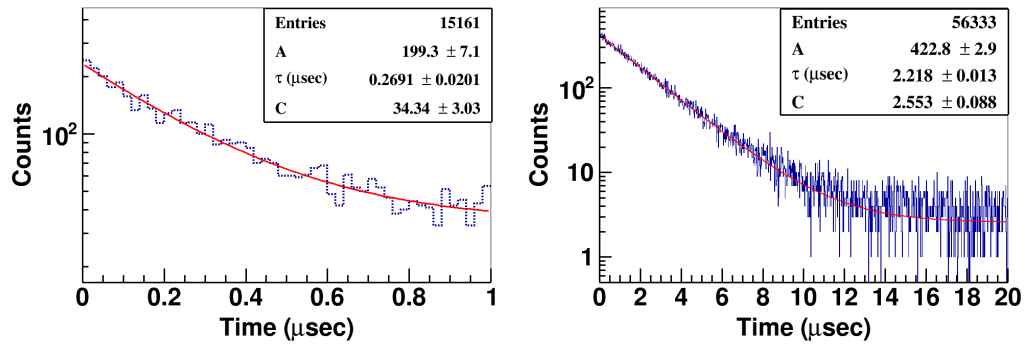


FIGURE 5.13: Time distribution of μ^- (Left) and μ^+ (Right) scintillators.

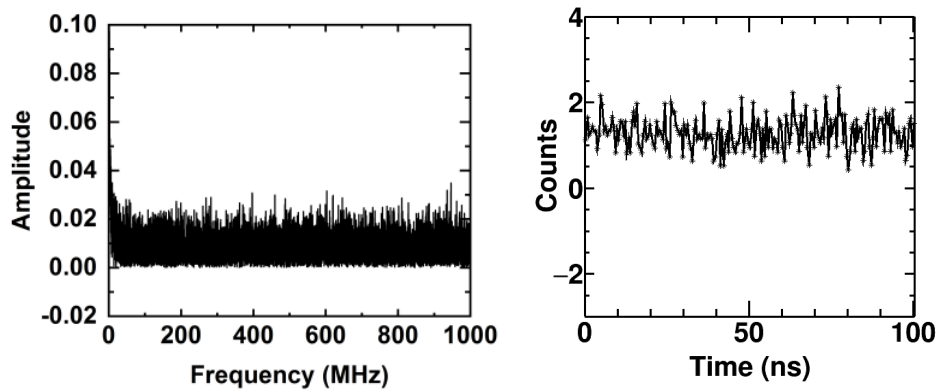


FIGURE 5.14: The FFT of the timing spectrum for μ^+ (left). The plot of the ratio between the number of counts in each bin and the value obtained from the fit function (right).

lifetime spectra was examined by dividing the data in 500 ps bins with the corresponding fitted value in that bin. Here also no oscillation was observed as it can be seen from Fig. 5.14 (right).

This absence of oscillations could be due to three possible reasons:

- 1) The data acquired was not enough to observe the oscillatory behavior overridden by a lifetime curve,
- 2) cosmic ray muon polarization is not retained in a 5.6 cm thick iron plate over the time period of observation,

3) due to ionization energy loss the decay electron is not able to come out of the iron plate, preserving, on the average, the directional information at the instant of muon decay.

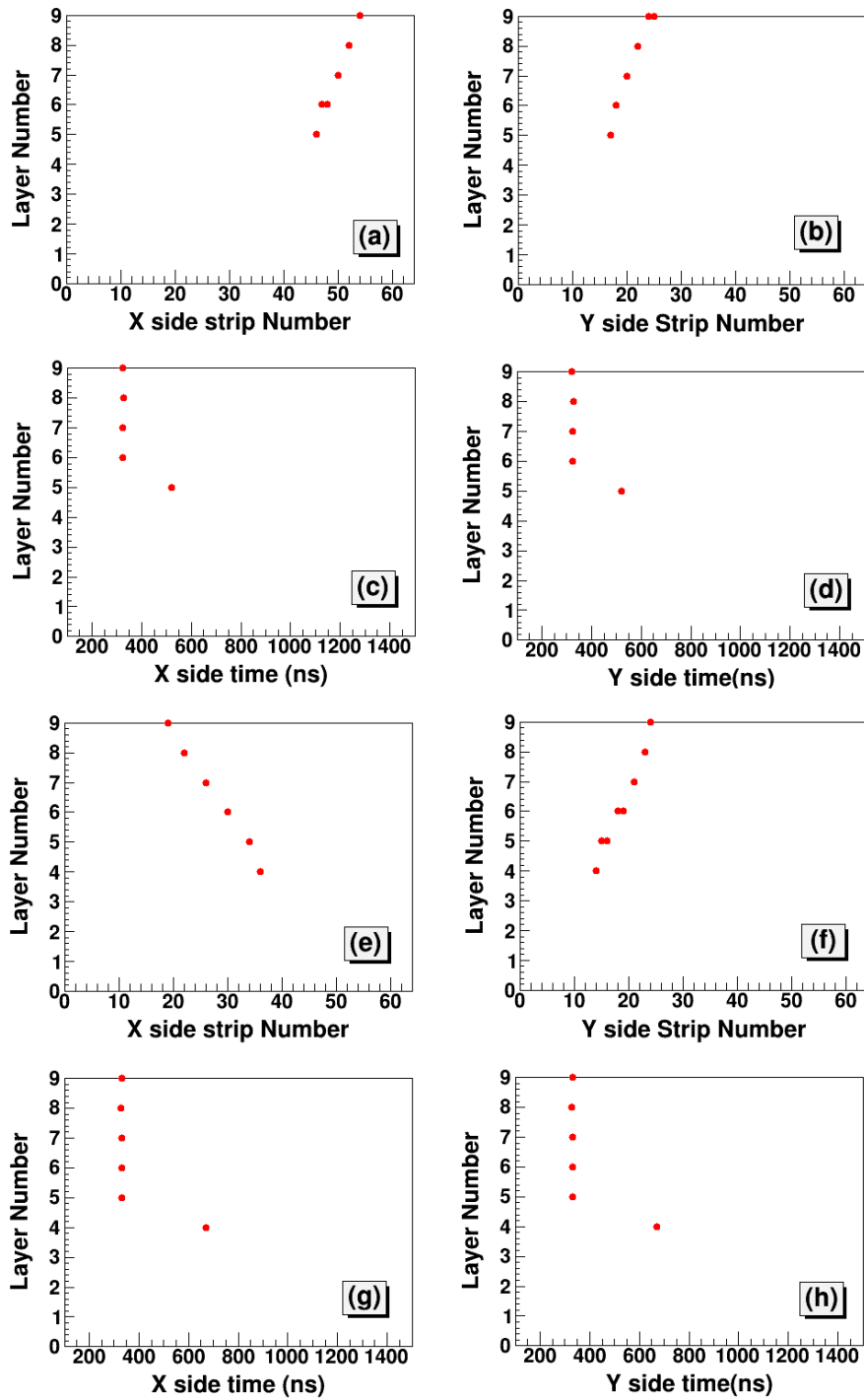


FIGURE 5.15: Candidate muon decay events in layer 5 (a-d) and 4 (e-h).

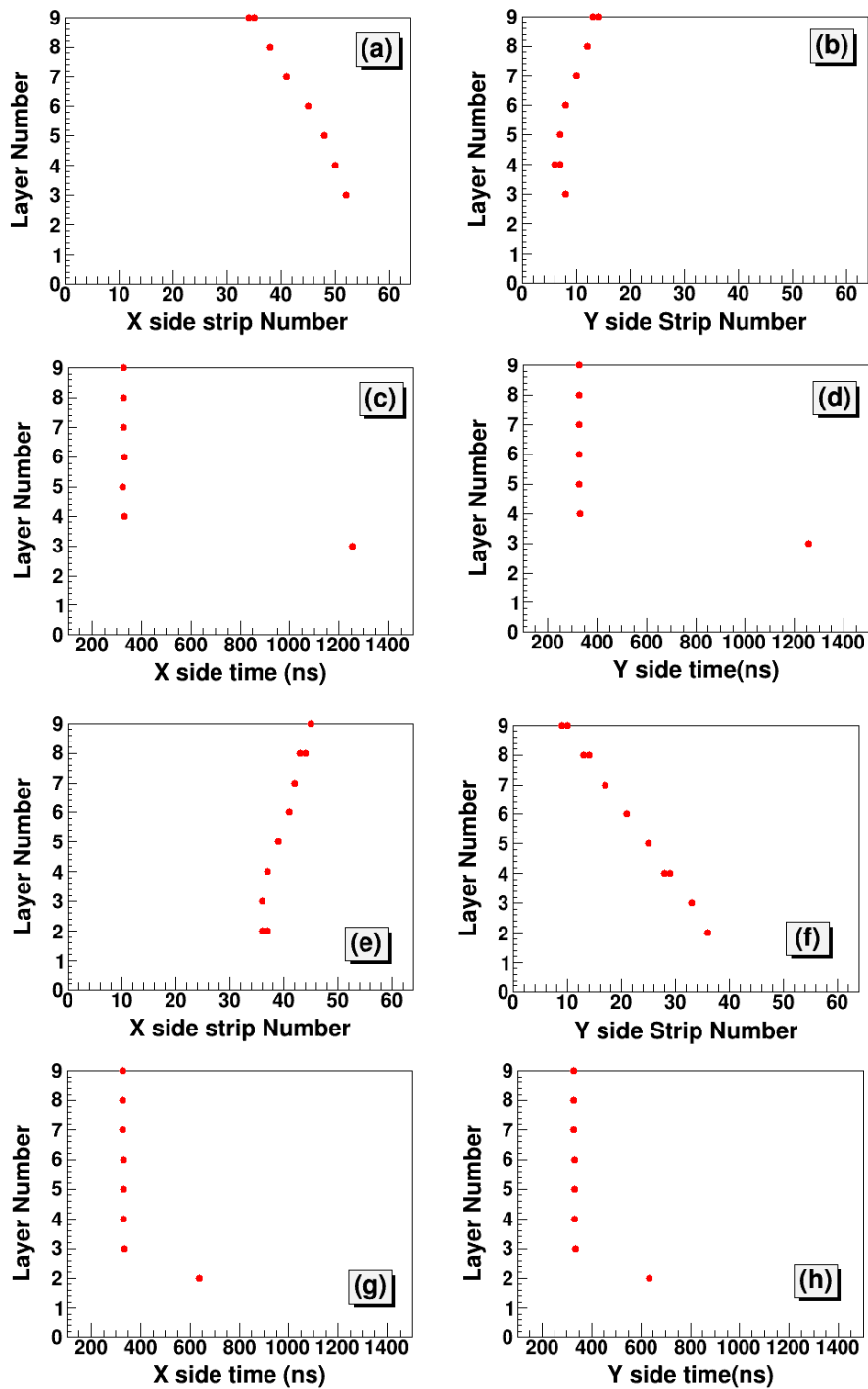


FIGURE 5.16: Candidate muon decay events in layer 3 (a-d) and 2 (e-h).

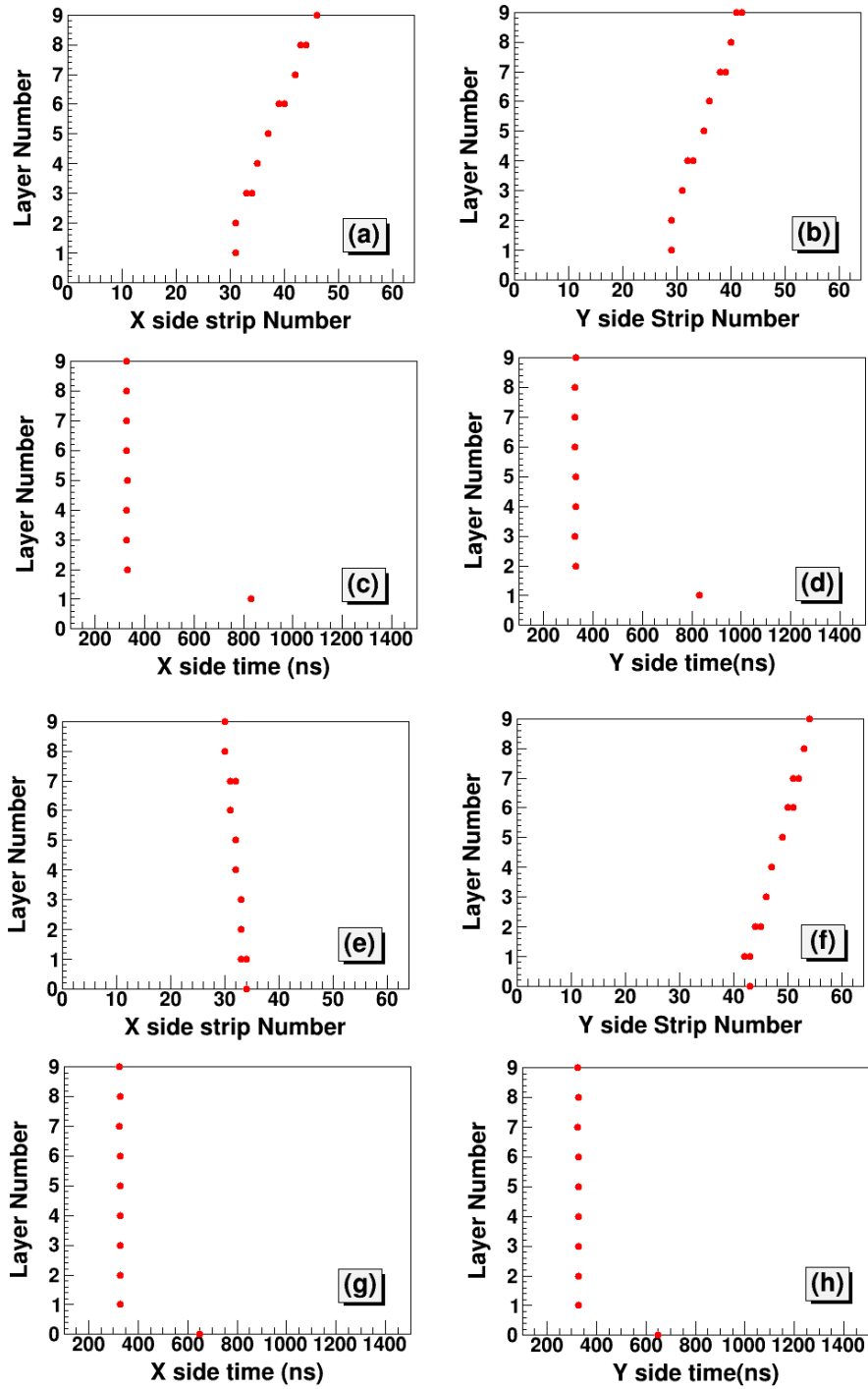


FIGURE 5.17: Candidate muon decay events in layer 1 (a-d) and 0 (e-h).

5.4 Summary

A GEANT4 based simulation, by incorporating full the RPC stack geometry, to decide the thickness of iron plate was performed. The detection efficiency of μ -decay was 31% and 16%, for 2 cm and 4 cm thick iron plates, respectively. An experiment was set up to measure the muon lifetime by putting an iron plate (1 m \times 1 m \times 0.02 m) in between two layers of the 12 layer RPC Stack. Timing data from individual strips of layers above and below the iron plate were acquired by connecting separate multi-hit TDCs. The measured lifetime of muons in the 12 layer RPC stack in the bottom layer was found to be $(2.09 \pm 0.18) \mu\text{s}$. However, the lifetime could not be measured in top layer as the passage of muon RPC makes a local region "dead" for milli sec time. Another small set-up with 5 layers of scintillators (96 cm \times 32 cm \times 1 cm) with iron layer placed in between 3rd and 4th layer from the top was made. The lifetime was measured in the top and bottom PSs to be (1.9 ± 0.2) and $(2.2 \pm 0.2) \mu\text{s}$, respectively. But the asymmetry could not be measured in this set-up due to ion feedback in PMTs due to after-pulsing in the PMTs that were used. An attempt to measure magnetic field inside the magnetic field using μSR was made. The lifetime of muon in iron was measured as $(2.21 \pm 0.01) \mu\text{s}$ and $(0.27 \pm 0.02) \mu\text{s}$ for μ^+ and μ^- , respectively. However, the modulation in the lifetime curve due to μSR signal could not be measured.

Summary

The possibility of carrying out the ICAL experiment at a shallow depth using an active muon veto system instead of a passive shield of rock has been explored. This requires to build an efficient cosmic muon veto detector (CMVD) with a veto efficiency of 99.99% or more. As a modest step towards making a prototype of the CMVD for the main ICAL, the investigation of the challenges involved in achieving such a high veto efficiency in a small size detector had initiated. For this, a CMVD ($1\text{ m} \times 1\text{ m} \times 0.3\text{ m}$) setup was made using plastic scintillators covering all four sides and a ceiling. The scintillation was down-shifted in frequency by Wavelength Shifting Fibers (WLS) which were bunched and measured with Photo Multiplier Tubes (PMT). A trigger setup was made with 4 layers of plastic scintillators, alternated with lead absorber, and kept inside the CMVD. The veto efficiency was obtained as the fraction of events when there is a signal in the CMVD in coincidence with the trigger. The intrinsic efficiency of the individual scintillator is very crucial to achieve the desired veto efficiency. Hence, all the PMTs were characterized first and then the efficiency of individual

scintillators was studied using a 12 layers stack of Resistive Plate Chambers (RPC). In the first attempt, a veto efficiency of $(99.88 \pm 0.007)\%$ was obtained which was improved subsequently in four iterations. Various factors contributing to the veto inefficiency had to be examined and improved upon where possible viz. intrinsic scintillator inefficiency, the number of layers in the veto, proper threshold for the trigger to reduce the compton events, etc. and finally a veto efficiency of $(99.978 \pm 0.002)\%$ was achieved. Motivated by the result of this work a bigger (~ 100 times) CMVD is being made for a small sized magnet prototype of the ICAL detector. Due to the compactness, SiPM based readout is preferred for the bigger CMVD.

The neutrals produced in the muon-nuclear interaction with the rock material could result in a significant background to the neutrino events in a shallow depth ICAL (SICAL) detector. The muon can undergo deep inelastic scattering with the rock material and produce secondary particles. The charged particles can be vetoed in CMVD but the neutrals can simply pass through the CMVD without giving any signal and later on can produce events in the ICAL which can mimic neutrino interactions. A Monte Carlo simulation was needed to estimate such background in the SICAL. As a preliminary step, a GEANT4 based simulation was carried out for estimating the neutral particles produced when only the vertical going muon passes through a block of 103 m of rock. These neutral particles are further propagated in the ICAL simulation code for estimating the neutrino like events produced by such particles. This simulation estimated a background of $\sim 0.1\%$. This underestimates the contribution from the neutrals coming from muons traveling at an angle to the ICAL. Hence, to obtain a more realistic simulation, another GEANT4 based simulation code was

developed, where the ICAL detector is kept inside a cavern surrounded by 3 cm thick scintillator (CMVD) which in turn is kept inside rock material of dimension $2 \text{ km} \times 2 \text{ km} \times 103 \text{ m}$. To take into consideration the complete cosmic muon spectra, the 3D flux (E, θ, ϕ) was generated by CORSIKA which covers 99.9% of the cosmic muon zenith angle spectrum. This simulation resulted in a background of $\sim 0.4\%$ with an upper bound of $\sim 1.2\%$ at 95% C.L. Motivated by this work, the 600 ton engineering prototype of ICAL will be built at a shallow depth of $\sim 30\text{m}$. The data from this detector are expected to validate the simulation results and if so, one can go for shallow depth ICAL experiment.

A small magnet prototype ($4 \text{ m} \times 4 \text{ m} \times 1.2 \text{ m}$) detector (mini-ICAL), comprising of 10 RPCs and 11 iron plates, has been built at IICHEP, Madurai. The advantages of building and operating such a detector are manifold. It allows a comparison of the simulated and measured magnetic fields, the latter using Hall probes and flux loops, monitoring the long term performance of the front end electronics in presence of the fringe magnetic field, the RPC detectors and the closed loop gas system as also the issue of electromagnetic interference (EMI), on the FEE. This experience would be very useful in building the main 51 kTon ICAL detector. The magnetic field in ICAL is of paramount importance for the reconstruction of the momentum of neutrino. The magnetic field in mini-ICAL is currently measured with two different techniques (a) by measuring the induced current in the sense coils around the plates and (b) by Hall probes measurements. However, the technique to measure the magnetic field seen by a passing muon in the iron plate is still an open problem. Muon spin rotation (μSR) is a non-destructive technique which could perhaps be used in ICAL to measure the magnetic field inside the iron plates. For this, a GEANT4 based simulation was

carried out for optimizing thickness of iron plate keeping in mind the small range of electrons in iron and the muon decay event rate in the iron. Though a muon life time of $2.2 \mu\text{s}$ was obtained in the top detector, the lifetime in the bottom detector was $0.148 \mu\text{s}$. Thorough investigation of the source of this discrepancy in the lifetime of muon as observed in top detector was done. It was found that the lifetime could not be measured in the top RPC correctly because the passage of muon from top detector makes RPC dead for a time of \sim tens of ms. After this a set up using a stack of 5 scintillators and one iron plate was made, in order to overcome this limitation. However, ion feedback in PMTs leads to second pulse at around $\sim 400 \text{ ns}$. Due to this second pulse the asymmetry measurements could not be done by this set-up. Lastly, μSR studies were performed on mini-ICAL detector. The lifetime of muon in iron was measured as $2.2 \mu\text{s}$ and $0.2 \mu\text{s}$ for μ^+ and μ^- , respectively with a charge ratio of ~ 1.2 however, did not observe any modulation in lifetime due to spin rotation.

Bibliography

- [1] W. Pauli. “Dear radioactive ladies and gentlemen”. In: *Phys. Today* 31N9 (1978), p. 27.
- [2] R. Wendell et al. “Atmospheric neutrino oscillation analysis with subleading effects in Super-Kamiokande I, II, and III”. In: *Phys. Rev. D* 81 (9 2010), p. 092004. DOI: 10.1103/PhysRevD.81.092004.
- [3] K. Abe et al. “Measurement of neutrino and antineutrino oscillations by the T2K experiment including a new additional sample of ν_e interactions at the far detector”. In: *Phys. Rev. D* 96 (9 2017), p. 092006. DOI: 10.1103/PhysRevD.96.092006.
- [4] M. A. Acero et al. “New constraints on oscillation parameters from ν_e appearance and ν_μ disappearance in the NOvA experiment”. In: *Phys. Rev. D* 98 (3 2018), p. 032012. DOI: 10.1103/PhysRevD.98.032012.
- [5] A. Kumar et al. “Invited review: Physics potential of the ICAL detector at the India-based Neutrino Observatory (INO)”. In: *Pramana* 88.5 (2017), p. 79. ISSN: 0973-7111. DOI: 10.1007/s12043-017-1373-4.

- [6] S. J. Blundell. “Spin-polarized muons in condensed matter physics”. In: *Contemporary Physics* 40.3 (1999), pp. 175–192. DOI: 10.1080/001075199181521. eprint: <https://doi.org/10.1080/001075199181521>.
- [7] S. Agostinelli et al. “Geant4 - a simulation toolkit”. In: *Nuclear Instruments and Methods in Physics Research Section A: Accelerators, Spectrometers, Detectors and Associated Equipment* 506.3 (2003), pp. 250–303. ISSN: 0168-9002. DOI: [https://doi.org/10.1016/S0168-9002\(03\)01368-8](https://doi.org/10.1016/S0168-9002(03)01368-8).
- [8] D. Heck et al. “CORSIKA: A Monte Carlo code to simulate extensive air showers”. In: (1998).
- [9] R. S. Fletcher et al. “sibyll: An event generator for simulation of high energy cosmic ray cascades”. In: *Phys. Rev. D* 50 (9 1994), pp. 5710–5731. DOI: 10.1103/PhysRevD.50.5710.
- [10] E. Fermi. “Versuch einer Theorie der β -Strahlen. I”. In: *Zeitschrift für Physik* 88.3 (1934), pp. 161–177. ISSN: 0044-3328. DOI: 10.1007/BF01351864.
- [11] C. L. Cowan et al. “Detection of the Free Neutrino: a Confirmation”. In: *Science* 124.3212 (1956), pp. 103–104. ISSN: 0036-8075. DOI: 10.1126/science.124.3212.103. eprint: <http://science.sciencemag.org/content/124/3212/103.full.pdf>.
- [12] C. S. Wu et al. “Experimental Test of Parity Conservation in Beta Decay”. In: *Phys. Rev.* 105 (4 1957), pp. 1413–1415. DOI: 10.1103/PhysRev.105.1413.

- [13] G. Danby et al. “Observation of High-Energy Neutrino Reactions and the Existence of Two Kinds of Neutrinos”. In: *Phys. Rev. Lett.* 9 (1 1962), pp. 36–44. DOI: 10.1103/PhysRevLett.9.36.
- [14] M. G. K. Narasimham V. S. Ramana Murthy P. V. Sreekantan B. V. Hino-tani K. Miyake S. Creed D. R. Osborne J. L. Pattison J. B. M. Wolfendale A. W. Achar C. V. Menon. “The K. G. F. Neutrino Experiment”. In: *Quasars and high-energy astronomy* (1965), pp. 311–319.
- [15] F. Reines et al. “Evidence for High-Energy Cosmic-Ray Neutrino Interactions”. In: *Phys. Rev. Lett.* 15 (9 1965), pp. 429–433. DOI: 10.1103/PhysRevLett.15.429.
- [16] R. Davis. “Solar Neutrinos: II. Experimental”. In: *Phys. Rev. Lett.* 12 (1964), pp. 303–305.
- [17] B. Aharmim et al. “Combined analysis of all three phases of solar neutrino data from the Sudbury Neutrino Observatory”. In: *Phys. Rev. C* 88 (2 2013), p. 025501. DOI: 10.1103/PhysRevC.88.025501.
- [18] Ivan Esteban et al. “Global analysis of three-flavour neutrino oscillations: synergies and tensions in the determination of θ_{23} , δ_{CP} , and the mass ordering”. In: *Journal of High Energy Physics* 2019.1 (2019), p. 106. ISSN: 1029-8479. DOI: 10.1007/JHEP01(2019)106.
- [19] Pablo F. de Salas et al. “Neutrino Mass Ordering from Oscillations and Beyond: 2018 Status and Future Prospects”. In: *Frontiers in Astronomy and Space Sciences* 5 (2018), p. 36. ISSN: 2296-987X. DOI: 10.3389/fspas.2018.00036.

- [20] P.F. de Salas et al. “Status of neutrino oscillations 2018: 3 σ hint for normal mass ordering and improved CP sensitivity”. In: *Physics Letters B* 782 (2018), pp. 633–640. ISSN: 0370-2693. DOI: <https://doi.org/10.1016/j.physletb.2018.06.019>.
- [21] V. M. Datar. “Direct Neutrino Mass Measurements”. In: *Proc. Indian Natl. Sci. Acad.* A70.1 (2004), pp. 89–94.
- [22] R. Santonico and R. Cardarelli. “Development of Resistive Plate Counters”. In: *Nucl. Instrum. Meth.* 187 (1981), pp. 377–380. DOI: [10.1016/0029-554X\(81\)90363-3](https://doi.org/10.1016/0029-554X(81)90363-3).
- [23] S. P. Behera et al. “Simulation Studies for Electromagnetic Design of INO ICAL Magnet and Its Response to Muons”. In: *IEEE Transactions on Magnetics* 51.2 (2015), pp. 1–9. ISSN: 0018-9464. DOI: [10.1109/TMAG.2014.2344624](https://doi.org/10.1109/TMAG.2014.2344624).
- [24] A.D. Bhatt et al. “Improvement of time measurement with the INO-ICAL resistive plate chambers”. In: *Journal of Instrumentation* 11.11 (2016), pp. C11001–C11001. DOI: [10.1088/1748-0221/11/11/c11001](https://doi.org/10.1088/1748-0221/11/11/c11001).
- [25] S. Pethuraj et al. “Measurement of cosmic muon angular distribution and vertical integrated flux by 2 m \times 2 m RPC stack at IICHEP-Madurai”. In: *Journal of Cosmology and Astroparticle Physics* 2017.09 (2017), pp. 021–021. DOI: [10.1088/1475-7516/2017/09/021](https://doi.org/10.1088/1475-7516/2017/09/021).
- [26] Karaparambil Rajan Rebin et al. “Study of neutrino oscillation parameters at the INO-ICAL detector using event-by-event reconstruction”. In: *The European Physical Journal C* 79.4 (2019), p. 295. ISSN: 1434-6052. DOI: [10.1140/epjc/s10052-019-6798-0](https://doi.org/10.1140/epjc/s10052-019-6798-0).

- [27] K Nagamine et al. “Cosmic-ray muon spin rotation in Fe and industrial application”. In: *Journal of Physics: Conference Series* 551 (2014), p. 012064. DOI: 10.1088/1742-6596/551/1/012064.
- [28] Deba Prasad Bhattacharyya. “Energy spectra of cosmic pions and nucleons at the top of the atmosphere”. In: *Zeitschrift für Physik* 257.4 (1972), pp. 292–298. ISSN: 0044-3328. DOI: 10.1007/BF01392987.
- [29] Gerald Lynch, J. Orear, and S. Rosendorff. “Measurement of the Asymmetry Parameter in $\mu - e$ Decay”. In: *Phys. Rev. Lett.* 1 (12 1958), pp. 471–472. DOI: 10.1103/PhysRevLett.1.471.
- [30] C. Scott Johnson. “Polarization of Cosmic-Ray Muons at Sea Level”. In: *Phys. Rev.* 122 (6 1961), pp. 1883–1890. DOI: 10.1103/PhysRev.122.1883.
- [31] S N Sen Gupta and M S Sinha. “Decay Asymmetry of Cosmic Ray Muons”. In: *Proceedings of the Physical Society* 79.6 (1962), pp. 1183–1196. DOI: 10.1088/0370-1328/79/6/312.
- [32] Luca Morescalchi. “The Mu2e Experiment at Fermilab”. In: *PoS DIS2016* (2016), p. 259. DOI: 10.22323/1.265.0259. arXiv: 1609.02021 [hep-ex].
- [33] L. Whitehead. “The Daya Bay Muon Veto System”. In: *Nuclear Physics B - Proceedings Supplements* 229-232 (2012). Neutrino 2010, p. 443. ISSN: 0920-5632. DOI: <https://doi.org/10.1016/j.nuclphysbps.2012.09.080>.

- [34] Craig Group and Yuri Oksuzian. “Design considerations for the cosmic-ray-veto system of the Mu2e experiment at Fermilab”. In: *Meeting of the APS Division of Particles and Fields (DPF 2013) Santa Cruz, California, USA, August 13-17, 2013*. 2013. arXiv: 1310.1377 [physics.ins-det].
- [35] Louis Archambault et al. “Plastic scintillation dosimetry: Optimal selection of scintillating fibers and scintillators”. In: *Medical Physics* 32.7Part1 (2005), pp. 2271–2278. DOI: 10.1118/1.1943807.
- [36] N. Panchal et al. “A compact cosmic muon veto detector and possible use with the Iron Calorimeter detector for neutrinos”. In: *Journal of Instrumentation* 12.11 (2017), T11002–T11002. DOI: 10.1088/1748-0221/12/11/t11002.
- [37] M David et al. *Comparative Measurements of WLS Fibers*. Tech. rep. ATL-TILECAL-94-034. ATL-L-PN-34. Geneva: CERN, 1994.
- [38] M. Bhuyan et al. “Cosmic ray test of INO RPC stack”. In: *Nuclear Instruments and Methods in Physics Research Section A: Accelerators, Spectrometers, Detectors and Associated Equipment* 661.Supplement 1 (2012). X. Workshop on Resistive Plate Chambers and Related Detectors (RPC 2010), S68 –S72. ISSN: 0168-9002. DOI: <https://doi.org/10.1016/j.nima.2010.08.034>.
- [39] A. Behere et al. “Electronics and data acquisition system for the ICAL prototype detector of India-based neutrino observatory”. In: *Nuclear Instruments and Methods in Physics Research Section A: Accelerators, Spectrometers, Detectors and Associated Equipment* 701.Supplement C (2013),

- pp. 153–163. ISSN: 0168-9002. DOI: <https://doi.org/10.1016/j.nima.2012.11.007>.
- [40] Mod. V1190A CAEN S.p.A. “TDC technical information manual”. In: 14 (2016).
- [41] Neha et al. “Can Stopped Cosmic Muons Be Used to Estimate the Magnetic Field in the Prototype ICAL Detector?” English. In: *XXII DAE High Energy Physics Symposium-Proceedings*. Vol. 203. Springer Science and Business Media, LLC, Jan. 2018, pp. 93–96. ISBN: 9783319731704. DOI: [10.1007/978-3-319-73171-1_19](https://doi.org/10.1007/978-3-319-73171-1_19).
- [42] N. DASH, V. M. DATAR, and G. MAJUMDER. “Sensitivity for detection of decay of dark matter particle using ICAL at INO”. In: *Pramana* 86.4 (2016), pp. 927–937. ISSN: 0973-7111. DOI: [10.1007/s12043-015-1094-5](https://doi.org/10.1007/s12043-015-1094-5).
- [43] N. Dash, V.M. Datar, and G. Majumder. “Sensitivity of the INO-ICAL detector to magnetic monopoles”. In: *Astroparticle Physics* 70 (2015), pp. 33–38. ISSN: 0927-6505. DOI: <https://doi.org/10.1016/j.astropartphys.2015.03.009>.
- [44] K.A. Olive. “Review of Particle Physics”. In: *Chinese Physics C* 40.10 (2016), p. 100001. DOI: [10.1088/1674-1137/40/10/100001](https://doi.org/10.1088/1674-1137/40/10/100001).
- [45] John Erthal Gaiser. “Charmonium Spectroscopy From Radiative Decays of the J/ψ and ψ' ”. PhD thesis. SLAC, 1982.
- [46] A. G. Bogdanov et al. “Geant4 simulation of production and interaction of muons”. In: *IEEE Transactions on Nuclear Science* 53.2 (2006), pp. 513–519. ISSN: 0018-9499. DOI: [10.1109/TNS.2006.872633](https://doi.org/10.1109/TNS.2006.872633).

- [47] S. Seth et al. “Update of INO-ICAL reconstruction algorithm”. In: *Journal of Instrumentation* 13.09 (2018), P09015–P09015. DOI: 10.1088/1748-0221/13/09/p09015.
- [48] M. Honda et al. “Atmospheric neutrino flux calculation using the NRLMSISE-00 atmospheric model”. In: *Phys. Rev. D* 92 (2 2015), p. 023004. DOI: 10.1103/PhysRevD.92.023004.
- [49] D. Casper. “The nuance neutrino physics simulation, and the future”. In: *Nuclear Physics B - Proceedings Supplements* 112.1 (2002), pp. 161 – 170. ISSN: 0920-5632. DOI: [https://doi.org/10.1016/S0920-5632\(02\)01756-5](https://doi.org/10.1016/S0920-5632(02)01756-5).
- [50] Kolahal Bhattacharya et al. “Error propagation of the track model and track fitting strategy for the Iron CALorimeter detector in India-based neutrino observatory”. In: *Computer Physics Communications* 185.12 (2014), pp. 3259–3268. ISSN: 0010-4655. DOI: <https://doi.org/10.1016/j.cpc.2014.09.003>.
- [51] S. Seth et al. “Update of INO-ICAL reconstruction algorithm”. In: *Journal of Instrumentation* 13.09 (2018), P09015–P09015. DOI: 10.1088/1748-0221/13/09/p09015.
- [52] M. G. Aartsen et al. “Measurement of Atmospheric Neutrino Oscillations at 6–56 GeV with IceCube DeepCore”. In: *Phys. Rev. Lett.* 120 (7 2018), p. 071801. DOI: 10.1103/PhysRevLett.120.071801.
- [53] Essar steel. *Soft Iron Plate*. http://www.essarsteel.com/section_level2.aspx?cont_id=ZACX2FP1m5c=&path=Products_and_processes%3E_Products%3E_Plates.

- [54] J. Weiss et al. “Finite element analysis of magnetic fields with permanent magnet”. In: *IEEE Transactions on Magnetics* 20.5 (1984), pp. 1933–1935. ISSN: 0018-9464. DOI: 10.1109/TMAG.1984.1063462.
- [55] S. Sanfilippo. “Hall probes: physics and application to magnetometry”. In: *Proceedings, 2009 CAS-CERN Accelerator School: Specialised course on Magnets: Bruges, Belgium, June 16 - 25, 2009*. 2011, pp. 423–462. arXiv: 1103.1271 [physics.acc-ph].
- [56] L. J. Laslett. *SOME ASPECTS OF SEARCH COIL DESIGN*. 1989.
- [57] Epoxy Adhesives. *3M Scotch-Weld*. <http://multimedia.3m.com/mws/media/667100/3m-scotch-weld-epoxy-adhesive-dp190-translucent-gray.pdf>.
- [58] S.D. Kalmani et al. “Design validation and performance of closed loop gas recirculation system”. In: *Journal of Instrumentation* 11.11 (2016), pp. C11026–C11026. DOI: 10.1088/1748-0221/11/11/c11026.
- [59] Puneet Kanwar Kaur et al. “Development of Fast, Low Power 8-Channel Amplifier-Discriminator Board for the RPCs”. In: *Springer Proc. Phys.* 203 (2018), pp. 571–574. DOI: 10.1007/978-3-319-73171-1_134.
- [60] V. K. S Kashyap et al. “Performance of ANUSPARSH-III ASIC chipset with 1 m x 2 m glass RPC”. In: *DAE Symp. Nucl. Phys.* 59 (2014), pp. 852–853.
- [61] M. N. Saraf et al. “Soft-Core Processor Based Data Acquisition Module for ICAL RPCs with Network Interface”. In: *XXI DAE-BRNS High Energy Physics Symposium*. Ed. by Bipul Bhuyan. Cham: Springer International Publishing, 2016, pp. 565–570.

- [62] CERN. *HPTDC*. <https://cds.cern.ch/record/1067476/files/cer-002723234.pdf>.
- [63] Sudeshna Dasgupta. “Development and implementation of the trigger system for the INO-ICAL detector”. PhD thesis. Bhabha Atomic Res. Ctr., 2013.
- [64] P. Nagaraj et al. “Ethernet Scheme for Command and Data Acquisition for the INO ICAL Detector”. In: *XXII DAE High Energy Physics Symposium*. Ed. by Md. Naimuddin. Cham: Springer International Publishing, 2018, pp. 863–865.
- [65] P. Kaur et al. “Calibration and Auxiliary Unit for INO’s ICAL Data Acquisition System”. In: *XXII DAE High Energy Physics Symposium*. Ed. by Md. Naimuddin. Cham: Springer International Publishing, 2018, pp. 587–590.
- [66] CAEN. *A3025 power supply board*. <https://www.caen.it/products/a3025/>.
- [67] “Leak rate estimation of a resistive plate chamber gap by monitoring absolute pressure”. In: *JINST* 11.11 (2016), p. C11009.
- [68] Manisha, V. Bhatnagar, and J. S. Shahi. “Study of Glass and Bakelite properties as electrodes in RPCs”. In: *Sci. Technol.* 4 (2016), pp. 21–24. arXiv: 1604.04130 [physics.ins-det].
- [69] J. M. Fowler, H. Primakoff, and R. D. Sard. “The polarization of cosmic ray muons”. In: *Il Nuovo Cimento (1955-1965)* 9.6 (1958), pp. 1027–1045. ISSN: 1827-6121. DOI: 10.1007/BF02777953.

- [70] C. Patrignani et al. “Review of Particle Physics”. In: *Chin. Phys.* C40.10 (2016), p. 100001. DOI: 10.1088/1674-1137/40/10/100001.
- [71] V. B. Brudanin, V. A. Morozov, and N. V. Morozova. “Ion Feedback Afterpulses in $\phi\epsilon\phi$ -130 and XP2020 Photomultipliers”. In: *Instruments and Experimental Techniques* 47.6 (2004), pp. 783–790. ISSN: 1608-3180. DOI: 10.1023/B:INET.0000049701.40676.f9.
- [72] B. K. Lubsandorzhev et al. “Photoelectron backscattering in vacuum phototubes”. In: *Nucl. Instrum. Meth.* A567 (2006), pp. 12–16. DOI: 10.1016/j.nima.2006.05.047. arXiv: physics/0601157 [physics].
- [73] Daniel Ferenc, Dario Hrupec, and Eckart Lorenz. “Solution to the ion feedback problem in hybrid photon detectors and photomultiplier tubes”. In: *Nuclear Instruments and Methods in Physics Research Section A: Accelerators, Spectrometers, Detectors and Associated Equipment* 427.3 (1999), pp. 518–523. ISSN: 0168-9002. DOI: [https://doi.org/10.1016/S0168-9002\(98\)01403-X](https://doi.org/10.1016/S0168-9002(98)01403-X).